

UC San Diego

UC San Diego Electronic Theses and Dissertations

Title

Multicomponent nitrides & carbonitrides: entropy considerations and tunable properties

Permalink

<https://escholarship.org/uc/item/0xs8g1g4>

Author

Dippo, Olivia Faye

Publication Date

2021

Peer reviewed|Thesis/dissertation

UNIVERSITY OF CALIFORNIA SAN DIEGO

Multicomponent nitrides & carbonitrides: entropy considerations and tunable properties

A dissertation submitted in partial satisfaction of the
requirements for the degree Doctor of Philosophy

in

Materials Science and Engineering

by

Olivia Faye Hrycyk Dippo

Committee in charge:

Professor Kenneth Vecchio, Chair
Professor Vlado Lubarda
Professor Jian Luo
Professor Chia-Ming Uang
Professor Kesong Yang

2022

Copyright

Olivia Faye Hrycyk Dippo, 2022

All rights reserved.

The dissertation of Olivia Faye Hrycyk Diplo is approved, and it is acceptable in quality and form for publication on microfilm and electronically.

University of California San Diego

2022

iii

DEDICATION

Dedicated to my sisters, especially Grace, Eve, and Sienna.

EPIGRAPH

Splendor awaits in minute proportions.

E.O. Wilson

TABLE OF CONTENTS

Dissertation Approval Page	iii
Dedication	iv
Epigraph	v
Table of Contents	vi
List of Figures	viii
List of Tables	x
Acknowledgements	xi
Vita	xiii
Abstract of the Dissertation	xv
Introduction	1
Thermodynamic background	1
High-entropy materials	2
Nitride & carbonitride ceramics	3
References	5
Chapter 1: A universal configurational entropy metric for high-entropy materials	8
Abstract	8
1.1 Main Text	8
Acknowledgements:	18
References:	18
Chapter 2: Bulk high-entropy nitrides and carbonitrides	21
Abstract	21
2.1 Introduction	22
2.2 Materials & Methods	24
2.2.1 Synthesis	24
2.2.2 Characterization	26
2.2.3 Mechanical testing	26
2.3 Results	27
2.3.1 Single-phase Formation: Crystal Structure	27
2.3.2 Single-phase Formation: Random Distribution of Elements	29
2.3.4 Equiatomic phase formation	32
2.3.5 Mechanical Properties	33
2.3.6 Valence Electron Concentration and Hardness	36
2.3.7 Randomness, Configurational Entropy, and Hardening	36
2.3.8 Entropic strengthening versus solid solution strengthening	39
2.3.9 Stoichiometry	40
2.4 Discussion	41

Acknowledgements.....	43
Supplementary Information	44
References.....	53
Chapter 3: Color and pseudogap tunability in multicomponent carbonitrides	59
Abstract.....	59
3.1 Introduction.....	60
3.2 Methods	62
3.2.1 Synthesis.....	62
3.2.2 UV-Vis-Near IR Spectroscopy.....	64
3.2.3 CIEL *a*b*/CIEL *C*h* Color Measurement.....	64
3.2.4 Tauc Plots	65
3.2.5 Rule of Mixtures Color Calculations.....	66
3.2.6 Density of States Calculations.....	67
3.3 Results and Discussion	68
3.3.1 Color.....	68
3.3.2 Optical Pseudogap Analysis.....	70
3.3.3 Hue and Chroma Trends in Carbonitrides.....	71
3.4 Conclusions.....	77
Acknowledgements.....	78
Supplementary Information	80
References.....	90
Conclusions & Future Directions.....	94
Conclusions.....	94
Future Directions	96
References.....	98

LIST OF FIGURES

<i>Figure 1.1:</i> (left) 5-metal carbide with a 1:1 metal to anion ratio, (right) 5-metal carbide with a 23:6 metal to anion ratio, with the structure of $M_{23}C_6$	11
<i>Figure 2.1:</i> Example progression of HECN #2 (CrNbTaTiV)(CN) through the processing steps: hand-mixed (bottom), high-energy ball-milled (middle), and then sintered (top). A residual graphite peak is marked with a black diamond.....	28
<i>Figure 2.2:</i> XRD of all 6 carbonitride (left) and 5 nitride (right) compositions. HEN and HECN #1-5 are FCC-rocksalt structures, with some residual native oxides present. HECN #6 shows multiple phases. Intensities are normalized by the highest intensity present in each spectrum. ..	29
<i>Figure 2.3:</i> Secondary electron images and corresponding elemental EDS maps of selected compositions. HEN #2, HECN #2, and HEN #3 have elements homogenously distributed throughout the matrix, and thus are considered single-phase high-entropy ceramics.	30
<i>Figure 2.4:</i> (a) Nanoindentation hardness as a function of valence electron concentration (VEC). Error bars are 1 standard deviation from the mean value. (b) Increase in hardness as a function of ideal configurational entropy, where R is the gas constant. Pearson correlation coefficients are equal to -0.90 and 0.75 for (a) and (b) respectively.....	37
<i>Supplementary Figure 2.1:</i> Microstructure and EDS composition maps for HEN and HECN #1,4,5, which are not included in the main text of the paper. Note the different scale in HEN and HECN #1.....	46
<i>Supplementary Figure 2.2:</i> Nanoindentation hardness as a function of force for composition HECN #2: (CrNbTaTiV)(CN). The minimum force threshold (dotted line) for testing was designated as 100nN. The solid blue line represents an average hardness value of 30.0 GPa from 100 tests at 300 nN.....	47
<i>Supplementary Figure 2.3:</i> Nanoindentation hardness (a) and modulus (b) as a function of the expected rule-of-mixtures (ROM) properties of the binary components. $Y=x$ is displayed as a dashed line. All measured nanoindentation hardness and modulus values are higher than the expected ROM values, though no trend is identified.....	48
<i>Supplementary Figure 2.4:</i> Nanoindentation hardness (a) and modulus (b) as a function of anion stoichiometry (carbon+nitrogen). No trend is identified between anion stoichiometry of the high-entropy compositions and mechanical properties. Error bars are 1 standard deviation from the mean value.	49
<i>Supplementary Figure 2.5:</i> The ideal configurational entropy of single anion (i.e. nitride) and two anion (i.e. carbonitride) systems. 10-metal nitrides have equal ideal configurational entropy (S/R) to 5-metal carbonitrides. X corresponds to the site fraction of the metals present in the material, where the maximum entropy corresponds to an equiatomic site fraction.	51
<i>Supplementary Figure 2.6:</i> RMS geometric intrinsic residual strain vs configurational entropy. Dashed line is a linear fit with pearson correlation coefficient = 0.95.	52
<i>Figure 3.1:</i> (a) Examples of colors of 10 multicomponent carbonitride materials synthesized in this work, displaying the range of colors achievable. (b) Reflectance plots for three carbonitride	

samples: $Zr(C_{0.1}N_{0.9})$, a high-saturation gold hue (top), and $Ti(C_{0.2}N_{0.8})$, displaying a lower-saturation pink color (middle), and $(Ti_{0.1}Zr_{0.9})(C_{0.6}N_{0.4})$ displaying a gray-purple color. 69

Figure 3.2: (a) Example Tauc plot, illustrating the extrapolation method for the determination of optical pseudogap energy. (b) Pseudogap energy based on a rule of mixtures (ROM) average of the precursor mononitrides and monocarbides vs the measured pseudogap energy extrapolated from Tauc plots. Linear fit line constitutes the prediction method for pseudogap energies..... 70

Figure 3.3: Hue and chroma trends with pseudogap energy. (a) Hue vs pseudogap energy, with fit line included for carbonitrides, which can access a larger range of hues than monocarbides and mononitrides. (b) Chroma value vs pseudogap energy. The high-entropy nitrides (HENs) and high-entropy carbonitrides (HECNs) shown were synthesized in Ref. [20]. 72

Figure 3.4: (a) Example total density of states (in arbitrary units) calculated via DFT for B1-structured TiN, TiC, ZrN, and ZrC at 0 kelvin. Dashed lines mark the anion-p/metal-d valence band peak energies. Energy = 0 is defined as the Fermi level. (b) The chroma of carbonitrides can be predicted from the density of states..... 74

Figure 3.5: The predicted hues and chromas of all possible combinations of carbonitrides with up to 5 metals (Ti, Zr, Hf, V, Nb, Ta), having $C_{adj}^* > 5$ and $L_{ROM}^* > 70$. Hue (h_{adj}^* , theta axis) represents the angle around the color wheel and chroma (C_{adj}^* , r-axis) represents the saturation of the color. 76

Supplementary Figure 3.1: Density of states for B1-structured TiN..... 82

Supplementary Figure 3.2: Density of states for B1-structured TiC..... 82

Supplementary Figure 3.3: Density of states for B1-structured ZrN..... 83

Supplementary Figure 3.4: Density of states for B1-structured ZrC..... 83

Supplementary Figure 3.5: Electronic density of states for B1-structured HfN..... 84

Supplementary Figure 3.6: Electronic density of states for B1-structured HfC..... 84

Supplementary Figure 3.7: Electronic density of states for B1-structured VN..... 85

Supplementary Figure 3.8: Electronic density of states for B1-structured VC..... 85

Supplementary Figure 3.9: Electronic density of states for B1-structured NbN..... 86

Supplementary Figure 3.10: Electronic density of states for B1-structured NbC..... 86

Supplementary Figure 3.11: Electronic density of states for B1-structured TaN..... 87

Supplementary Figure 3.12: Electronic density of states for B1-structured TaC..... 87

Supplementary Figure 3.13: Electronic density of states for B1-structured CrN..... 88

Supplementary Figure 3.14: Electronic density of states for B1-structured CrC..... 88

Supplementary Figure 3.15: Experimental chroma vs ROM Chroma with DOS adjustment (Eq. 3.18 in main text). The fitting data was used to fit the chroma model. In the test case, two materials with approximately the same hue but different chroma values according to the DOS adjustment were successfully predicted and synthesized. 89

LIST OF TABLES

<i>Table 1.1:</i> Quantification of entropy and new entropy metric. In the structure type examples, (5M), (5N), and similar notation denotes there are 5 species on that particular lattice site.	15
<i>Table 2.1:</i> Composition of experimental samples in atomic percent, calculated from EDS analysis of metal content and CHNS chemical analysis of carbon and nitrogen content. Metals are expected to be in equal atomic proportion.	32
<i>Table 2.2:</i> Nanoindentation elastic modulus, hardness, and Poisson’s ratios for every monocarbide and mononitride used as a precursor for the HENs and HECNs. Modulus and hardness are measured from samples synthesized via SPS. Poisson’s ratios are gathered from the literature, and mechanical properties for carbides (except CrC) are from Ref. [9].	34
<i>Table 2.3:</i> Composition, stoichiometry, density, hardness values, and modulus values for each composition. Theoretical density was calculated using lattice parameters from XRD and atomic ratios from EDS and CHNS chemical analysis, except for HECN#6 which was calculated using the weighted average density of the monocarbide/nitride precursors.	35
<i>Supplementary Table 2.1:</i> Phases present in precursor powders used in the synthesis of high-entropy nitrides and carbonitrides, from XRD.	44
<i>Supplementary Table 2.2:</i> Phases present in sintered bulk samples, from XRD (see Figure 2.2 in main text) and EDS (see Figure 2.3 in main text and Supplementary Figure 2.1).	45
<i>Supplementary Table 2.3:</i> A comparison of different ways of calculating ideal configurational entropy values for different high-entropy materials. Rows 1 and 2 represent high-entropy alloys with 5 metals (5M) and 10 metals (10M). Rows 3 and 4 represent 5-metal carbonitrides with different stoichiometries.	50
<i>Supplementary Table 2.4:</i> Pearson correlation coefficients for mechanical properties from nanoindentation vs different metrics used to analyze trends. Entropy is calculated using the sublattice model.	52
<i>Table 3.1:</i> Listing of the nitrides and carbonitrides in the present study.	63
<i>Supplementary Table 3.1:</i> Precursor monocarbide and mononitride samples, with their measured CIELCh color values from wavelength-dependent reflection, pseudogap energies (E_{pg}) from Tauc plot analysis, and the energy of the total valence band peak in the calculated electronic density of states ($E_{valence, totDOS}$).	80
<i>Supplementary Table 3.2:</i> Carbonitride samples analyzed in this work, with their measured CIELCh color values from wavelength-dependent reflection and pseudogap energies (E_{pg}) from Tauc plot analysis.	81

ACKNOWLEDGEMENTS

I would like to acknowledge Dr. Kenneth Vecchio, Dr. Rusty Gray, Veronica Livescu, and Dr. Anthony Rollett, without whose mentorship I would not be the scientist I am today. An additional thank you to Dr. Janette Williams for guiding me toward my leadership potential.

I would like to acknowledge the NanoEngineering Materials Research Center staff Wayne Neilson, Sabine Faulhauber, and Dr. Stephen Horvath for their invaluable experimental assistance and advice.

I would like to acknowledge members of the Vecchio lab past and present: Kevin Kaufmann, Thomas Liu, Haoren Wang, Tyler Harrington, Chaoyi Zhu, Mojtaba Saimee, Joshua Gild, William Mellor, Eduardo Marin, Neda Mesgarzadeh, Grant Schrader, Cameron McElfresh, Wenyou Jiang, Mahika Luncker, Samuel Figueroa, and Emma Wenger.

Thank you to my parents and my sisters, Eve and Grace, for your unwavering support. I'd also like to acknowledge my friends, including Taylor Reck, Andy Zhao, Anthony Thomas, Nancy Donald, Matt Powell-Palm, Mele Johnson, Ben Sarno, Gabe Renna, and so many more, for listening, supporting, and laughing with me. Sam Solomon, thank you for keeping me honest and on track. Lastly, an enormous thank you to Will McCarthy for your boundless compassion, silliness, and support.

Chapter 1, in full, is a reprint of the material “A universal configurational entropy metric for high-entropy materials” as it appears in *Scripta Materialia* 2021. Dippo, Olivia F.; Vecchio, Kenneth S. The dissertation author was the primary investigator and author of this material.

Chapter 2, in full, is a reprint of the material “Bulk high-entropy nitrides and carbonitrides” as it appears in *Scientific Reports* 2020. Dippo, Olivia F.; Mesgarzadeh, Neda;

Harrington, Tyler J.; Schrader, Grant D.; Vecchio, Kenneth S. The dissertation author was the primary investigator and author of this material.

Chapter 3, in full, has been submitted for publication of the material “Color and pseudogap tunability in multicomponent carbonitrides” as it may appear in *Materials & Design* 2022. Dippo, Olivia F.; Sangiovanni, Davide G.; Wenger, Emma H.; Vecchio, Kenneth S. The dissertation author was the primary investigator and author of this material.

VITA

- 2015 Bachelor of Science, Carnegie Mellon University
- 2015-2016 Post-Baccalaureate, Los Alamos National Laboratory
- 2017 Master of Science, University of California San Diego
- 2022 Doctor of Philosophy, University of California San Diego

PUBLICATIONS

Dippo, O.F., Sangiovanni, D.G., Wenger, E.H., Vecchio, K.S. Color and pseudogap tunability in multicomponent carbonitrides. *Submitted*. (2021)

Vecchio, K.S. **Dippo, O.F.**, Kaufmann, K.R., Liu, Xiao. High-Throughput Rapid Experimental Alloy Development (HT-READ). *Acta Materialia*. 221 (2021) 117352.
doi:10.1016/j.actamat.2021.117352

Mellor, W M., Kaufmann, K.R., **Dippo, O.F.**, Figueroa, S. D., Schrader, G. D., Vecchio, K.S. Development of ultrahigh-entropy ceramics with tailored oxidation behavior. *Journal of the European Ceramic Society*. 41 (2021) 12, 5791-5800. *doi: 10.1016/j.jeurceramsoc.2021.05.010*

Dippo, O.F., Vecchio, K.S. A universal configurational entropy metric for high-entropy materials. *Scripta Materialia*. 201 (2021) 113974. *doi:10.1016/j.scriptamat.2021.113974*

Dippo, O.F., Mesgarzadeh, N., Harrington, T.J, Schrader, G.D., Vecchio, K.S. Bulk high-entropy nitrides and carbonitrides. *Scientific Reports*. 10 (2020) 21288. doi:10.1038/s41598-020-78175-8

Livescu, V., Beyerlein, I.J., Bronkhorst, C., **Dippo, O.F.**, Ndefru, B.G., Capolungo, L., Mourad, H.M., Microstructure insensitive twinning: A statistical analysis of incipient twins in high-purity titanium. *Acta Materialia*. 6 (2019) 100303. doi: 10.1016/j.mta.2019.100303

Harrington, T.J., Gild, J., Sarker, P., Toher, C., Rost, C.M., **Dippo, O.F.**, McElfresh, C., Kaufmann, K., Marin, E., Borowski, L., Hopkins, P.E., Luo, J., Curtarolo, S., Brenner, D.W., Vecchio, K.S. Phase stability and mechanical properties of novel high entropy transition metal carbides. *Acta Materialia*. 166 (2019) 271-280. doi: 10.1016/j.actamat.2018.12.054.

Zhu, C.Y., Livescu, V., Harrington, T., **Dippo, O.**, Gray, G.T., III, Vecchio, K.S. Investigation of the shear response and geometrically necessary dislocation densities in shear localization in high-purity titanium. *International Journal of Plasticity*. 92 (2017) 148-163. doi:10.1016/j.ijplas.2017.03.009.

Jones, D.R., Fensin, S.J., **Dippo, O.**, Beal, R.A., Livescu, V., Martinez, D.T., Trujillo, C.P., Florando, J.N., Kumar, M., Gray, G.T., III. Spall fracture in additive manufactured Ti-6Al-4V. *Journal of Applied Physics*. 120 (2016) 13. doi:10.1016/j.ijplas.2017.03.009.

ABSTRACT OF THE DISSERTATION

Multicomponent nitrides & carbonitrides: entropy considerations and tunable properties

by

Olivia Faye Hrycyk Dippo

Doctor of Philosophy in Materials Science and Engineering

University of California San Diego, 2022

Professor Kenneth Vecchio, Chair

Transition metal nitrides and carbonitrides are used in applications ranging from extreme high-temperature environments, for their high thermal stability, to decorative coatings, for their bright golden color. Multicomponent mixtures of nitrides and carbides facilitate advantageous tunability of material properties, in some cases connected to an increase in configurational entropy. Entropic considerations for high-entropy versions of nitrides and carbonitrides are

discussed, including consistent methods for calculating configurational entropy in materials with complex crystal structures and entropy thresholding for high and low-entropy materials. A new entropy metric for consistent entropy thresholding across all crystal structures is established, marking the first universal configurational entropy metric, with potential to unify the field of high-entropy materials. Eleven novel bulk high-entropy nitrides and carbonitrides are synthesized. Their composition and single-phase character are characterized using X-ray diffraction, energy dispersive x-ray spectroscopy, and combustion analysis. Their mechanical properties are analyzed using nanoindentation hardness, and a significant increase in hardness and elastic modulus above rule-of-mixtures averages is found. High-entropy carbonitrides exhibit greater hardness and modulus enhancements than the high-entropy nitrides, linked to higher configurational entropy levels and decreased valence electron concentrations, two important parameters for the tunability of mechanical properties in high-entropy ceramics. Multicomponent carbonitrides are also optimized for their optical properties. Reflectance spectra were acquired using ultraviolet-visible-near infrared spectroscopy, color quantification was obtained using CIE L*a*b* color standards, and pseudogap energies were extrapolated using Tauc analysis. Parameters for prediction and tunability of pseudogap energy and color appearance are established for multicomponent transition metal carbonitrides, ushering in a new generation of materials with advantageous optical and decorative properties as well as high, tunable hardness.

Introduction

Thermodynamic background

Entropy, a measure of disorder in a system, has become a prominent factor in material design in recent years. It contributes to important thermodynamic properties of materials, including phase transitions such as melting, freezing, and evaporation. There are several different types of entropy including configurational, vibrational, magnetic, and electronic. However, as configurational entropy predominates in most solid-state ceramics and alloys, configurational entropy will be the focus in this work. Configurational entropy quantifies the number of energetically distinct atomic configurations that can exist in a system, in other words, how mixed-up atoms or particles are. Higher atomic mixing corresponds to higher configurational entropy [1].

For systems at thermodynamic equilibrium, the Gibbs Free Energy is minimized. This parameter is an important tool for understanding probable phase formation, according to $G = H - TS$, where G is the Gibbs Free Energy, H is enthalpy, T is temperature, and S is entropy [1]. In traditional alloy design strategies, the understanding and engineering of phase stability focused on enthalpy. Enthalpy describes the heat content of a system and can be intuited as the bond strength between atoms. However, at high temperatures, entropy (S) becomes proportionally more important. If entropy is engineered to have a high baseline within a material, it will have a stabilizing effect, especially at high temperatures. Entropy maximization may facilitate material design for the most extreme environments, where high strength and hardness are required in addition to high-temperature stability.

High-entropy materials

High-entropy materials originated in metallic alloys. One of the first was the Cantor alloy, an equiatomic multicomponent five-element alloy FeCrMnCoNi, plus some six-element variations, published in 2004 [2]. In the same year, Yeh *et al.* published a study of equiatomic alloys with 5-8 elements and coined the term ‘high-entropy alloys’ as part of a new alloy design technique [3]. High-entropy alloys, designed to take advantage of property changes that arise with high levels of configurational entropy, are designated according to their entropy level. An alloy having configurational entropy greater than $1.5R$, where R is the gas constant, is considered ‘high’ entropy; this threshold corresponds to an equiatomic metallic alloy with 5 elements randomly mixed in solid solution [4]. Such entropic thresholding places several constraints on the material, because in order for entropy to be maximized, a material must be equiatomic, in other words having all elements in equal atomic proportions, and it must be a completely random solid solution, i.e. no elemental ordering or phase separation. To avoid those constraints, there are also compositional definitions of materials, including multi-principal element alloys, complex concentrated alloys, and multicomponent alloys which describe a broader range of materials than high-entropy alloys [2,5].

In the original high-entropy alloys, comprising equiatomic solid-solution metallic materials with all atomic positions being equal, quantifying the entropy increase with atomic mixing is straightforward: it depends on the number of elements present. However, in even the simplest ceramics, such as a nitride, carbide, or oxide, there are at least two inequivalent atomic positions in the crystal structure: one for the anion (C,N,O, etc.) and one for the cation (such as transition metals). When crystal structures increase in complexity, in this case by having multiple inequivalent atomic positions, the quantification of entropy also increases in complexity. This

has sowed confusion and discord in the field of high-entropy materials, regarding methods for quantifying entropy and thresholding for high-, medium-, and low-entropy determinations.

In Chapter 1, methods of entropy determination will be discussed with a critical eye toward mathematical and thermodynamic consistency. A novel entropy metric, for accurate and consistent determinations of entropy levels in materials, no matter how complex their crystal lattice, is proposed. This entropy metric has the potential to unite the field of high-entropy materials, making consistent entropic determinations across all types of materials and crystal systems. Throughout this dissertation, materials having a sufficiently high entropy metric will be referred to as high-entropy. Those materials not designed to have high configurational entropy or maximize entropy-related properties will be referred to as multicomponent, corresponding to the presence of multiple elements.

Inspired by research in high-entropy metallic alloys, the first high-entropy ceramic, (MgNiCoCuZn)O, was synthesized by Rost *et al.* in 2015 [6]. The five-metal oxide was found to have increased phase stability over its components, and this pioneering report inspired a rapid increase in high-entropy ceramics research [7]. In this dissertation, high-entropy nitrides and carbonitrides will be discussed, and in parallel with this research, there have also been significant advances in comparable high-entropy ceramics such as carbides [8–10], borides [11], oxides [12–18], and more within the last five years.

Nitride & carbonitride ceramics

Transition metal nitrides, carbides, and solid solution mixtures of nitrides and carbides (carbonitrides) have a unique mixed bond type, which leads to a favorable mixture of properties. Their bonds are partially covalent, granting high hardness and high thermal stability, and

partially metallic, granting them high conductivity and the prospect of engineered ductility [10,19]. Most group 4 and 5, and some group 6 transition metals (M) form a 1:1 compound with anions (A) carbon and nitrogen, M_1A_1 , with a face-centered cubic (FCC) crystal structure. Those FCC crystal structures are also stable at a wide range of anion stoichiometries, M_1A_x , where x ranges from approximately 0.5 to 1, though certain nitrides can have $x > 1$ [20]. This range of stoichiometries is enabled by the mixed bond character and, as such, allows the bond character to shift with stoichiometry. As anion stoichiometry (x) decreases, metallic bond character increases due to increased metal-metal interactions across the anion vacancies [21,22]. This anion stoichiometry is tailorable with certain synthesis procedures. Metallic bond character can also be influenced by the valence electron concentration of the nitride/carbide/carbonitride, which is influenced both by anion stoichiometries, anion ratios (i.e. C/N ratio), and the transition metal elements present [19].

These favorable combinations of properties make nitrides and carbonitrides ideal candidates for materials which function in both everyday environments, including hard-facing wear resistant and/or decorative coatings [23,24], and extreme environments such as high-temperature thermoreflectance measurements [25], fuels for nuclear reactors [26], and leading edges for hypersonic missiles [27]. In the synthesis of high-entropy versions of nitrides and carbonitrides in this work, the aim is: (i) to understand which properties are tunable across the wide range of compositional variation possible and (ii) to identify properties which can be enhanced due to the increase of configurational entropy in in single-anion systems (nitrides) and multi-anion systems (carbonitrides) having one or multiple cations. In Chapter 2, the first synthesis of bulk high-entropy nitrides and carbonitrides is reported, and the parameters which are critical to tuning and enhancing their mechanical properties are detailed.

In Chapter 3, the tunability of optical and electronic properties of multicomponent carbonitrides is explored, with less emphasis on maximizing configurational entropy. The materials synthesized and predicted in Chapter 3 are carbonitride solid solutions having more than one element type on at least one of the two atomic sites (metal or anion). The mechanisms of color production in multicomponent carbonitrides are analyzed based on electron transition energies from the valence band to the conduction band and the connection to absorption properties in the visible range. By mixing carbides and nitrides, the transition energies and their selectivity are controllable, and prediction methods are established for the colored appearance of multicomponent carbonitrides. Throughout the course of this dissertation, we will discuss entropy parameters, high-entropy synthesis, tunability of mechanical properties, and tunability of optical properties in multicomponent transition metal nitrides and carbonitrides. Novel mechanical and optical properties are discovered, and the potential for complete tunability in nitrides and carbonitrides is explored.

References

- [1] D.R. Gaskell, *Introduction to the Thermodynamics of Materials*, 5th ed., Taylor & Francis, New York, NY, 2008.
- [2] B. Cantor, I.T.H. Chang, P. Knight, A.J.B. Vincent, Microstructural development in equiatomic multicomponent alloys, *Materials Science and Engineering A*. 375–377 (2004) 213–218. <https://doi.org/10.1016/j.msea.2003.10.257>.
- [3] J.-W. Yeh, S.-K. Chen, S.-J. Lin, J.-Y. Gan, T.-S. Chin, T.-T. Shun, C.-H. Tsau, S.-Y. Chang, Nanostructured High-Entropy Alloys with Multiple Principal Elements: Novel Alloy Design Concepts and Outcomes, *Advanced Engineering Materials*. 6 (2004) 299–303. <https://doi.org/10.1002/adem.200300567>.
- [4] B.S. Murty, J.W. Yeh, S. Ranganathan, P.P. Bhattacharjee, High-entropy ceramics, in: *High-Entropy Alloys*, 2nd ed., Elsevier, 2019: pp. 165–176. <https://doi.org/10.1016/b978-0-12-816067-1.00009-6>.

- [5] D.B. Miracle, O.N. Senkov, A critical review of high entropy alloys and related concepts, *Acta Materialia*. 122 (2017) 448–511. <https://doi.org/10.1016/j.actamat.2016.08.081>.
- [6] C.M. Rost, E. Sacht, T. Borman, A. Moballegh, E.C. Dickey, D. Hou, J.L. Jones, S. Curtarolo, J.P. Maria, Entropy-stabilized oxides, *Nature Communications*. 6 (2015) 1–8. <https://doi.org/10.1038/ncomms9485>.
- [7] C. Oses, C. Toher, S. Curtarolo, High-entropy ceramics, *Nature Reviews Materials*. 5 (2020) 295–309. <https://doi.org/10.1038/s41578-019-0170-8>.
- [8] P. Sarker, T. Harrington, C. Toher, C. Oses, M. Samiee, J.-P. Maria, D.W. Brenner, K.S. Vecchio, S. Curtarolo, High-entropy high-hardness metal carbides discovered by entropy descriptors, *Nature Communications*. 9 (2018) 4980. <https://doi.org/10.1038/s41467-018-07160-7>.
- [9] E. Castle, T. Csanádi, S. Grasso, J. Dusza, M. Reece, Processing and Properties of High-Entropy Ultra-High Temperature Carbides, *Scientific Reports*. 8 (2018). <https://doi.org/10.1038/s41598-018-26827-1>.
- [10] T.J. Harrington, J. Gild, P. Sarker, C. Toher, C.M. Rost, O.F. Dippo, C. McElfresh, K. Kaufmann, E. Marin, L. Borowski, P.E. Hopkins, J. Luo, S. Curtarolo, D.W. Brenner, K.S. Vecchio, Phase stability and mechanical properties of novel high entropy transition metal carbides, *Acta Materialia*. 166 (2019) 271–280. <https://doi.org/10.1016/j.actamat.2018.12.054>.
- [11] J. Gild, Y. Zhang, T. Harrington, S. Jiang, T. Hu, M.C. Quinn, W.M. Mellor, N. Zhou, K. Vecchio, J. Luo, High-Entropy Metal Diborides: A New Class of High-Entropy Materials and a New Type of Ultrahigh Temperature Ceramics, *Scientific Reports*. 6 (2016). <https://doi.org/10.1038/srep37946>.
- [12] S. Jiang, T. Hu, J. Gild, N. Zhou, J. Nie, M. Qin, T. Harrington, K. Vecchio, J. Luo, A new class of high-entropy perovskite oxides, *Scripta Materialia*. 142 (2018) 116–120. <https://doi.org/10.1016/j.scriptamat.2017.08.040>.
- [13] A. Sarkar, B. Breitung, H. Hahn, High entropy oxides: The role of entropy, enthalpy and synergy, *Scripta Materialia*. 187 (2020) 43–48. <https://doi.org/10.1016/j.scriptamat.2020.05.019>.
- [14] S.J. McCormack, A. Navrotsky, Thermodynamics of high entropy oxides, *Acta Materialia*. 202 (2021) 1–21. <https://doi.org/10.1016/j.actamat.2020.10.043>.
- [15] K. Chen, X. Pei, L. Tang, H. Cheng, Z. Li, C. Li, X. Zhang, L. An, A five-component entropy-stabilized fluorite oxide, *Journal of the European Ceramic Society*. 38 (2018) 4161–4164. <https://doi.org/10.1016/j.jeurceramsoc.2018.04.063>.
- [16] A. Sarkar, R. Djenadic, D. Wang, C. Hein, R. Kautenburger, O. Clemens, H. Hahn, Rare earth and transition metal based entropy stabilised perovskite type oxides, *Journal of the*

- European Ceramic Society. 38 (2018) 2318–2327.
<https://doi.org/10.1016/j.jeurceramsoc.2017.12.058>.
- [17] A.J. Wright, Q. Wang, S.T. Ko, K.M. Chung, R. Chen, J. Luo, Size disorder as a descriptor for predicting reduced thermal conductivity in medium- and high-entropy pyrochlore oxides, *Scripta Materialia*. 181 (2020) 76–81.
<https://doi.org/10.1016/j.scriptamat.2020.02.011>.
- [18] A.J. Wright, Q. Wang, C. Huang, A. Nieto, R. Chen, J. Luo, From high-entropy ceramics to compositionally-complex ceramics: A case study of fluorite oxides, *Journal of the European Ceramic Society*. 40 (2020) 2120–2129.
<https://doi.org/10.1016/j.jeurceramsoc.2020.01.015>.
- [19] K. Balasubramanian, S. v. Khare, D. Gall, Valence electron concentration as an indicator for mechanical properties in rocksalt structure nitrides, carbides and carbonitrides, *Acta Materialia*. 152 (2018) 175–185. <https://doi.org/10.1016/j.actamat.2018.04.033>.
- [20] H.O. Pierson, *Handbook of refractory carbides and nitrides : properties, characteristics, processing, and applications*, Noyes Publications, 1996.
- [21] L. Skala, P. Capkovich, *Nitrogen vacancy and chemical bonding in substoichiometric vanadium nitride*, 1990.
- [22] A.B. Mei, H. Kindlund, E. Broitman, L. Hultman, I. Petrov, J.E. Greene, D.G. Sangiovanni, Adaptive hard and tough mechanical response in single-crystal B1 VN_x ceramics via control of anion vacancies, *Acta Materialia*. 192 (2020) 78–88.
<https://doi.org/10.1016/j.actamat.2020.03.037>.
- [23] H. Holleck, Material selection for hard coatings, *Journal of Vacuum Science & Technology A: Vacuum, Surfaces, and Films*. 4 (1986) 2661–2669.
<https://doi.org/10.1116/1.573700>.
- [24] H.E. Hintermann, Adhesion, friction and wear of thin hard coatings, *Wear*. 100 (1984) 381–397. [https://doi.org/10.1016/0043-1648\(84\)90023-1](https://doi.org/10.1016/0043-1648(84)90023-1).
- [25] C.M. Rost, J. Braun, K. Ferri, L. Backman, A. Giri, E.J. Opila, J.P. Maria, P.E. Hopkins, Hafnium nitride films for thermoreflectance transducers at high temperatures: Potential based on heating from laser absorption, *Applied Physics Letters*. 111 (2017) 151902.
<https://doi.org/10.1063/1.5006648>.
- [26] A. Ciriello, V. v. Rondinella, D. Staicu, J. Somers, O. Benes, R. Jardin, D. Bouëxière, F. Wastin, E. Colineau, Thermophysical characterization of ZrN and (Zr,Pu)N, *Journal of Alloys and Compounds*. 473 (2009) 265–271.
<https://doi.org/10.1016/j.jallcom.2008.05.077>.
- [27] E. Wuchina, E. Opila, M. Opeka, W. Fahrenholtz, I. Talmy, UHTCs: Ultra-High Temperature Ceramic materials for extreme environment applications, *Electrochemical Society Interface*. 16 (2007) 30–36. <https://doi.org/10.1149/2.f04074if>.

Chapter 1: A universal configurational entropy metric for high-entropy materials

Olivia F. Dippo¹, Kenneth S. Vecchio^{1,2*}

Affiliations:

¹ Materials Science and Engineering Program, UC San Diego, La Jolla CA 92093, USA.

² Department of NanoEngineering, UC San Diego, La Jolla CA 92093, USA

*Corresponding author: kvecchio@eng.ucsd.edu

Abstract

In recent years, high-entropy materials have become increasingly complex, outgrowing simple solid-solution based calculations of configurational entropy, and with that, the previously established metrics for high-, medium-, and low-entropy. Those previous metrics are derived from metals-specific approximations of the entropy of fusion and the internal energy of a monatomic gas, and thus, do not apply to other materials. A new entropy metric is proposed that is universally applicable for crystalline materials, from simple solid-solution high-entropy alloys to high-entropy materials with complex crystal structures and multiple sublattices. Additionally, the methods for calculating configurational entropy in complex crystal structures are discussed.

1.1 Main Text

High-entropy materials with increasingly complex crystal structures have become more prevalent in recent years. High-entropy materials initially started with high-entropy alloys [1],

and later those concepts were adapted by the high-entropy ceramics communities. High-entropy ceramics with simple crystal structures were synthesized first, with 1:1 ratios of metals to anions, in materials such as oxides [2], carbides [3], and nitrides [4]. Most of these materials have 5 metal elements and a single anion, though multiple cations and multiple anions are possible [5,6]. There also exist single-anion high-entropy ceramics with a 2:1 metal to anion ratio such as borides and silicides [7–9]. High-entropy versions of more complex crystal structures are being explored now such as silicates [10], fluorite oxides [11], pyrochlores [12], and perovskite oxides [13–16].

Entropy calculation is essential to the prediction of Gibb's free energies, energetically favorable phases, and whether increased entropy can stabilize a given phase [2,17]. Entropy is also important for entropy-related material behaviors: the cocktail effect, shifting melting temperatures [18,19], enhanced mechanical properties [20,21], and more. Due to these interesting properties, configurational entropy values have been used to classify materials as high-entropy when the configurational entropy of the solid material is greater than $1.5R$; this entropy metric will be revisited in more detail later.

However, within the fields of high-entropy materials, there exist some inconsistencies in calculation of this ideal configurational entropy value. In this paper we will discuss the 3 methods of calculating configurational entropy for materials with complex crystal structures: the single-lattice model, the sublattice model calculated per mole of formula unit, and the sublattice model calculated per mole of atom. We will dissect each model's assumptions and implications, and propose a new metric for what constitutes a high-entropy material. This novel entropy metric can be applied to complex high-entropy crystal structures with multiple atom positions and is still consistent with simpler crystal structures.

First, we will discuss the single-lattice model of configurational entropy, also sometimes referred to as the solid-solution model. This model is described by Murty, Yeh, and Ranganathan [1]; the ideal configurational entropy is defined based on the mole fraction of each element (X_i).

$$S_{SS}^{config} = -R \sum_i X_i \ln (X_i) \quad (Eq.1.1)$$

Eq.1.1 relies on the assumption that the components are equally likely to be in any lattice position. If those components are also in equal atomic proportion to one another, or equiatomic, Equation 1.1 reduces to Equation 1.2, defined simply based on the number of components, or ‘entropic species’ (n) in the system.

$$S_{SS}^{config} = -R \ln(n) \quad (Eq.1.2)$$

The metallic high-entropy alloys for which this equation was written exist as FCC and BCC crystal structures containing one atom per formula unit. Each species in the system is an element, i.e. one metal atom. However, the solid solution model has been used to describe ceramic systems with more than one atom per compound, which requires considering each compound (such as TiC or SrTiO₃) as one entropic species.

To examine this point, it is necessary to define an entropic species. Entropic species can be defined as an atom or a molecule [22]. However, the molecule definition requires that the elements within that compound do not dissociate from one another in the material system of interest. Take for example a simple solution of salt and water; upon dissolution, the Na⁺ and Cl⁻ ions will dissociate from one another, and each will function alongside H₂O as a separate entropic species (totaling three species, instead of the two that might be assumed if NaCl were not an ionic constituent). Analogous to dissociated ions in aqueous solutions, in ceramic applications, atoms in different sites within the compound exhibit different behaviors or

properties. For example, in carbides the anions and cations that make up the compound have different rates of diffusion and vacancy formation [23]. Additionally, at high temperatures, before melting, vacancy formation occurs first due to anion loss, as a result of the increase in entropy associated with vacancy formation [24,25]. Therefore, each element within the material is defined as an entropic species. For example, a 5-metal high-entropy carbide $(\text{HfZrTiNbTa})_1\text{C}_1$ would have 6 entropic species: Hf, Zr, Ti, Nb, Ta, and C. If there is a significant number of vacancies present, vacancies can be considered an additional species. Previous studies which have considered the monocarbide compounds as entropic species (HfC, ZrC, TiC, NbC, TaC) are unable to describe entropy changes with respect to compositional differences that occur separately for metals and anions in these materials or the entropic phenomena leading to melting.

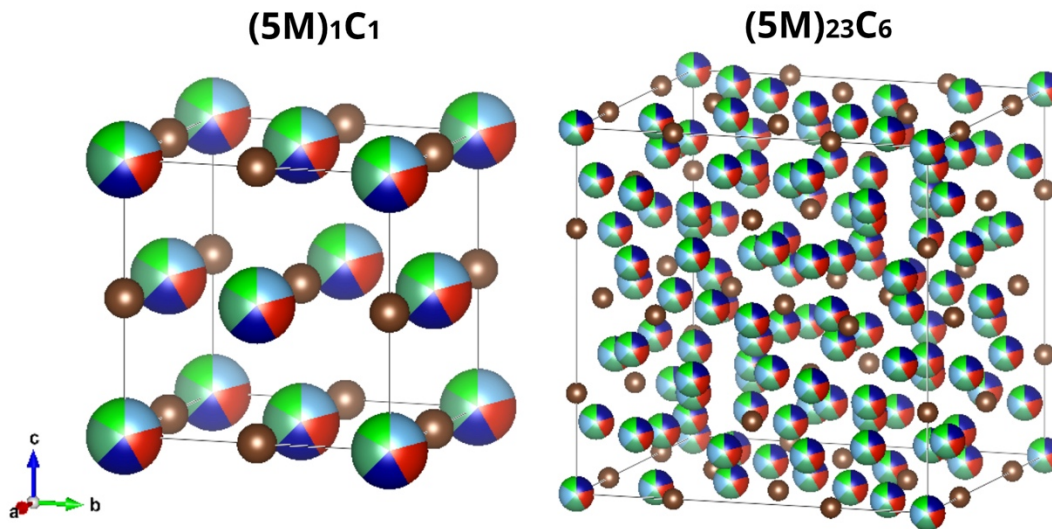


Figure 1.1: (left) 5-metal carbide with a 1:1 metal to anion ratio, (right) 5-metal carbide with a 23:6 metal to anion ratio, with the structure of M_{23}C_6 .

Furthermore, the additional impetus for defining an entropic species as an element, not as a compound, is to understand any entropy gain that occurs within the compound and as a result of different structural configurations. If a compound is considered to be an entropic species, it

becomes impossible to distinguish entropy values for compounds of different structures and stoichiometries. For example, consider the fabrication of a 1:1 metal to anion ratio ceramic, with five metals, such as a carbide with the form $(5M)_1C_1$. Carbides and many other ceramics form multiple stable polymorphs: for example, a 23:6 compound similar to $M_{23}C_6$ containing the same 5 metal elements. If compounds are used as entropic species, there would be no difference in the configurational entropy of the two materials $(5M)_1C_1$ and $(5M)_{23}C_6$, shown in Figure 1.1. This constitutes a critical loss of information regarding any configurational entropy changes within the formula unit. The varying crystal structures and ratios of atoms between the two materials inherently changes the number of possible energetically distinct atomic configurations, and hence the configurational entropy. Thus, when using a compound as an entropic species, any compound, regardless of crystal structure, number of atoms in the compound, or atomic ratio, will be assigned the same configurational entropy value. If all compounds have the same configurational entropy value, using entropy and Gibb's free energy to evaluate the relative stability of competing phases becomes impossible, such as M_1C_1 vs $M_{23}C_6$ discussed here. Lastly, this method cannot accommodate point defects as entropic species, which are known to occur in significant amounts on specific lattices in ceramics [24], and which have caused measurable contributions to entropy-related properties such as melting temperature [18].

To avoid the information loss regarding configurational entropy within a compound, it is necessary to define an entropic species as an element in crystalline materials. In addition, the constrained atom positions present in a crystalline compound must be taken into account. For example, in a face-centered cubic rock salt structured M_1C_1 compound, the metal (M) atoms are at the (0,0,0) position, and the carbon (C) atoms are in the (1/2,1/2,1/2) position. These constrained atom positions are referred to as lattice sites or occupy a sublattices within the

structure, and certain atoms will only occupy certain sublattices. The corresponding model for calculating configurational entropy is often referred to as the sublattice (SL) model and is defined as [26–28]:

$$S_{SL}^{config} = \frac{-R \sum_S \sum_i a^S X_i^S \ln(X_i^S)}{\sum_S a^S} \quad (Eq. 1.3)$$

In Equation 1.3, a^s is the number of sites on the s sublattice, and X_i^s is the fraction of element species i randomly distributed on the s sub-lattice, or the site fraction. This model reduces to the solid solution model (Eq. 1.1) for the case of only one possible crystallographic atomic position, or sublattice, as in most metallic high-entropy alloys. The units of S_{SL}^{config} are J/(K*mol of atoms). In some works, a slightly modified equation is used wherein there is no denominator; this changes the units of S_{SL}^{config} to J/(K*mol of formula units) [17].

Inconsistencies arise when calculating entropy per mole of formula units, because the entropy increases with the number of atoms in the formula unit, instead of with the number of energetically distinct atomic configurations, and this prevents comparison of entropy or free energies between crystal systems. For example, for the case of $(5M)_1C_1$ and $(5M)_{23}C_6$, entropy per mole of atoms is $0.8R$ and $1.28R$, respectively, and entropy per mol of formula units is $1.61R$ and $37.0R$, respectively. As high-entropy material crystal structures increase in complexity and more composite high-entropy materials are developed, the consistency between crystal structures offered by the sublattice calculation of entropy per mole of atoms becomes necessary.

Configurational entropy values have been used to classify materials as high-entropy ($>1.5R$), medium entropy ($1 - 1.5R$), and low entropy ($<1R$) [1]. The classification of high-entropy as $>1.5R$ matches the internal energy per mole of a monoatomic ideal gas, which is equal to $1.5RT$. It is also based on Richard's rule, which states that every metallic material has an

entropy of fusion approximately equal to R [29]. It is theorized that if a metal solid solution can overcome these entropic barriers of $1-1.5R$, then its free energy is significantly lowered, and the material's melting temperature is increased accordingly, thus entropically stabilizing the solid material. The problem arises upon realization that the approximations of a monoatomic gas and Richard's rule do not apply to ceramic materials. Additionally, often enthalpies and entropies of fusion are difficult to measure due to high melting temperatures of ceramic materials. With the limited data on entropy of fusion for these classes of materials, no pattern similar to Richard's rule emerges, perhaps due to the varied types of bonding present in ceramic materials. Ideally, for each compositionally complex material synthesized, researchers would determine the amount of configurational entropy necessary to overcome the entropy of fusion, in order to determine if the material is 'high-entropy'. However, due to the difficulty of obtaining entropy of fusion data for many ceramic materials, this would put an undue burden on the researcher, especially considering that high-entropy materials have found applications beyond high-temperature phase stability. To address these difficulties, a new entropy metric (EM) is proposed, defined as:

$$EM = \frac{S_{SL/mol\ atoms}^{config}}{R} * L \quad (Eq. 1.4)$$

where $S_{SL/mol\ atoms}^{config}$ refers to the configurational entropy calculated using the sublattice model, in units of $J/(K * mol\ atoms)$, R is the ideal gas constant, and L is the total number of sublattices. In continuity with previous high-entropy metrics and high-entropy research, $EM < 1$ denotes low-entropy materials, $1 < EM < 1.5$ denotes medium-entropy materials, and $EM > 1.5$ denotes high-entropy materials.

Table 1.1: Quantification of entropy and new entropy metric. In the structure type examples, (5M), (5N), and similar notation denotes there are 5 species on that particular lattice site. L denotes the number of sublattices in the material, $\sum_S a^S$ denotes the total number of atoms per formula unit, and S_{config}/R denotes the configurational entropy per mol of atoms. EM represents the new entropy metric as calculated in Eq. 1.4. High-entropy compounds with $EM > 1.5$ are highlighted in green, medium-entropy with $1 < EM < 1.5$ in yellow, and low-entropy with $EM < 1$ in red.

Structure type	L	$\sum_S a^S$	S_{config}/R	EM	EM classification
(5M) [metal]	1	1	1.61	1.61	high-entropy EM>1.5
(5M) ₁ C ₁ [carbide]	2	2	0.80	1.61	high-entropy EM>1.5
(5M) ₁ (CN) ₁ [carbonitride]	2	2	1.15	2.30	high-entropy EM>1.5
(5M) ₁ Si ₂ [silicide]	2	3	0.54	1.07	medium-entropy 1<EM<1.5
(5M) ₁ B ₁ O ₃ [perovskite]	3	5	0.32	0.97	low-entropy EM<1
(5M) ₁ (5N) ₁ O ₃ [perovskite]	3	5	0.64	1.93	high-entropy EM>1.5
(5M) ₃ O ₄ [spinel]	2	7	0.69	1.38	medium-entropy 1<EM<1.5
(5M) ₂ B ₁ O ₄ [spinel]	3	7	0.46	1.38	medium-entropy 1<EM<1.5
A ₂ (5M) ₁ O ₄ [spinel]	3	7	0.23	0.69	low-entropy EM<1
(5M) ₂ (5N) ₁ O ₄ [spinel]	3	7	0.69	2.07	high-entropy EM>1.5
(5M) ₂ (5N) ₁ (5O) ₄ [spinel]	3	7	1.61	4.83	high-entropy EM>1.5

Table 1.1 provides examples of different types of high-entropy materials, with formula units that increase in complexity. For materials with one sublattice, such as high-entropy solid solution metals, EM is equal to S/R , indicating that this metric is consistent with previous high-entropy cutoffs. For materials with more than one sublattice, “high-entropy” can be achieved by having many element species on one sublattice, or by having low- to medium-entropy on multiple sublattices. This metric, for materials with multiple sublattices, also captures the ratios of atomic sites, as a higher proportion of sites with no configurational entropy (i.e. only one species) will lower the entropy of the system. For example, in a material with a 23:6 ratio of metals to anions, like the carbide $M_{23}C_6$, achieving “high-entropy” will require 3 metals with 1 anion, or 1 metal with 38 anions. Additionally, if multiple sublattices have many atomic species, such as the perovskite structure $(5M)_2(5N)_1(5O)_4$ shown in Table 1.1, the EM metric can quantify that entropy gain. This overcomes the main drawback of the previously used technique of simply ensuring one sublattice has 5 atomic species in order to classify a material as high-entropy, as EM classification allows for quantification of the whole system.

EM classification captures physical phenomena that are important to high-entropy systems. In many high-entropy ceramics, important entropic effects have been observed. Rost *et al.*'s entropy-stabilized oxide $(MgNiCoZnCu)O$, with $EM=1.61$, showed a reversible high-temperature entropically-driven phase transformation [2], as did Sarkar *et al.*'s entropy-stabilized perovskite oxide, $EM=1.93$ [16]. However, it should be noted that it has been debated whether this effect is entropy stabilization or enthalpy destabilization [17]. In addition to phase stability, other high-entropy effects have been isolated, including reduced thermal conductivity in oxides ($EM=0.59-2.61$) [12,15], and increased hardness [29,30] and elastic modulus in bulk carbides and nitrides ($EM=1.61$) and carbonitrides ($EM=2.30$) [5].

The limitations of this work should be acknowledged, in that the entropy calculations discussed are purely for ideal configurational entropy. The assumption of an ideal material means neglecting any deviation from completely homogeneous, random mixing of elements on each sublattice; this assumption may not hold true, depending on the tendency for a material to exhibit preferential bonding or short-range ordering. Furthermore, there are additional contributions to entropy, including vibrational, magnetic, and electronic entropy, although these other contributions are often negligible. Vibrational entropy is about an order of magnitude less than configurational entropy in multi-component solid materials [3,31], approximately $0.1-0.2R$ per mole of atoms in substitutional alloys [32]. Magnetic contributions to entropy can occur in magnetic materials upon application of a magnetic field [33]. Electronic entropy relates to probabilistic occupation of electronic states; in a study on the perovskite $\text{La}_{0.8}\text{Sr}_{0.2}\text{CoO}_{3-x}$, electronic entropy was undetectable compared to configurational entropy changes [34]. Ideal configurational entropy's predominance over other entropic contributions and its dependence only on composition and atomic positions make configurational entropy advantageous for establishing a universal entropy metric.

This work has reconciled calculations of configurational entropy, along with their assumptions and implications, and recommends calculating entropy per mole of atoms using the sublattice model as the method giving consistent results. A new entropy metric (EM) is established for determination of high-entropy, medium-entropy, and low-entropy status of complex crystal structures with multiple sublattices. This metric is consistent with previous high-entropy metrics as established for solid-solution high-entropy alloys, and also facilitates quantification of the configurational entropy of a system with multiple sublattices as a whole. It is consistent with the current understanding in the field of high-entropy ceramics that not every

sublattice needs to have high entropy [11], but removes the limitation requiring one sublattice to have 5 atomic species. The methods, examples, and explanations used herein focus on ceramic materials and their crystal structures. However, the methods and results should apply consistently to any crystalline solid, from complex crystal structures to simple solid solutions.

Acknowledgements:

The authors would like to acknowledge Dr. Matthew J. Powell-Palm, Dr. Tyler Harrington, Dr. Daniel Miracle, William Mellor, and Kevin Kaufmann for useful discussions, and Wenyong Jiang for literature search assistance. This work was funded by the Office of Naval Research ONR-MURI (Grant No. N00014-15-1-2863).

Chapter 1, in full, is a reprint of the material “A universal configurational entropy metric for high-entropy materials” as it appears in *Scripta Materialia*. Dippo, Olivia F.; Vecchio, Kenneth S., 2021. The dissertation author was the primary investigator and author of this paper.

References:

- [1] B.S. Murty, J.W. Yeh, S. Ranganathan, High Entropy Alloys, Elsevier, 2014.
- [2] C.M. Rost, E. Sachet, T. Borman, A. Moballeggh, E.C. Dickey, D. Hou, J.L. Jones, S. Curtarolo, J.P. Maria, Nature Communications 6 (2015) 1–8.
- [3] P. Sarker, T. Harrington, C. Toher, C. Oses, M. Samiee, J.-P. Maria, D.W. Brenner, K.S. Vecchio, S. Curtarolo, Nature Communications 9 (2018) 4980.
- [4] C.H. Lai, S.J. Lin, J.W. Yeh, S.Y. Chang, Surface and Coatings Technology 201 (2006) 3275–3280.
- [5] O.F. Dippo, N. Mesgarzadeh, T.J. Harrington, G.D. Schrader, K.S. Vecchio, Scientific Reports 10 (2020) 1–11.

- [6] S.Y. Lin, S.Y. Chang, Y.C. Huang, F.S. Shieu, J.W. Yeh, *Surface and Coatings Technology* 206 (2012) 5096–5102.
- [7] Y. Qin, J.X. Liu, F. Li, X. Wei, H. Wu, G.J. Zhang, *Journal of Advanced Ceramics* 8 (2019) 148–152.
- [8] J. Gild, J. Braun, K. Kaufmann, E. Marin, T. Harrington, P. Hopkins, K. Vecchio, J. Luo, *Journal of Materiomics* (2019).
- [9] J. Gild, Y. Zhang, T. Harrington, S. Jiang, T. Hu, M.C. Quinn, W.M. Mellor, N. Zhou, K. Vecchio, J. Luo, *Scientific Reports* 6 (2016).
- [10] X. Ren, Z. Tian, J. Zhang, J. Wang, *Scripta Materialia* 168 (2019) 47–50.
- [11] A.J. Wright, Q. Wang, C. Huang, A. Nieto, R. Chen, J. Luo, *Journal of the European Ceramic Society* 40 (2020) 2120–2129.
- [12] A.J. Wright, Q. Wang, S.T. Ko, K.M. Chung, R. Chen, J. Luo, *Scripta Materialia* 181 (2020) 76–81.
- [13] Y. Sharma, B.L. Musico, X. Gao, C. Hua, A.F. May, A. Herklotz, A. Rastogi, D. Mandrus, J. Yan, H.N. Lee, M.F. Chisholm, V. Keppens, T.Z. Ward, *Physical Review Materials* 2 (2018) 1–6.
- [14] S. Jiang, T. Hu, J. Gild, N. Zhou, J. Nie, M. Qin, T. Harrington, K. Vecchio, J. Luo, *Scripta Materialia* 142 (2018) 116–120.
- [15] R. Banerjee, S. Chatterjee, M. Ranjan, T. Bhattacharya, S. Mukherjee, S.S. Jana, A. Dwivedi, T. Maiti, *ACS Sustainable Chemistry and Engineering* 8 (2020) 17022–17032.
- [16] A. Sarkar, R. Djenadic, D. Wang, C. Hein, R. Kautenburger, O. Clemens, H. Hahn, *Journal of the European Ceramic Society* 38 (2018) 2318–2327.
- [17] S.J. McCormack, A. Navrotsky, *Acta Materialia* 202 (2021) 1–21.
- [18] Q.-J. Hong, A. van de Walle, *RAPID COMMUNICATIONS PHYSICAL REVIEW B* 92 (2015) 20104.
- [19] O. Cedillos-Barraza, D. Manara, K. Boboridis, T. Watkins, S. Grasso, D.D. Jayaseelan, R.J.M. Konings, M.J. Reece, W.E. Lee, *Scientific Reports* 6 (2016) 1–11.
- [20] E. Castle, T. Csanádi, S. Grasso, J. Dusza, M. Reece, *Scientific Reports* 8 (2018).
- [21] T.J. Harrington, J. Gild, P. Sarker, C. Toher, C.M. Rost, O.F. Dippo, C. McElfresh, K. Kaufmann, E. Marin, L. Borowski, P.E. Hopkins, J. Luo, S. Curtarolo, D.W. Brenner, K.S. Vecchio, *Acta Materialia* 166 (2019).
- [22] D.R. Gaskell, *Introduction to the Thermodynamics of Materials*, 5th ed., Taylor & Francis, New York, NY, 2008.

- [23] Hj. Matzke, *Diffusion in Materials* (1990) 429–455.
- [24] H.O. Pierson, *Handbook of Refractory Carbides and Nitrides : Properties, Characteristics, Processing, and Applications*, Noyes Publications, 1996.
- [25] K. Balasubramanian, S. v. Khare, D. Gall, *Acta Materialia* (2018).
- [26] D.B. Miracle, O.N. Senkov, *Acta Materialia* 122 (2017) 448–511.
- [27] M. Temkin, *Acta Physicochimica USSR* (1945) 411–420.
- [28] M. Hillert, L.-I. Staffanson, *Acta Chemica Scandinavica* 24 (1970) 3618–3626.
- [29] T.J. Harrington, J. Gild, P. Sarker, C. Toher, C.M. Rost, O.F. Dippo, C. McElfresh, K. Kaufmann, E. Marin, L. Borowski, P.E. Hopkins, J. Luo, S. Curtarolo, D.W. Brenner, K.S. Vecchio, *Acta Materialia* 166 (2019) 271–280.
- [30] Y. Wang, T. Csanádi, H. Zhang, J. Dusza, M.J. Reece, R.Z. Zhang, *Advanced Theory and Simulations* 2000111 (2020) 1–8.
- [31] M.C. Gao, C. Zhang, P. Gao, F. Zhang, L.Z. Ouyang, M. Widom, J.A. Hawk, *Current Opinion in Solid State and Materials Science* 21 (2017) 238–251.
- [32] A. van de Walle, G. Ceder, *Reviews of Modern Physics* 74 (2002) 11–45.
- [33] M. Dhahri, J. Dhahri, E.K. Hlil, *RSC Advances* 8 (2018) 5395–5406.
- [34] M.H.R. Lankhorst, H.J.M. Bouwmeester, H. Verweij, *Solid State Ionics* 96 (1997) 21–27.

Chapter 2: Bulk high-entropy nitrides and carbonitrides

Olivia F. Dippo,¹ Neda Mesgarzadeh,¹ Tyler J. Harrington,¹ Grant D. Schrader,²

Kenneth S. Vecchio,^{1,2,*}

Affiliations:

¹Materials Science and Engineering Program, UC San Diego, La Jolla CA 92037

²Department of NanoEngineering, UC San Diego, La Jolla CA 92037

Abstract

High-entropy ceramics have potential to improve the mechanical properties and high-temperature stability over traditional ceramics, and high entropy nitrides and carbonitrides (HENs and HECNs) are particularly attractive for high temperature and high hardness applications. The synthesis of 5 bulk HENs and 4 bulk HECNs forming single-phase materials is reported herein among 11 samples prepared. The hardness of HENs and HECNs increased by an average of 22% and 39%, respectively, over the rule-of-mixtures average of their monocarbide and mononitride precursors. Similarly, elastic modulus values increased by an average of 17% in nitrides and 31% in carbonitrides over their rule-of-mixtures values. The enhancement in mechanical properties is tied to an increase in the configurational entropy and a decrease in the valence electron concentration, providing parameters for tuning mechanical properties of high-entropy ceramics.

2.1 Introduction

High entropy ceramics have been gaining traction in recent years,[1,2] since Rost *et al.* adapted the idea of high-entropy alloys [3,4] to synthesize the first entropy-stabilized oxide[5]. The field of bulk high-entropy ceramics has grown to include borides[6], carbides [7–11], silicides [12,13], perovskite oxides [14], and fluorite oxides [15]. Many of these bulk high-entropy ceramics have increased hardness over their constituents [6,7,9], and have the potential for increased phase stability at high temperatures [16], according to the increased entropy term (S) in the Gibb’s free energy equation $G = H-TS$.

Transition metal nitrides and carbonitrides are used for their high hardness, wear resistance, and refractory character - having melting temperatures over 1800°C [17], with some having melting temperatures above 4000°C [18]. High-entropy versions of these materials show potential to augment their already high hardness and thermal stability, making them promising candidates for leading edges and thermal protective components in aerospace applications, which require bulk materials [19]. HENs have been synthesized as a powder [20] and as thin films [21–36]; HECNs have also been synthesized as thin films [37,38]. High-entropy nitrides (HENs) and high-entropy carbonitrides (HECNs) have not been synthesized in bulk form until recently, when a paper by Wen *et al.* reported the synthesis of one bulk HEN composition and one bulk HECN composition, (HfNbTaTiZr)N and (HfNbTaTiZr)CN, respectively [39]. In addition to these compositions, we report the first bulk synthesis of 4 other HECN compositions and 3 other HEN compositions.

HENs and HECNs in particular offer interesting opportunities for tuning mechanical properties over existing bulk high-entropy ceramics, the first of which is their configurational entropy. Higher configurational entropy is associated with favorable “high-entropy” material

behavior, such as increased strength and phase stability. Methods for calculating ideal configurational entropy of high-entropy ceramic compositions will be discussed in this paper, which indicate that the configurational entropy of a carbonitride is significantly higher than that of a nitride or carbide. The ideal configurational entropy for an equiatomic and stoichiometric five-metal nitride is $0.8R$, and for a carbonitride is $1.15R$, where R is the gas constant. This entropy increase upon addition of a second anion to a high-entropy ceramic system is equal to that of adding five additional metal species, giving carbonitrides a major advantage in entropy-related properties.

In addition to entropy, valence electron concentration (VEC) provides an opportunity for tuning mechanical properties, where HENs have the advantage of a higher VEC. Transition metal nitrides, carbides, and carbonitrides have mixed bond character, considered partially covalent, ionic, and metallic. This gives rise to many of the interesting properties of these materials, for example maintaining the high melting temperatures of ionic/covalently bonded materials and the high thermal and electrical conductivity of metallic materials [17]. Changing the composition of the HEN or HECN can shift the bond character, which can be quantified using the material's VEC – calculated as the number of valence electrons per formula unit. VEC can be manipulated by varying the metals contained in the ceramic, and in addition, nitrogen has one more valence electron than carbon, giving HECNs and HENs higher VECs than high-entropy carbides. Increasing VEC in cubic carbides, nitrides, and carbonitrides decreases hardness [9,40] and increases toughness [41]. Therefore, HENs, having higher nitrogen content and thus higher VEC than carbon-containing high-entropy ceramics, should display lower hardness, thus indicating potential for future synthesis of more ductile ceramics.

The aim of this study is twofold: (i) to report the first synthesis of five bulk HENs and six bulk HECNs, and (ii) to elucidate the effect of configurational entropy and VEC on the mechanical properties of bulk high-entropy ceramics. Consistent with the current literature on bulk high-entropy ceramics, the single-phase character of all HENs and HECNs will be analyzed. A single-phase high-entropy material is defined as having one majority crystal structure and a homogeneous distribution of elements within the material; conditions chosen to ensure that randomness, and therefore configurational entropy, is maximized. Bulk high-entropy ceramics are often equiatomic, i.e. all elements are in equal atomic proportions, though this is not a requirement to categorize a high-entropy ceramic as single-phase. In this work, single-phase or multi-phase character of these novel HENs and HECNs is experimentally determined for all 11 samples through XRD and EDS. Additionally, nanoindentation hardness and elastic modulus data are presented, in comparison with expected rule of mixtures (ROM) averages of the constituents of each composition. Mechanical properties are also analyzed in terms of configurational entropy and VEC, defining trends that may influence future design of ceramic materials.

2.2 Materials & Methods

2.2.1 Synthesis:

Precursor powders of graphite, CrN, CrC, HfC, Mo₂C, NbN, NbC, TaN TaC, TiN, TiC, VC, W₂C, ZrN, and ZrC were procured from Alfa Aesar (>99% purity); HfN was procured from Reade Advanced Materials (99.5% purity); VN was procured from American Elements (99% purity).

For nitride and carbonitride compositions listed as HENs #1-5 and HECNs #1-6 respectively, appropriate amounts of precursor powders were hand-mixed, to achieve an equiatomic mixture, calculated on the metals basis. An additional 5 atomic percent graphite powder was added to all of the samples, to aid in sintering and reduce oxides present in the precursor powders. To achieve particle size reduction and improved blending, hand-mixed powders were then high-energy ball milled using a SPEX 8000D mill (SpexCertPrep, NJ, USA) for three hours total, in increments of 30 minutes with 10-minute cool-down periods in between. Tungsten carbide milling media was used (ball to powder ratio 2:1), and stearic acid was added as a lubricant to the milling process. The SPEX milling and subsequent powder handling was done in an argon glove box to prevent oxidation.

Powders were then densified using spark plasma sintering (SPS, Thermal Technologies, CA, USA) under vacuum (below 30 mtorr) using a temperature ramp rate of 100°C/min and held at temperature for 1 hour under a pressure of 50 MPa. During heating, whenever significant sample off-gassing occurred, heating was paused to allow the vacuum level to stay below 30 mtorr. Chromium containing compositions were sintered at a maximum temperature of 1600°C, and compositions that did not contain chromium were sintered at 2200°C. Mononitrides (defined as containing one transition metal, for example CrN) were each synthesized in the SPS at approximately 300°C below their respective melting temperatures. Samples were sintered in 20-mm graphite dies lined with graphite foil. The outside surfaces of sintered samples were ground away using an 80-grit diamond grinding disc, to remove residual carbon contamination before characterization.

2.2.2 Characterization:

Crystal structures of sintered samples were characterized using powder X-ray diffraction (XRD) in a Rigaku Miniflex diffractometer with Cu K- α radiation. Microstructure and metal content were characterized in a scanning electron microscope (SEM) (Apreo, Thermo-Fisher) with energy dispersive X-ray spectroscopy (EDS) (Oxford Instruments). Densities were measured using Archimedes method; chemical analysis of carbon and nitrogen content were characterized using a Perkin Elmer 2400 Series II CHNS/O Elemental Analyzer (CHNS).

2.2.3 Mechanical testing:

Bulk, sintered samples were first ground and polished using diamond media, with an 0.04 μm colloidal silica suspension final polish. Nanoindentation according to the Oliver & Pharr method [42] was performed using 300mN force to obtain asymptotic hardness, avoiding indentation size effects, which are present below 100 mN, as shown in Supplementary Figure 2.3. Nanoindentation was performed with a diamond Berkovich indenter in accordance with the ISO 14577 standard. On each sample, a grid of 100 indents were done, spaced 30 μm apart, and the typical indentation depth was approximately 800 nm. Outliers were removed by removing data points with an indentation depth greater than 1400 nm, which were confirmed by optical microscopy to have intersected pores near the surface. The maximum and minimum 5% of data points were removed before averaging the values. Removing outliers in this fashion was necessary for the mononitrides, which had lower sintered densities than the high-entropy compositions, causing more outliers in the low end of the data and artificially lowering the average nanoindentation results. The nanoindentation data for monocarbides is published in another work by the authors, using comparable synthesis methods and identical indentation

parameters [9]. The rule of mixtures (ROM) values for modulus and hardness comparison were taken as a weighted average value of the mononitride and monocarbide compounds, based on the measured composition of each high-entropy sample. Poisson's ratios for all precursor compounds were gathered from the literature (see Table 2.2), and the average value was used for each high entropy composition. The Poisson's ratios for the high entropy compositions were all within the range of 0.24-0.29.

2.3 Results

2.3.1 Single-phase Formation: Crystal Structure

XRD results in Figure 2.1 show the phase consolidation of the precursor mononitrides and monocarbides into a single FCC phase throughout the processing steps: hand-mixing, ball-milling, and SPS densification, even though many of the precursor compositions do not form a room temperature stable FCC-rocksalt phase on their own and/or have many room-temperature polymorphs. A list of phases present in the precursor powders is provided in Supplementary Table 2.1.

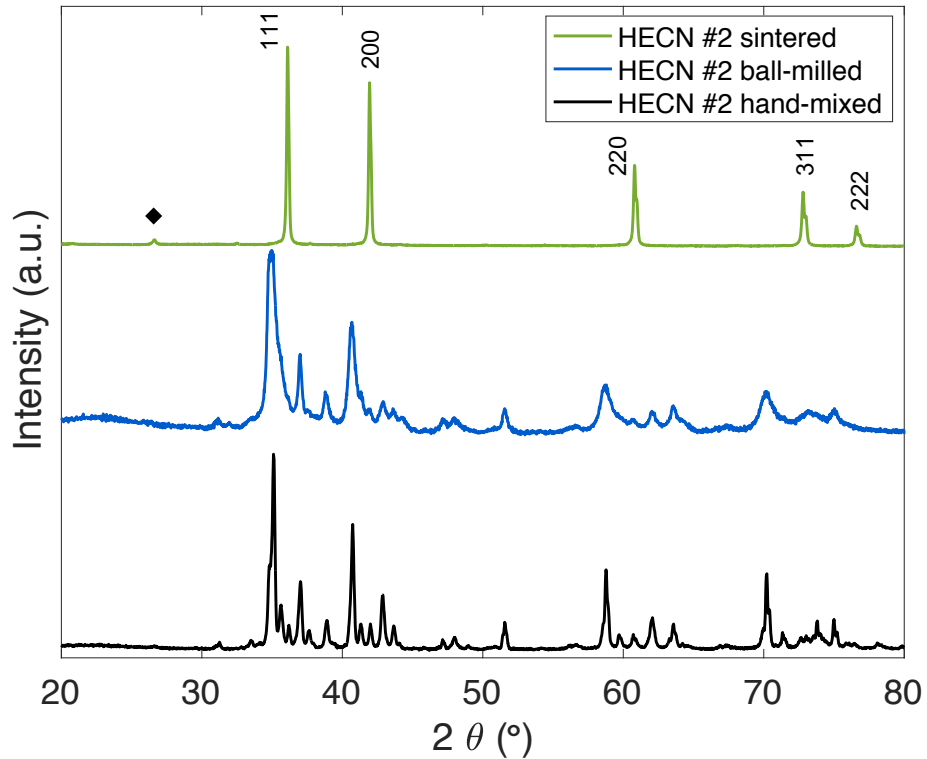


Figure 2.1: Example progression of HECN #2 (CrNbTaTiV)(CN) through the processing steps: hand-mixed (bottom), high-energy ball-milled (middle), and then sintered (top). A residual graphite peak is marked with a black diamond.

After sintering, HEN and HECN samples #1-5 all show a majority FCC-rocksalt phase (Fm-3m), as shown in Figure 2.2. HECN #6 is the only material synthesized with two major crystal structures; it contains an FCC phase and a hexagonal phase. Minor hafnium/zirconium oxide peaks are visible in some XRD patterns; these oxides are native to the precursor powders. For a complete list of all minor oxide phases identified in each material, see Supplementary Table 2.2. Minor graphite peaks are due to the 5 atomic percent graphite powder added as sintering aid and to help reduce native oxides.

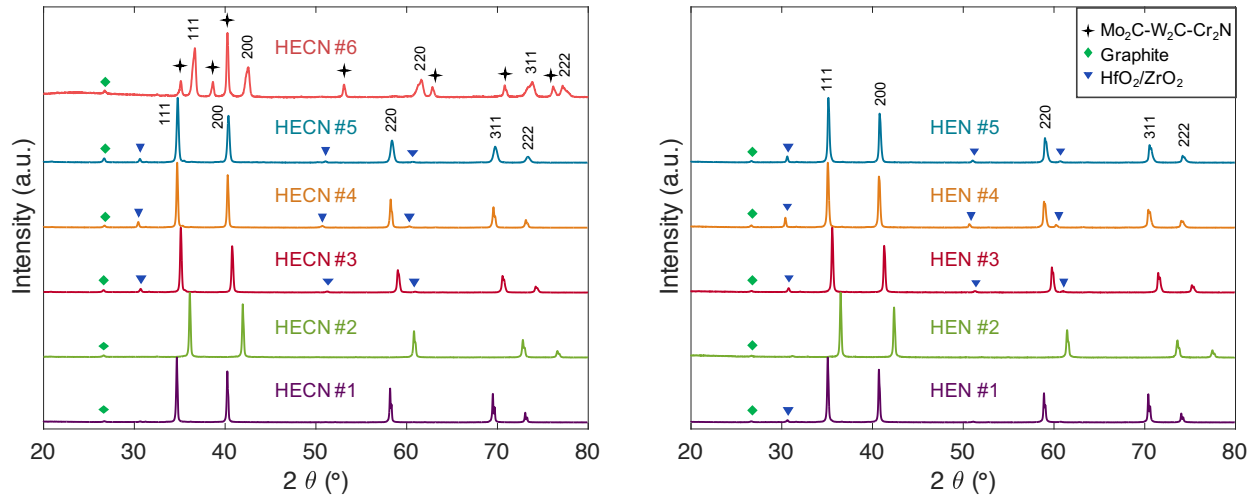


Figure 2.2: XRD of all 6 carbonitride (left) and 5 nitride (right) compositions. HEN and HECN #1-5 are FCC-rocksalt structures, with some residual native oxides present. HECN #6 shows multiple phases. Intensities are normalized by the highest intensity present in each spectrum.

2.3.2 Single-phase Formation: Random Distribution of Elements

To maximize ideal configurational entropy, the sample should be a homogenous mixture, with the elements in equal atomic proportions on each sublattice. First, the homogeneity of the samples will be discussed. EDS maps showing chemical homogeneity of selected compositions are shown in Figure 2.3 (EDS maps of all compositions are shown in Supplementary Figure 2.1); there is a small variation in chemical homogeneity from sample to sample. For example, HEN #2 and HECN #2 have good chemical homogeneity, meaning the elements are randomly distributed, except for a minor chromium oxide phase. Oxygen maps are included to help the reader distinguish which chemical inhomogeneities are due to minor oxide phases, and a list of oxide phases present in each sample is included in Supplementary Table 2.2. The primary matrix structure is close to equiatomic throughout the sample. Both HEN #3 and HECN #3 contain minor amounts of chromium oxide and hafnium oxide, but otherwise the elements in the matrix are homogeneously distributed. In HECN #3, however, there are additional islands of increased

niobium content of about 2 atomic % higher than other regions. Therefore, HECN #3 is not considered to have good compositional homogeneity, and therefore is not truly single-phase, even though there is only one FCC crystal structure present in XRD.

Composition	Electron image	EDS ElementMaps					
HEN #2 (CrNbTaTiV)N		Cr	Nb	Ta	Ti	V	O
HECN #2 (CrNbTaTiV) CN		Cr	Nb	Ta	Ti	V	O
HEN #3 (CrHfNbTaTi)N		Cr	Hf	Nb	Ta	Ti	O
HECN #3 (CrHfNbTaTi) CN		Cr	Hf	Nb	Ta	Ti	O
HECN #6 (CrMoTaVW) CN		Cr	Mo	Ta	V	W	O

Figure 2.3: Secondary electron images and corresponding elemental EDS maps of selected compositions. HEN #2, HECN #2, and HEN #3 have elements homogeneously distributed throughout the matrix, and thus are considered single-phase high-entropy ceramics. HECN #3 contains islands of segregated niobium, thus it does not have the compositional homogeneity required to be single-phase. HECN #6 is a dual phase ceramic, with clear elemental segregation. Oxygen maps are included to indicate the elemental segregation of minor native oxide phases (such as Cr₂O₃ and HfO₂), separate from the high-entropy matrix phases.

To understand why some high-entropy ceramic compositions form a compositionally homogeneous single phase and some do not, the Entropy Forming Ability (EFA) descriptor concept can be employed. Sarker *et al.* created this descriptor to predict how readily specific compositions would form homogeneous single-phase high entropy carbides [10]. The EFA ratings imply that there is a continuum of how easy it is to synthesize a high-entropy ceramic phase with one crystal structure and homogeneous random mixing of elements. Indeed, it was shown by

Kaufmann *et al.* that high-entropy carbides with lower EFA values, displaying some chemical segregation (but only one detectable crystal structure), could be homogenized with a longer annealing time [11]. Similarly, HECN #3 can be considered to be in the middle of the EFA continuum, where it could potentially be synthesized as a homogenous single-phase, but would require more energetic input (i.e. mechanical milling, or time at temperature) during synthesis. Though it is possible to homogenize chemical segregation islands in this way, the differences are pointed out here using identical synthesis processes as these differences may indicate the ease of forming single phase compounds of these compositions, which is an indication of their entropic stability.

As shown in Figure 2.3, HECN #6 demonstrates the most extreme case of chemical segregation, which is not surprising given that two majority crystal structures are seen in XRD. HECN #6 shows clear segregation of elements into two distinct phases. To understand the segregation behavior in HECN #6, the slight difference in synthesis technique for this sample must be noted. Due to limitations in availability of mononitrides, this sample was made using VN, CrN, TaN, Mo₂C, W₂C, and graphite. All other carbonitride samples were made by mixing both the monocarbides and mononitrides of each metal (i.e. the (CrMoTaVW)(CN) sample would have been made with CrN, CrC, MoN, MoC, TaN, TaC, VN, VC, WN, and WC if the precursors were available). Therefore, it is not surprising that the Mo and W cluster together in EDS, matching the hexagonal Mo₂C-W₂C phase present in XRD. Interestingly, the chromium content is relatively homogenous, due to the Cr₂N phase present in the chromium nitride precursor powder, which mixes favorably with the Mo₂C-W₂C phase. One of the biggest challenges in synthesis of bulk HENs and HECNs is the lack of readily available mononitride powders.

2.3.4 Equiatomic phase formation

The composition of each sample in atomic percent can be found in Table 2.1, with metal data from EDS and light element (C, N) data from CHNS combustion analysis. The precursor powders are mixed in equiatomic proportions, but there are some variances in the final sintered compositions. Nitrogen content is consistently lower than equiatomic (50 at% for the nitrides and 25 at% for the carbonitrides), which is consistent with knowledge that nitrogen vacancies are prevalent in nitrides at high temperatures [17,43]. More surprisingly, in some compositions, the chromium content is significantly lower than equiatomic throughout the sample.

Table 2.1: Composition of experimental samples in atomic percent, calculated from EDS analysis of metal content and CHNS chemical analysis of carbon and nitrogen content. Metals are expected to be in equal atomic proportion.

atomic %	C	N	Cr	Hf	Nb	Ta	Ti	V	Zr	Mo	W	C+N subtotal	metals subtotal
HEN #1	9.9	36.7	-	10.9	10.8	10.5	10.6	-	10.8	-	-	46.5	53.6
HEN #2	4.0	41.5	12.0	-	11.0	10.5	10.4	10.7	-	-	-	45.4	54.6
HEN #3	5.9	41.4	6.4	12.0	11.8	10.8	11.6	-	-	-	-	47.3	52.6
HEN #4	6.5	41.2	4.0	11.8	12.2	-	12.6	-	11.6	-	-	47.7	52.2
HEN #5	6.0	41.9	4.7	12.1	-	11.3	12.2	-	11.7	-	-	47.9	52.0
HECN #1	30.0	17.6	-	10.0	10.9	10.4	10.5	-	10.7	-	-	47.5	52.5
HECN #2	26.4	18.5	10.3	-	11.1	10.7	11.7	11.4	-	-	-	44.9	55.2
HECN #3	27.8	19.8	5.4	12.2	11.8	11.7	11.3	-	-	-	-	47.6	52.4
HECN #4	27.7	19.8	2.7	12.4	12.9	0	12.2	-	12.4	-	-	47.4	52.6
HECN #5	29.1	18.0	3.7	12.2	-	12.1	12.5	-	12.4	-	-	47.1	52.9
HECN #6	32.1	7.4	12.1	-	-	12.1	0.0	11.8	-	12.3	12.2	39.5	60.5

All chromium-containing compounds were sintered under the same conditions: 1600°C under vacuum for 1 hour, as detailed in the Methods section of this work. If the high-entropy composition is not stable at this temperature, chromium will tend to evaporate. This can happen via one of two pathways: carbothermal reduction of Cr₂O₃ to form chromium metal and carbon

monoxide gas, and then chromium metal vaporization, which occurs at temperatures above 825°C under vacuum [44], or significant nitrogen evaporation in chromium nitride and subsequent chromium metal evaporation. Chromium is the most sensitive element because chromium nitride and chromium carbide have the lowest melting temperatures of all the precursors.

Atomic proportion of elements does not affect whether a high-entropy ceramic is considered single-phase, but it can act as an indicator of high-temperature stability of the compound. If the high-entropy ceramic phase is stable at high temperatures, it will tend to maintain its equiatomic composition, as in HEN #2 and HECN #2, which did not lose chromium content during synthesis, i.e. maintained equiatomic character. This may be used as an indicator of high-temperature phase stability, and is also a characteristic of having a higher EFA value, as Kaufmann *et al.* noted chromium loss in lower EFA carbides [11]. High-temperature phase stability and thus increased melting temperatures are theorized to be an asset of high-entropy systems, due to the increased contribution of entropy (S) to the Gibb's free energy $G = H - TS$ at high temperatures [16]. However, it should be noted that we have not determined that these HENs and HECNs are entropy-stabilized, as carbides and nitrides have some mutual solubility [17] as well as strong enthalpic contributions to phase stability [10].

2.3.5 Mechanical Properties

Nanoindentation was performed on all ten of the FCC-structured compositions, i.e. HENs #1-5 and HECNs #1-5. In order to compare the mechanical properties of the high-entropy nitrides and carbonitrides to the properties of their constituents, each monocarbide and mononitride was also synthesized in a similar fashion and mechanical testing was performed

under the same conditions. Most of the monocarbides were synthesized and tested in another work by the authors [9]. The results of the mononitrides and chromium carbide are shown in Table 2.2. Most of the data for nanoindentation hardness and elastic modulus for transition-metal mononitrides is not otherwise available in the literature for comparison.

Table 2.2: Nanoindentation elastic modulus, hardness, and Poisson’s ratios for every monocarbide and mononitride used as a precursor for the HENs and HECNs. Modulus and hardness are measured from samples synthesized via SPS. Poisson’s ratios are gathered from the literature, and mechanical properties for carbides (except CrC) are from Ref. [9].

Composition	Nanoindentation Modulus (GPa)	Nanoindentation Hardness (GPa)	Poisson’s ratio	References
TiN	532 ± 25	21.1 ± 2.7	0.22	[45,46]
TiC	489	31	0.19	[9,47]
ZrN	441 ± 23	18.6 ± 1.6	0.26	[45,46]
ZrC	402	24	0.20	[9,47]
HfN	377 ± 6	17.8 ± 1.1	0.25	[45,46]
HfC	428	25	0.18	[9,47]
VN	393 ± 44	16.0 ± 3.4	0.29	[48]
VC	465	29	0.22	[9,47]
NbN	389 ± 27	25.5 ± 3.7	0.29	[49]
NbC	429	17	0.22	[9,47]
TaN	377 ± 6	30.6 ± 1.3	0.335	[50]
TaC	431	14	0.24	[9,47]
CrC	292 ± 32	17.8 ± 3.8	0.28	[45,46]
CrN	352 ± 31	17.8 ± 2.5	0.29	[45,46]

Results of average nanoindentation hardness and modulus for the high entropy compositions are shown in Table 2.3; HECN #6 was exempted from mechanical testing due to the two major crystal structures present, which would lead to a multimodal indentation data distribution. Hardness and modulus values for HEN#1 and HECN#1 agree closely with the work of Wen *et al.* [39]. Compared to literature hardness values for high-entropy carbides,^{7,9} HECNs

are within the same hardness range, while HENs have lower hardness. All hardness and modulus values are higher than the expected rule-of-mixtures (ROM) of the monocarbide and mononitride constituents for each composition. Nitrides show an average 17% increase in modulus above ROM values and an average 22% increase in hardness above ROM values. Carbonitrides show an average 31% increase in modulus above ROM values and an average 39% increase in hardness above ROM values. ROM hardness and elastic modulus values do not show any trend with actual experimental values, as shown in Supplementary Figure 2.3. However, important trends in mechanical properties have arisen with configurational entropy and with valence electron concentration.

Table 2.3: Composition, stoichiometry, density, hardness values, and modulus values for each composition. Theoretical density was calculated using lattice parameters from XRD and atomic ratios from EDS and CHNS chemical analysis, except for HECN#6 which was calculated using the weighted average density of the monocarbide/nitride precursors.

Label	Nominal composition	x	Measured Density (g/cm ³)	Theoretical Density (g/cm ³)	Relative density (%)	Nanoindentation Hardness (GPa)	ROM Hardness (GPa)	Nanoindentation Modulus (GPa)	ROM Modulus (GPa)	Measured VEC	Single phase?
HEN #1	(HfNbTaTiZr) ₁ N _x	0.88	10.09	10.18	99.1	27.8	22.5	502.6	422.7	8.7	yes
HEN #2	(CrNbTaTiV) ₁ N _x	0.83	8.33	8.46	98.5	24.4	21.9	476.7	405.0	9.1	yes
HEN #3	(CrHfNbTaTi) ₁ N _x	0.90	9.50	10.39	91.4	26.2	22.6	488.9	410.7	9.1	yes
HEN #4	(CrHfNbTiZr) ₁ N _x	0.91	8.15	8.61	94.7	27.3	20.9	488.4	427.4	8.8	yes
HEN #5	(CrHfTaTiZr) ₁ N _x	0.92	9.56	10.16	94.1	26.5	21.7	465.5	423.9	8.9	yes
HECN #1	(HfNbTaTiZr) ₁ (CN) _x	0.91	9.54	9.68	98.5	32	22.4	557.9	431.0	8.3	yes
HECN #2	(CrNbTaTiV) ₁ (CN) _x	0.81	8.16	8.14	100	30	21.9	518.2	415.0	8.6	yes
HECN #3	(CrHfNbTaTi) ₁ (CN) _x	0.91	10.05	10.21	98.4	29.9	22.0	564.5	419.8	8.7	no – some chemical segregation.
HECN #4	(CrHfNbTiZr) ₁ (CN) _x	0.90	8.35	8.43	99.0	30.4	22.5	531.9	429.2	8.4	yes
HECN #5	(CrHfTaTiZr) ₁ (CN) _x	0.89	9.84	9.86	99.8	29.7	22.5	550	425.8	8.3	yes
HECN #6	(CrMoTaVW) ₁ (CN) _x	0.65	9.13	10.11	90.3	-	-	-	-	8.3	no – two phases

2.3.6 Valence Electron Concentration and Hardness

Valence electron concentration (VEC) has been shown to serve as an indicator for mechanical properties in nitrides, carbides, and carbonitrides, as increasing VEC corresponds to increasing metallic bond character and increased number of structural transformations available to the lattice upon deformation [9,40,51]. Here, VEC values are calculated based on the actual measured compositions of each material, and due to vacancies on the anion lattice and chromium loss, this resulted in lower VEC values than expected, by an average of 0.7. In Figure 2.4(a), nanoindentation hardness has a negative dependence on VEC. Increasing VEC increases metallic bond character and anharmonic lattice vibrations. Therefore, under deformation, the atoms can move to another local minimum structure as opposed to cleaving [41]. Thus, an increase in VEC leads to lower hardness and modulus values. This illustrates the importance of bond character and electronic structure for the intrinsic hardness of these ceramic materials. It is important to keep in mind, however, that VEC, as a way to quantify electronic structure, is an oversimplification, which can be illustrated by the fact that mononitrides with equal VEC can have very different hardness, for example the measured hardness of VN and TaN (VEC = 10) are 16.0 and 30.6 GPa, respectively. However, in high-entropy ceramics, the combined VEC values of the compositions do effectively describe the trends in hardness with composition.

2.3.7 Randomness, Configurational Entropy, and Hardening

Bulk high-entropy carbides [7,9] and borides [6] have shown significantly increased hardness and modulus over their expected ROM values, i.e. the averages of their constituents. In this work, all HENs and HECNs also show increased hardness over ROM values, and, additionally, carbonitrides show an almost double percent increase over the nitrides in both

hardness and elastic modulus versus ROM values. To understand why high-entropy materials consistently have higher hardness than their expected values, and further to understand why carbonitrides exhibit higher strengthening than their nitride counterparts, it is necessary to address the compositional randomness in these materials. Wang *et al.* [52] found that in eight-metal high-entropy carbides, randomness increases hardness due to the increase in possible configurations of dislocation cores, which impedes the movement of dislocations, and that Peierls stress increases with the number of elements. This effect is calculated using density functional theory, where the effect of randomness on specific slip systems can be analyzed. In the same vein, we propose a more facile approach to quantifying the effect of compositional randomness, utilizing configurational entropy.

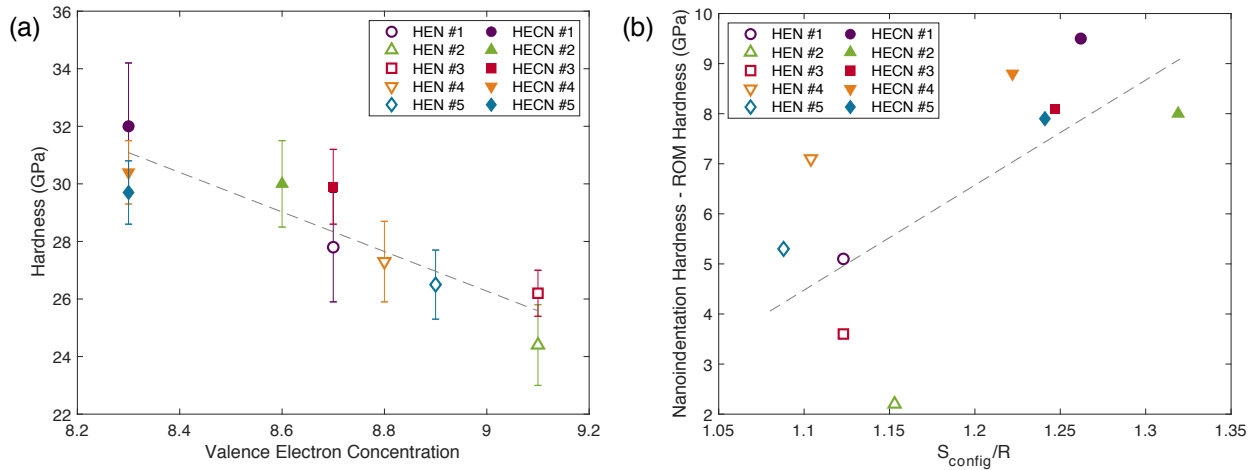


Figure 2.4: (a) Nanoindentation hardness as a function of valence electron concentration (VEC). Error bars are 1 standard deviation from the mean value. (b) Increase in hardness as a function of ideal configurational entropy, where R is the gas constant. Pearson correlation coefficients are equal to -0.90 and 0.75 for (a) and (b) respectively.

There are multiple methods used in the literature to calculate ideal configurational entropy of high-entropy materials, with significant inconsistencies; a detailed comparison of these methods is included in the Supplementary Table 2.3. The crystal structure of high-entropy

nitrides and carbonitrides is comprised of two interpenetrating FCC lattices, the metal cation lattice and the anion lattice, with the metals and anions confined to those specific sites. Thus, the configurational entropy is calculated using the sublattice model, which was first described by Temkin in 1945 [53], expanded upon by Hillert [54,55] and adapted by Miracle and Senkov [56].

$$\Delta S_m^{ideal} = \frac{-R \sum_S \sum_i a^S X_i^S \ln(X_i^S)}{\sum_S a^S}, \quad (Eq. 2.1)$$

In Equation 2.1, a^s is the number of sites on the s sub-lattice, and X_i^s is the fraction of species i randomly distributed on the s sub-lattice, or the “site fraction.” R is the gas constant, and entropic species(i) are defined as an element [57] or a point defect [54]. In this version of the sublattice model, dividing by the total number of atom sites (i.e. the number of atoms in the formula unit) results in the configurational entropy on a per mole of atoms basis, so that it is comparable across crystal structures.

For each sample, the experimentally measured composition and vacancy concentration were used to calculate ideal configurational entropy. In the search for the highest-entropy materials, the actual compositional differences from the ideal composition are often overlooked. However, by measuring variations in composition of high-entropy materials, and therefore variations in configurational entropy, the effects of entropy in high-entropy materials can be elucidated. In Figure 2.4b, the calculated ideal configurational entropy for each sample is plotted against the increase in hardness over the expected value (calculated as the measured nanoindentation hardness minus the ROM hardness). As configurational entropy increases, the increase in hardness increases. This “entropic strengthening” effect is caused by increased compositional randomness, i.e. the different types and sizes of elements inducing local strain in

the lattice which can impede dislocation motion, and it underpins the significant increase in entropy between a five-metal nitride and a five-metal carbonitride.

2.3.8 Entropic strengthening versus solid solution strengthening

Entropic strengthening explains the hardness increases observed as high-entropy ceramic materials become increasingly complex. The baseline hardness of a high-entropy ceramic material is based on its bonding structure, which can be quantified using VEC, and the increase in hardness over the expected value is based on its increased randomness, or configurational entropy. This is similar to the concept of solid solution strengthening, where the strain fields of atoms of different sizes in a solid solution impede dislocation motion. However, simple measures such as atomic size variance or lattice parameter differences, which capture hardening trends for solid solutions, do not apply to HENs and HECNs in this work, nor HECs in the literature [52]. This is likely due to the fact that each metal atom is coordinated to 6 anions, and vice versa, as opposed to each atom position being equivalent in a solid solution. In fact, Ye *et al.* [58] have shown that the anion lattice accommodates most of the strain in the lattice in a DFT study on high-entropy carbides. Thus, the assumption in solid solution strengthening that the strain field around each atom position has an effect on the equivalent atom position next to it (i.e. not accounting for different sublattices), causes simple solid solution strengthening parameters to fail.

Conversely, the geometric model for intrinsic residual strain based on atomic size differences developed by Ye *et al.* [59] does show an interesting correlation with our results. The model was also designed for solid solutions, however, it is based on pairwise geometric comparisons of adjacent atoms, so we adapted the model to only compare the metals with anions

in the structure. A limitation of this model is its inability to describe the more complex crystal structures that exist in high-entropy ceramics, including perovskite oxides [14] and spinels [60]. The root mean squared residual strain calculated with this model correlates extremely well with the calculated configurational entropy values (Pearson correlation coefficient = 0.95, see Supplementary Figure 2.6), supporting the notion that configurational entropy is able to capture the intrinsic strain in the lattice caused by compositional randomness. Additionally, entropy's significance extends further than just size and configuration effects on mechanical properties. Configurational entropy, as a guiding principle of high-entropy materials [61], already has established implications for phase stability [5], high-temperature properties [16], thermal conductivity [62], and more.

2.3.9 Stoichiometry

It is worth noting that HEN #2 and HECN #2 fall below the trend for entropic hardening. This can be traced to the fact that those materials have the highest vacancy concentrations of the compositions tested in nanoindentation. Transition metal carbides and nitrides are typically sub-stoichiometric and are stable in a range of stoichiometry from approximately $0.5 < x < 1.0$, though in some cases nitrides can be super-stoichiometric (i.e. $x > 1.0$) [17]. However, vacancies on the anion lattice outweigh vacancies on the metal lattice when nitrides are synthesized at high temperature [43]. Stoichiometries are listed for each composition in Table 2.3, where x represents the sum of carbon and nitrogen atomic fractions on the anion lattice, calculated by normalizing the metal atomic fraction to 1. Notably, most of the x values are tightly clustered around 0.90, while $x=0.83$ for HEN #2 and $x=0.81$ for HECN#2. Increasing anion vacancy concentration has been shown to cause lattice relaxation and increase metallic bond character in

VN_x , as there are increased metal-metal orbital interactions in the space left by the vacancy [63,64]. Likewise, in HEN #2 and HECN#2, with drastically higher vacancy concentrations, the material exhibits more metallic character and therefore lower hardness and modulus increases than predicted by the configurational entropy. Across all of the compositions there exists no clear trend in mechanical properties with stoichiometry, as shown in Supplementary Figure 2.4. Moreover, the effect of vacancies and resulting increase in metallic bond character demonstrates the need to recognize both VEC/bonding effects and entropic strengthening.

2.4 Discussion

Eleven bulk HENs and HECNs were synthesized for the first time in this study, including 5 single-phase HENs and 4 single-phase HECNs. A single phase high-entropy ceramic is defined based on two essential criteria: a single crystal structure and the homogenous distribution of elements throughout the sample. These two criteria are selected to ensure that there is only one matrix phase in the material, in addition to ensuring the highest degree of homogeneity, randomness, and therefore entropy in the materials. An additional condition to maximize entropy is that the elements on each sublattice should be in equal proportion. The high-entropy nitrides and carbonitrides in this study were all found to have one single FCC rock salt (space group $Fm\bar{3}m$) matrix phase in XRD, except for HECN #6, which contained an FCC rock salt phase and a hexagonal phase. HECN #6 also showed chemical segregation into two distinct phases in EDS. All compositions that were comprised of a single crystal structure also demonstrated chemical homogeneity throughout the high-entropy matrix phase, except for HECN #3, which had islands of minor niobium segregation. Therefore, all compositions besides HECN #6 and HECN #3 are determined to be single-phase high-entropy ceramics.

In addition to maximizing entropy by creating random, homogenous single-phase ceramic materials, entropy is maximized when compositions are equiatomic, so this is often a goal in high-entropy material synthesis. However, by taking into account the experimental variation in composition and vacancy concentrations that occurred during synthesis of multiple HENs and HECNs, it is possible to observe differences in properties due to compositional randomness. To do so, a consistent method for calculating ideal configurational entropy was discussed, which is necessary and long-overdue, due to the foundational nature of configurational entropy to the field of high-entropy materials. Configurational entropy has been used to classify high-entropy alloys and has implications for the mechanical properties and phase stability of these materials. Competing phase formation during synthesis of high-entropy materials with many components is inevitable, and as high-entropy systems increase in ubiquity and complexity, universal adoption of the sublattice model (per mole of atom basis) will bolster our ability to understand and design entropy-related properties.

Hardness enhancements over the rule of mixtures values are almost double the percent increase for HECNs over HENs. This is attributed to the significant increase in configurational entropy attained by going from a one-anion system (nitride) to a two-anion system (carbonitride). Higher configurational entropy represents local inhomogeneity in lattice structure, which impedes dislocation motion and complicates the available slip systems, thus increasing hardness, and similarly creates local strain in bonds, thus increasing modulus. This local inhomogeneity is a direct result of increased atomic mixing, and therefore is represented by the ideal configurational entropy of the sample, which positively correlates with hardness and modulus – the entropic strengthening effect.

In addition to configurational effects, it is necessary to consider the elemental composition, which dictates the bond character of the materials. Increasing metallic bond character, which is associated with increasing anion vacancy concentration and increasing VEC, is found to have a negative effect on hardness and elastic modulus. The finding of a negative correlation of both hardness and modulus with VEC in bulk HENs and HECNs fits well with both existing computational [40,41,51,65,66] and experimental [7,9] results, which demonstrate that bonding and electronic structure govern the inherent mechanical properties in bulk rock-salt structured high-entropy carbides and nitrides. Purposeful design of high-entropy ceramic compositions' configurational entropy and VEC provides the ability to tune mechanical properties and high temperature phase stability in cubic high-entropy ceramics.

Acknowledgements

The authors acknowledge support through the Office of Naval Research ONR-MURI (grant No. N00014-15-1-2863). The authors would like to acknowledge Kevin Kaufmann, Andrew Zhao, William Mellor, Joshua Gild, and Mojtaba Samiee for helpful discussions; Eduardo Marin and Mahika Lunger for laboratory assistance. This work was partially supported through access and utilization of the UC San Diego, Dept. of NanoEngineering's Materials Research Center.

Chapter 2, in full, is a reprint of the material "Bulk high-entropy nitrides and carbonitrides" as it appears in *Scientific Reports* 2020. Dippo, Olivia F.; Mesgarzadeh, Neda; Harrington, Tyler J.; Schrader, Grant D.; Vecchio, Kenneth S. The dissertation author was the primary investigator and author of this material.

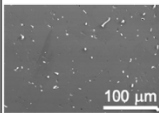
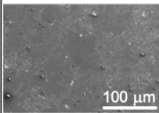
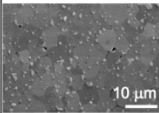
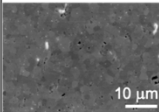
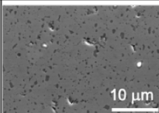
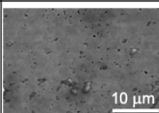
Supplementary Information

Supplementary Table 2.1: Phases present in precursor powders used in the synthesis of high-entropy nitrides and carbonitrides, from XRD.

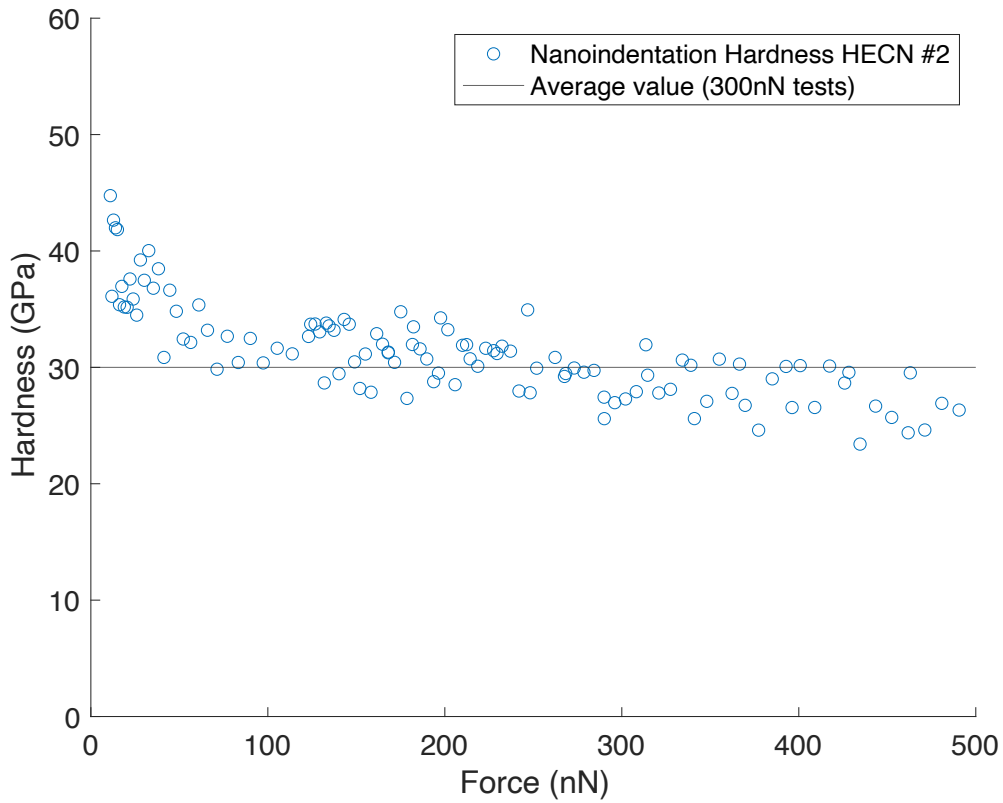
Precursor	Major Compounds		Minor Compounds (<10%)	
	Stoichiometry	Space group	Stoichiometry	Space group
CrN	Cr ₂ N	P -3 1 m	CrN	F m -3 m
			Cr ₂ O ₃	R -3 c H
CrC	Cr ₇ C ₃	P n m a		
	Cr ₃ C ₂	P n m a		
	Cr ₂₃ C ₆	F m -3 m		
HfN	Hf	P 63/m m c		
	HfN	F m -3 m		
HfC	HfC	F m -3 m		
MoC	Mo ₂ C	P b c n		
NbN	NbN	F m -3 m	NbN	P 63/m m c
			Nb ₄ N ₅	I 4/m m m
			Nb ₂ O ₅	P 1 2/m 1
NbC	Nb ₆ C ₅	C 1 2/m 1		
	NbC	F m -3 m		
TaN	TaN	P -6		
TaC	TaC	F m -3 m		
TiN	TiN	F m -3 m		
TiC	TiC	F m -3 m		
VN	VN	F m -3 m	VO ₂	C 1 2/m 1
VC	V ₆ C ₅	P 3 1		
	VC	F m -3 m		
WC	W ₂ C	P -3 1 m		
	WC	P -6 m 2		
ZrN	ZrN	F m -3 m	ZrO ₂	P 1 21/c 1
ZrC	ZrC	F m -3 m		

Supplementary Table 2.2: Phases present in sintered bulk samples, from XRD (see Figure 2.2 in main text) and EDS (see Figure 2.3 in main text and Supplementary Figure 2.1). All are considered single-phase matrix materials, with most having some second-phase oxides present. HECN #3 is not a single-phase matrix due to the presence of a Nb-rich phase which is not an oxide (from EDS). HECN #6 is not single-phase due to the presence of two major phases, from XRD and EDS.

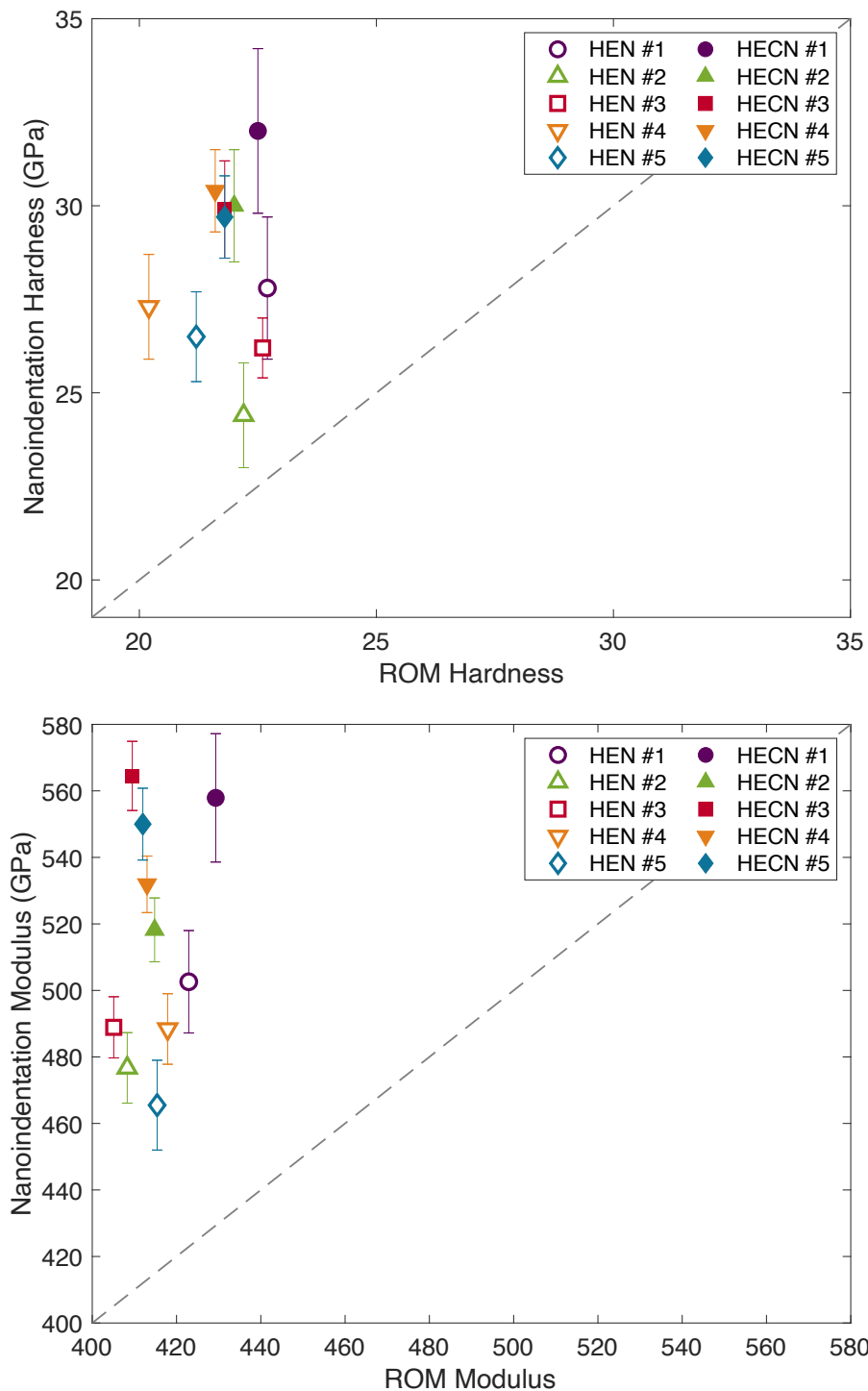
Sample	Composition	Major phase(s)	Secondary phase(s) (<5%)
HEN #1	(HfNbTaTiZr)N	(HfNbTaTiZr)N [FCC]	HfO ₂ -ZrO ₂
HEN #2	(CrNbTaTiV)N	(CrNbTaTiV)N [FCC]	Cr ₂ O ₃
HEN #3	(CrHfNbTaTi)N	(CrHfNbTaTi)N [FCC]	Cr ₂ O ₃ , HfO ₂
HEN #4	(CrHfNbTiZr)N	(CrHfNbTiZr)N [FCC]	HfO ₂ -ZrO ₂ , Cr ₂ O ₃
HEN #5	(CrHfTaTiZr)N	(CrHfTaTiZr)N [FCC]	HfO ₂ -ZrO ₂ , Cr ₂ O ₃
HECN #1	(HfNbTaTiZr)CN	(HfNbTaTiZr)CN [FCC]	HfO ₂ -ZrO ₂
HECN #2	(CrNbTaTiV)CN	(CrNbTaTiV)CN [FCC]	Cr ₂ O ₃
HECN #3	(CrHfNbTaTi)CN	(CrHfNbTaTi)CN [FCC]	Nb-rich carbonitride phase, Cr ₂ O ₃ , HfO ₂
HECN #4	(CrHfNbTiZr)CN	(CrHfNbTiZr)CN [FCC]	HfO ₂ -ZrO ₂
HECN #5	(CrHfTaTiZr)CN	(CrHfTaTiZr)CN [FCC]	HfO ₂ -ZrO ₂ , Cr ₂ O ₃
HECN #6	(CrMoTaVW)CN	Mo ₂ C-W ₂ C-Cr ₂ N [hexagonal], (CrTaV)CN [FCC]	-

Composition	Electron image	EDS Element Maps					
HEN #1		Hf	Nb	Ta	Ta	Zr	O
HECN #1		Hf	Nb	Ta	Ti	Zr	O
HEN #4		Cr	Hf	Nb	Ti	Zr	O
HECN #4		Cr	Hf	Nb	Ti	Zr	O
HEN #5		Cr	Hf	Ta	Ti	Zr	O
HECN #5		Cr	Hf	Ta	Ti	Zr	O

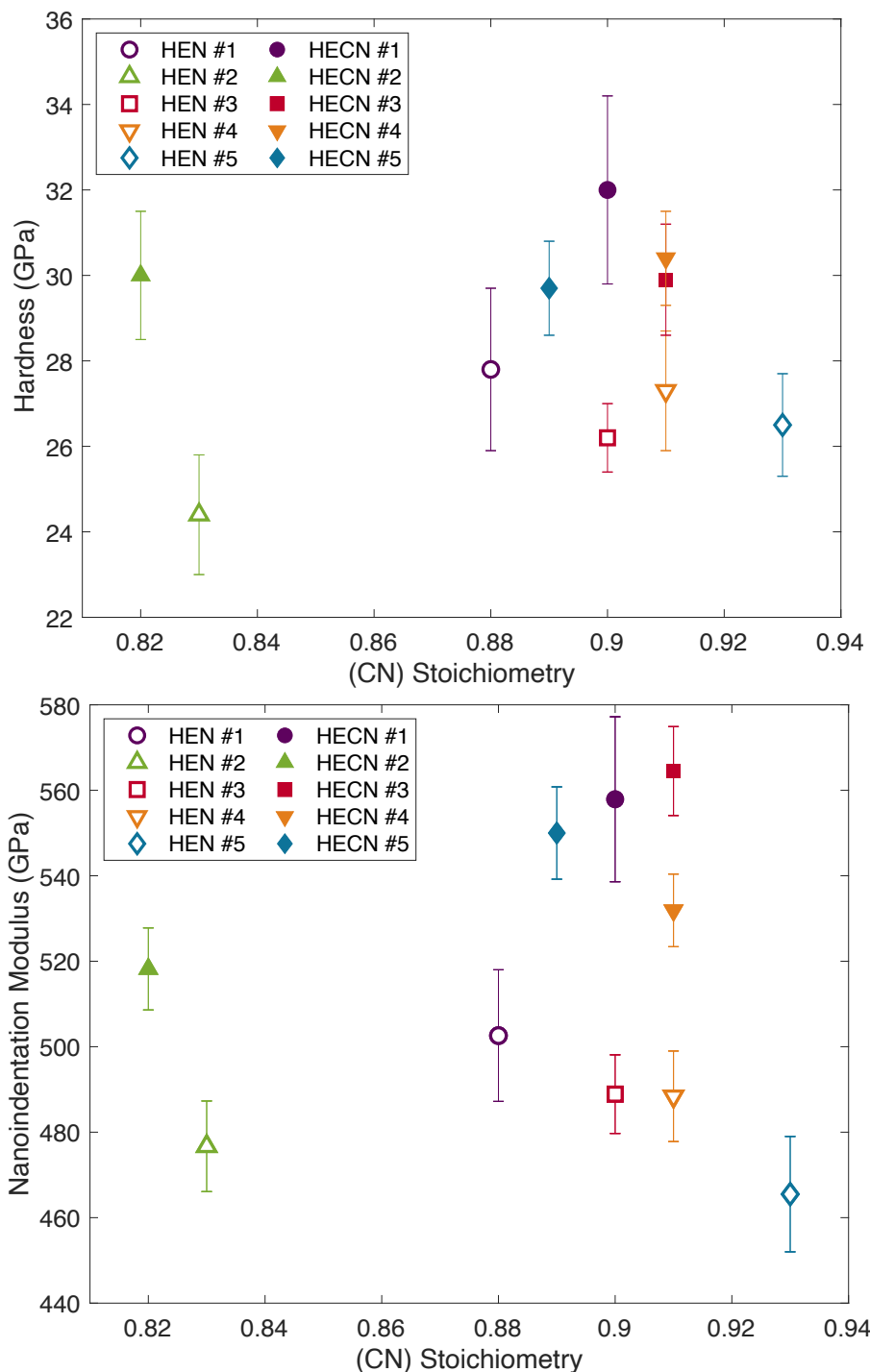
Supplementary Figure 2.1: Microstructure and EDS composition maps for HEN and HECN #1,4,5, which are not included in the main text of the paper. Note the different scale in HEN and HECN #1. All compositions shown here are considered single-phase high-entropy compositions. Inhomogeneities seen in the EDS composition maps are minor second-phase oxides that are native to the precursor powders.



Supplementary Figure 2.2: Nanoindentation hardness as a function of force for composition HECN #2: (CrNbTaTiV)(CN). The minimum force threshold (dotted line) for testing was designated as 100nN. The solid blue line represents an average hardness value of 30.0 GPa from 100 tests at 300 nN. 300nN was determined to be a sufficient load to achieve asymptotic hardness and avoid nanoindentation size effects seen at low loads.



Supplementary Figure 2.3: Nanoindentation hardness (a) and modulus (b) as a function of the expected rule-of-mixtures (ROM) properties of the binary components. $Y=x$ is displayed as a dashed line. All measured nanoindentation hardness and modulus values are higher than the expected ROM values, though no trend is identified. Error bars are 1 standard deviation from the mean value.



Supplementary Figure 2.4: Nanoindentation hardness (a) and modulus (b) as a function of anion stoichiometry (carbon+nitrogen). No trend is identified between anion stoichiometry of the high-entropy compositions and mechanical properties. Error bars are 1 standard deviation from the mean value.

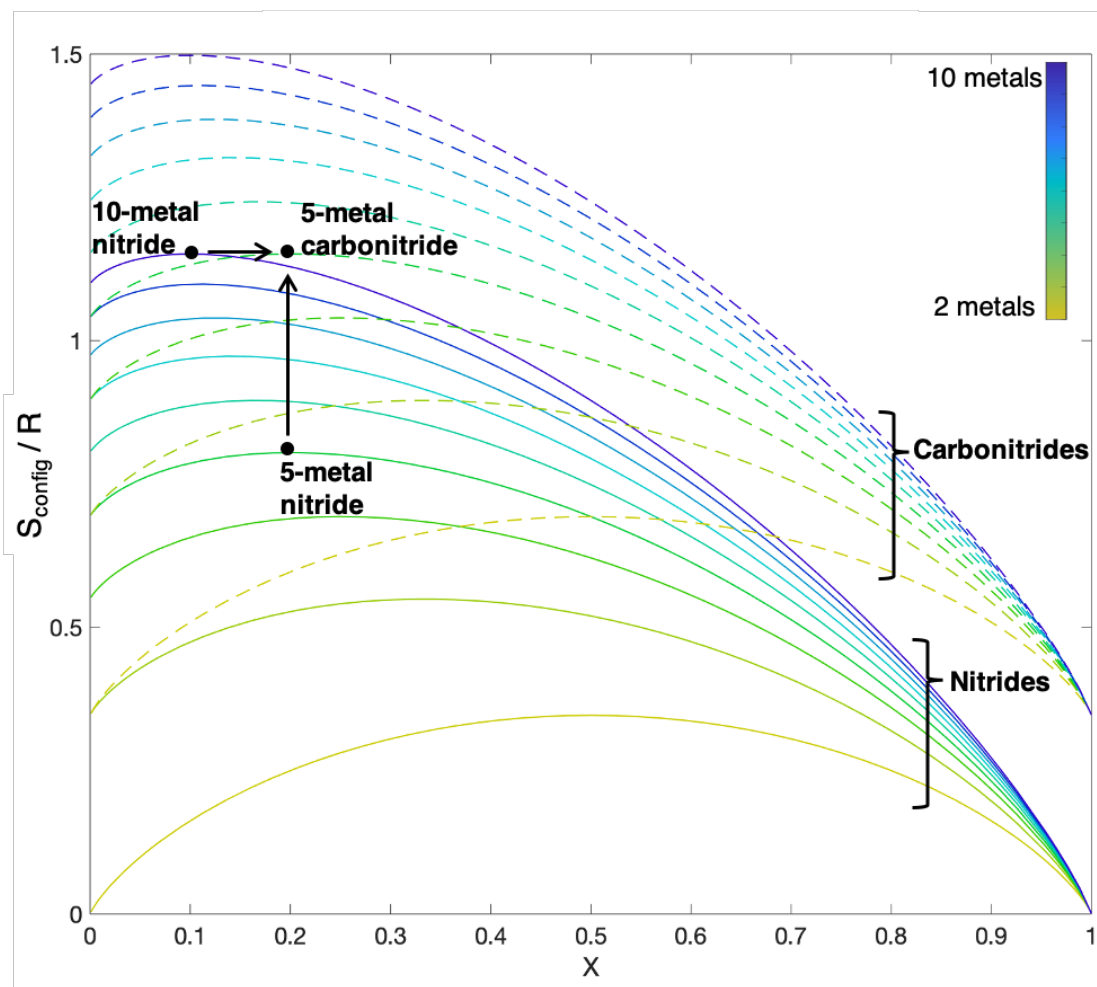
Supplementary Table 2.3: A comparison of different ways of calculating ideal configurational entropy values for different high-entropy materials. Rows 1 and 2 represent high-entropy alloys with 5 metals (5M) and 10 metals (10M). Rows 3 and 4 represent 5-metal carbonitrides with different stoichiometries. Supplementary Equation 2.1 corresponds only to solid solutions (i.e. high-entropy metals with one atom per formula unit).

	Solid solution model (S.Eq 2.1)	Sublattice model, entropy per mole of formula unit (S.Eq 2.2)	Sublattice model, entropy per mole of atom (S.Eq 2.3)
	$S_{SS}^{ideal} = -R \sum_i X_i \ln(X_i)$	$S_{sub,f.u.}^{ideal} = -R \sum_S \sum_i a^S X_i^S \ln(X_i^S)$	$\Delta S_{sub}^{ideal} = \frac{-R \sum_S \sum_i a^S X_i^S \ln(X_i^S)}{\sum_S a^S}$
(5M)	$\ln(5) = 1.61$	$\ln(5) = 1.61$	$\ln(5) = 1.61$
(10M)	$\ln(10) = 2.30$	$\ln(10) = 2.30$	$\ln(10) = 2.30$
(5M)N	$\ln(5) = 1.61$	$\ln(5) = 1.61$	$\ln(5)/2 = 0.80$
(10M)N	$\ln(10) = 2.30$	$\ln(10) = 2.30$	$\ln(10)/2 = 1.15$
(5M)(CN)	$\ln(10) = 2.30$	$\ln(5) + \ln(2) = 2.30$	$[\ln(5) + \ln(2)]/2 = 1.15$
(5M)₂(CN)	$\ln(10) = 2.30$	$2[\ln(5)] + \ln(2) = 3.91$	$[2(\ln(5)) + \ln(2)]/2 = 1.30$

The most commonly used ideal configurational entropy calculation for high-entropy ceramics is Supplementary Equation 2.2. However, an inconsistency arises when comparing configurational entropies between phases of different structures. For example, entropy of the 5-metal 2-anion carbonitride has the same entropy as a 10-metal solid solution. That is, the former material, with 7 elements that are restricted in their possible positions to only one of two sublattices, has equal configurational entropy to the latter material which has 10 species that can occupy any position on the lattice. This is fundamentally incorrect, due to the former having fewer possible configurations than the latter, it will have less configurational entropy.

The root of this problem is that the sublattice model in Supplementary Equation 2.2 is calculating the configurational entropy *per mole of formula unit*, and where there are unequal numbers of atoms per formula unit (for example, 1 in a solid solution metal, and 2 in a carbonitride), there will be a resulting discrepancy in the configurational entropy. By dividing by the total number of atom sites (i.e. the number of atoms in the formula unit), the configurational entropy is calculated on a per mole of atoms basis, so that it is comparable across crystal structures. As systems increase in complexity, different methods for calculating configurational entropy start to diverge.

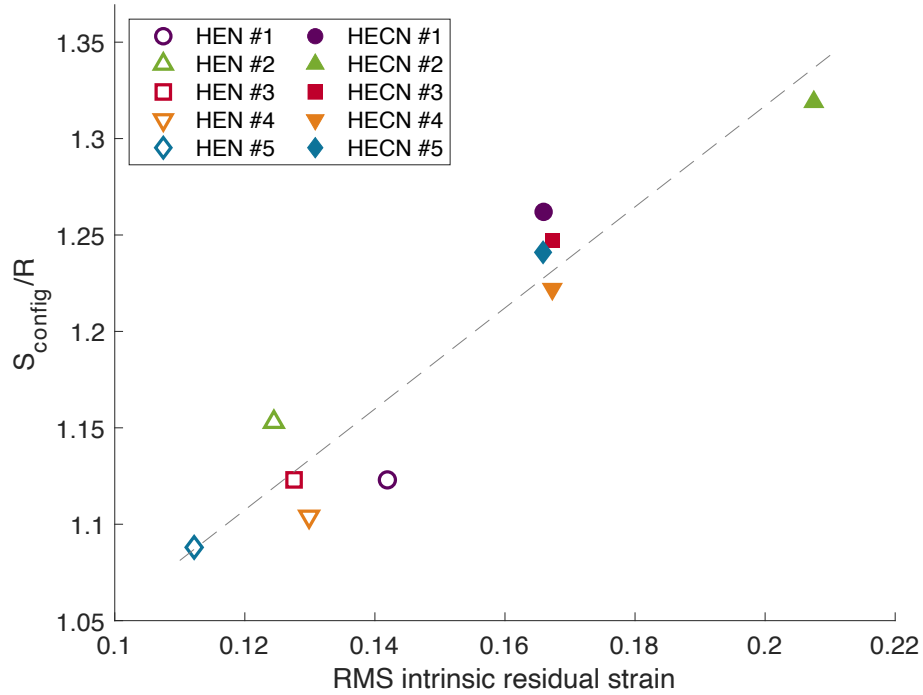
Calculating the configurational entropy using the sublattice model per mole of atom (column 3) is the only method that consistently represents the possible number of configurations in the system. the implications of this model include (1) a 5-metal high-entropy nitride has half the ideal configurational entropy of a 5-metal solid solution high-entropy alloy, which is intuitive due to the addition of the ordered carbon sublattice, i.e. only every other lattice position is a random metal in a carbide as opposed to every lattice position in a metal. (2) Differences in stoichiometry are afforded meaningful differences in entropy, as in (5M)(CN) and (5M)₂(CN). (3) Vacancies and other point defects on each separate lattice can be accounted for as additional species, though this was not specifically shown here. Notably, for this work, the ideal configurational entropy of a 5-metal nitride is 0.8R, and the ideal configurational entropy for a 5-metal carbonitride is 1.15R. A 5-metal 2-anion system has the same ideal configurational entropy value as a 10-metal 1-anion system. That is, by adding one anion to a 5-metal nitride, same entropy gain is achieved as for adding an additional 5 metal species; this is the entropic increase that we exploit by synthesizing carbonitrides, which are 2-anion systems



Supplementary Figure 2.5: The ideal configurational entropy of single anion (i.e. nitride) and two anion (i.e. carbonitride) systems. 10-metal nitrides have equal ideal configurational entropy (S/R) to 5-metal carbonitrides. X corresponds to the site fraction of the metals present in the material, where the maximum entropy corresponds to an equiatomic site fraction.

Supplementary Table 2.4: Pearson correlation coefficients for mechanical properties from nanoindentation vs different metrics used to analyze trends. Entropy is calculated using the sublattice model.

	Entropy	Geometric RMS residual strain	Valence electron concentration
Hardness	0.78	0.79	-0.90
Hardness increase	0.75	0.77	-0.87
Modulus	0.79	0.73	-0.78
Modulus increase	0.83	0.74	-0.65



Supplementary Figure 2.6: RMS geometric intrinsic residual strain vs configurational entropy. Dashed line is a linear fit with Pearson correlation coefficient = 0.95.

References

- [1] C. Oses, C. Toher, S. Curtarolo, High-entropy ceramics, *Nature Reviews Materials*. 5 (2020) 295–309. <https://doi.org/10.1038/s41578-019-0170-8>.
- [2] B.S. Murty, J.W. Yeh, S. Ranganathan, P.P. Bhattacharjee, High-entropy ceramics, in: *High-Entropy Alloys*, 2nd ed., Elsevier, 2019: pp. 165–176. <https://doi.org/10.1016/b978-0-12-816067-1.00009-6>.
- [3] J.-W. Yeh, S.-K. Chen, S.-J. Lin, J.-Y. Gan, T.-S. Chin, T.-T. Shun, C.-H. Tsau, S.-Y. Chang, Nanostructured High-Entropy Alloys with Multiple Principal Elements: Novel Alloy Design Concepts and Outcomes, *Advanced Engineering Materials*. 6 (2004) 299–303. <https://doi.org/10.1002/adem.200300567>.
- [4] B. Cantor, I.T.H. Chang, P. Knight, A.J.B. Vincent, Microstructural development in equiatomic multicomponent alloys, *Materials Science and Engineering A*. 375–377 (2004) 213–218. <https://doi.org/10.1016/j.msea.2003.10.257>.
- [5] C.M. Rost, E. Sachet, T. Borman, A. Moballeggh, E.C. Dickey, D. Hou, J.L. Jones, S. Curtarolo, J.P. Maria, Entropy-stabilized oxides, *Nature Communications*. 6 (2015) 1–8. <https://doi.org/10.1038/ncomms9485>.
- [6] J. Gild, Y. Zhang, T. Harrington, S. Jiang, T. Hu, M.C. Quinn, W.M. Mellor, N. Zhou, K. Vecchio, J. Luo, High-Entropy Metal Diborides: A New Class of High-Entropy Materials and a New Type of Ultrahigh Temperature Ceramics, *Scientific Reports*. 6 (2016). <https://doi.org/10.1038/srep37946>.
- [7] E. Castle, T. Csanádi, S. Grasso, J. Dusza, M. Reece, Processing and Properties of High-Entropy Ultra-High Temperature Carbides, *Scientific Reports*. 8 (2018). <https://doi.org/10.1038/s41598-018-26827-1>.
- [8] X. Yan, L. Constantin, Y. Lu, J. Silvain, M. Nastasi, B. Cui, (Hf_{0.2} Zr_{0.2} Ta_{0.2} Nb_{0.2} Ti_{0.2})C high-entropy ceramics with low thermal conductivity, *Journal of the American Ceramic Society*. 101 (2018) 4486–4491. <https://doi.org/10.1111/jace.15779>.
- [9] T.J. Harrington, J. Gild, P. Sarker, C. Toher, C.M. Rost, O.F. Dippo, C. McElfresh, K. Kaufmann, E. Marin, L. Borowski, P.E. Hopkins, J. Luo, S. Curtarolo, D.W. Brenner, K.S. Vecchio, Phase stability and mechanical properties of novel high entropy transition metal carbides, *Acta Materialia*. 166 (2019) 271–280. <https://doi.org/10.1016/j.actamat.2018.12.054>.
- [10] P. Sarker, T. Harrington, C. Toher, C. Oses, M. Samiee, J.-P. Maria, D.W. Brenner, K.S. Vecchio, S. Curtarolo, High-entropy high-hardness metal carbides discovered by entropy descriptors, *Nature Communications*. 9 (2018) 4980. <https://doi.org/10.1038/s41467-018-07160-7>.
- [11] K. Kaufmann, D. Maryanovsky, W.M. Mellor, C. Zhu, A.S. Rosengarten, T.J. Harrington, C. Oses, C. Toher, S. Curtarolo, K.S. Vecchio, Discovery of high-entropy ceramics via

- machine learning, *Npj Computational Materials*. 6 (2020) 1–9.
<https://doi.org/10.1038/s41524-020-0317-6>.
- [12] J. Gild, J. Braun, K. Kaufmann, E. Marin, T. Harrington, P. Hopkins, K. Vecchio, J. Luo, A high-entropy silicide: (Mo 0.2 Nb 0.2 Ta 0.2 Ti 0.2 W 0.2)Si 2, *Journal of Materiomics*. (2019). <https://doi.org/10.1016/j.jmat.2019.03.002>.
- [13] Y. Qin, J.X. Liu, F. Li, X. Wei, H. Wu, G.J. Zhang, A high entropy silicide by reactive spark plasma sintering, *Journal of Advanced Ceramics*. 8 (2019) 148–152.
<https://doi.org/10.1007/s40145-019-0319-3>.
- [14] S. Jiang, T. Hu, J. Gild, N. Zhou, J. Nie, M. Qin, T. Harrington, K. Vecchio, J. Luo, A new class of high-entropy perovskite oxides, *Scripta Materialia*. 142 (2018) 116–120.
<https://doi.org/10.1016/j.scriptamat.2017.08.040>.
- [15] K. Chen, X. Pei, L. Tang, H. Cheng, Z. Li, C. Li, X. Zhang, L. An, A five-component entropy-stabilized fluorite oxide, *Journal of the European Ceramic Society*. 38 (2018) 4161–4164. <https://doi.org/10.1016/j.jeurceramsoc.2018.04.063>.
- [16] O. Cedillos-Barraza, D. Manara, K. Boboridis, T. Watkins, S. Grasso, D.D. Jayaseelan, R.J.M. Konings, M.J. Reece, W.E. Lee, Investigating the highest melting temperature materials: A laser melting study of the TaC-HfC system, *Scientific Reports*. 6 (2016) 1–11. <https://doi.org/10.1038/srep37962>.
- [17] H.O. Pierson, *Handbook of refractory carbides and nitrides : properties, characteristics, processing, and applications*, Noyes Publications, 1996.
- [18] V.S. Buinevich, A.A. Nepapushev, D.O. Moskovskikh, G. v. Trusov, K. v. Kuskov, S.G. Vadchenko, A.S. Rogachev, A.S. Mukasyan, Fabrication of ultra-high-temperature nonstoichiometric hafnium carbonitride via combustion synthesis and spark plasma sintering, *Ceramics International*. 46 (2020) 16068–16073.
<https://doi.org/10.1016/j.ceramint.2020.03.158>.
- [19] T.E. Steyer, Shaping the Future of Ceramics for Aerospace Applications, *International Journal of Applied Ceramic Technology*. 10 (2013) 389–394.
<https://doi.org/10.1111/ijac.12069>.
- [20] T. Jin, X. Sang, R.R. Unocic, R.T. Kinch, X. Liu, J. Hu, H. Liu, S. Dai, Mechanochemical-Assisted Synthesis of High-Entropy Metal Nitride via a Soft Urea Strategy, *Advanced Materials*. 30 (2018). <https://doi.org/10.1002/adma.201707512>.
- [21] C.H. Lai, S.J. Lin, J.W. Yeh, S.Y. Chang, Preparation and characterization of AlCrTaTiZr multi-element nitride coatings, *Surface and Coatings Technology*. 201 (2006) 3275–3280.
<https://doi.org/10.1016/j.surfcoat.2006.06.048>.
- [22] M.H. Tsai, C.H. Lai, J.W. Yeh, J.Y. Gan, Effects of nitrogen flow ratio on the structure and properties of reactively sputtered (AlMoNbSiTaTiVZr)_x coatings, *Journal of Physics D: Applied Physics*. 41 (2008). <https://doi.org/10.1088/0022-3727/41/23/235402>.

- [23] S.-Y. Chang, M.-K. Chen, D.-S. Chen, Multiprincipal-Element AlCrTaTiZr-Nitride Nanocomposite Film of Extremely High Thermal Stability as Diffusion Barrier for Cu Metallization, *Journal of The Electrochemical Society*. 156 (2009) G37. <https://doi.org/10.1149/1.3097186>.
- [24] P.K. Huang, J.W. Yeh, Effects of nitrogen content on structure and mechanical properties of multi-element (AlCrNbSiTiV)N coating, *Surface and Coatings Technology*. 203 (2009) 1891–1896. <https://doi.org/10.1016/j.surfcoat.2009.01.016>.
- [25] K.H. Cheng, C.H. Lai, S.J. Lin, J.W. Yeh, Structural and mechanical properties of multi-element (AlCrMoTaTiZr)N_x coatings by reactive magnetron sputtering, *Thin Solid Films*. 519 (2011) 3185–3190. <https://doi.org/10.1016/j.tsf.2010.11.034>.
- [26] S.C. Liang, D.C. Tsai, Z.C. Chang, H.S. Sung, Y.C. Lin, Y.J. Yeh, M.J. Deng, F.S. Shieu, Structural and mechanical properties of multi-element (TiVCrZrHf)N coatings by reactive magnetron sputtering, *Applied Surface Science*. 258 (2011) 399–403. <https://doi.org/10.1016/j.apsusc.2011.09.006>.
- [27] H. te Hsueh, W.J. Shen, M.H. Tsai, J.W. Yeh, Effect of nitrogen content and substrate bias on mechanical and corrosion properties of high-entropy films (AlCrSiTiZr) 100-xN_x, *Surface and Coatings Technology*. 206 (2012) 4106–4112. <https://doi.org/10.1016/j.surfcoat.2012.03.096>.
- [28] V. Braic, A. Vladescu, M. Balaceanu, C.R. Luculescu, M. Braic, Nanostructured multi-element (TiZrNbHfTa)N and (TiZrNbHfTa)C hard coatings, *Surface and Coatings Technology*. 211 (2012) 117–121. <https://doi.org/10.1016/j.surfcoat.2011.09.033>.
- [29] M.-H. Hsieh, M.-H. Tsai, W.-J. Shen, J.-W. Yeh, Structure and properties of two Al–Cr–Nb–Si–Ti high-entropy nitride coatings, *Surface and Coatings Technology*. 221 (2013) 118–123. <https://doi.org/10.1016/j.surfcoat.2013.01.036>.
- [30] B. Ren, S.Q. Yan, R.F. Zhao, Z.X. Liu, Structure and properties of (AlCrMoNiTi)N_x and (AlCrMoZrTi)N_x films by reactive RF sputtering, *Surface and Coatings Technology*. 235 (2013) 764–772. <https://doi.org/10.1016/j.surfcoat.2013.08.064>.
- [31] A.D. Pogrebnjak, I. v. Yakushchenko, A.A. Bagdasaryan, O. v. Bondar, R. Krause-Rehberg, G. Abadias, P. Chartier, K. Oyoshi, Y. Takeda, V.M. Beresnev, O. v. Sobol, Microstructure, physical and chemical properties of nanostructured (Ti-Hf-Zr-V-Nb)N coatings under different deposition conditions, *Materials Chemistry and Physics*. 147 (2014) 1079–1091. <https://doi.org/10.1016/j.matchemphys.2014.06.062>.
- [32] D.C. Tsai, Z.C. Chang, B.H. Kuo, T.N. Lin, M.H. Shiao, F.S. Shieu, Interfacial reactions and characterization of (TiVCrZrHf)N thin films during thermal treatment, *Surface and Coatings Technology*. 240 (2014) 160–166. <https://doi.org/10.1016/j.surfcoat.2013.12.034>.

- [33] Z.C. Chang, D.C. Tsai, E.C. Chen, Effect of N₂ flow on the structure and mechanical properties of (CrTaTiVZr)_{N_x} coatings processed by reactive magnetron sputtering, *Journal of Materials Research*. 30 (2015) 924–934. <https://doi.org/10.1557/jmr.2015.79>.
- [34] Q.-W. Xing, S.-Q. Xia, X.-H. Yan, Y. Zhang, Mechanical properties and thermal stability of (NbTiAlSiZr)_{N_x} high-entropy ceramic films at high temperatures, (2019). <https://doi.org/10.1557/jmr.2018.337>.
- [35] C.Y. Wu, R.C. Hsiao, C.H. Hsu, T.H. Hsieh, J.Y. Kao, C.Y. Hsu, Microstructure and mechanical performance of (AlCrNbSiTiV)_N films coated by reactive magnetron sputtering, *Bulletin of Materials Science*. 42 (2019). <https://doi.org/10.1007/s12034-018-1699-7>.
- [36] B. Ren, S.-J. Lv, R.-F. Zhao, Z.-X. Liu, S.-K. Guan, Effect of sputtering parameters on (AlCrMnMoNiZr)_N films, *Surface Engineering*. 30 (2014) 152–158. <https://doi.org/10.1179/1743294413Y.0000000226>.
- [37] S.Y. Lin, S.Y. Chang, Y.C. Huang, F.S. Shieu, J.W. Yeh, Mechanical performance and nanoindenting deformation of (AlCrTaTiZr)_{N_γ} multi-component coatings co-sputtered with bias, *Surface and Coatings Technology*. 206 (2012) 5096–5102. <https://doi.org/10.1016/j.surfcoat.2012.06.035>.
- [38] C.F. Lv, G.F. Zhang, B.S. Cao, Y.Y. He, X.D. Hou, Z.X. Song, Structure and mechanical properties of a-C/(AlCrWTaTiNb)_{C_xN_y} composite films, *Surface Engineering*. 32 (2016) 541–546. <https://doi.org/10.1080/02670844.2015.1130408>.
- [39] T. Wen, B. Ye, M.C. Nguyen, M. Ma, Y. Chu, Thermophysical and mechanical properties of novel high-entropy metal nitride-carbides, *Journal of the American Ceramic Society*. (2020). <https://doi.org/10.1111/jace.17333>.
- [40] K. Balasubramanian, S. v. Khare, D. Gall, Valence electron concentration as an indicator for mechanical properties in rocksalt structure nitrides, carbides and carbonitrides, *Acta Materialia*. 152 (2018) 175–185. <https://doi.org/10.1016/j.actamat.2018.04.033>.
- [41] D.G. Sangiovanni, Inherent toughness and fracture mechanisms of refractory transition-metal nitrides via density-functional molecular dynamics, *Acta Materialia*. 151 (2018) 11–20. <https://doi.org/10.1016/j.actamat.2018.03.038>.
- [42] W.C. Oliver, G.M. Pharr, Measurement of hardness and elastic modulus by instrumented indentation: Advances in understanding and refinements to methodology, *Journal of Materials Research*. 19 (2004) 3–20. <https://doi.org/10.1557/jmr.2004.19.1.3>.
- [43] K. Balasubramanian, S. v. Khare, D. Gall, Energetics of point defects in rocksalt structure transition metal nitrides: thermodynamic reasons for deviations from stoichiometry, *Acta Materialia*. (2018). <https://doi.org/10.1016/J.ACTAMAT.2018.07.074>.

- [44] E.A. Gulbransen, K.F. Andrew, A Preliminary Study of the Oxidation and Vapor Pressure of Chromium, *Journal of the Electrochemical Society*. 99 (1952) 402–406. <https://doi.org/10.1149/1.2779609>.
- [45] A. Jain, S.P. Ong, G. Hautier, W. Chen, W.D. Richards, S. Dacek, S. Cholia, D. Gunter, D. Skinner, G. Ceder, K.A. Persson, The materials project: A materials genome approach to accelerating materials innovation, *APL Materials*. 1 (2013) 011002. <https://doi.org/10.1063/1.4812323>.
- [46] M. de Jong, W. Chen, T. Angsten, A. Jain, R. Notestine, A. Gamst, M. Sluiter, C.K. Ande, S. van der Zwaag, J.J. Plata, C. Toher, S. Curtarolo, G. Ceder, K.A. Persson, M. Asta, Charting the complete elastic properties of inorganic crystalline compounds, *Scientific Data*. 2 (2015) 1–13. <https://doi.org/10.1038/sdata.2015.9>.
- [47] A. Krajewski, L. D'Alessio, G. de Maria, Physico-Chemical and Thermophysical Properties of Cubic Binary Carbides, *Crystal Research and Technology*. 33 (1998) 341–374. [https://doi.org/10.1002/\(SICI\)1521-4079\(1998\)33:3<341::AID-CRAT341>3.0.CO;2-I](https://doi.org/10.1002/(SICI)1521-4079(1998)33:3<341::AID-CRAT341>3.0.CO;2-I).
- [48] A.B. Mei, R.B. Wilson, D. Li, D.G. Cahill, A. Rockett, J. Birch, L. Hultman, J.E. Greene, I. Petrov, J. Birch, L. Hultman, J.E. Greene, I. Petrov, Elastic constants, Poisson ratios, and the elastic anisotropy of VN(001), (011), and (111) epitaxial layers grown by reactive magnetron sputter deposition, *Citation: Journal of Applied Physics*. 21 (2014) 214908. <https://doi.org/10.1063/1.4881817>.
- [49] J. Tan, S. Zhang, S. Wang, W. Wang, X. Zheng, J. Zhao, W. Li, X. Mao, K. Liu, X. Zhou, Y. Zhao, C. Jin, X. Yu, Stoichiometric δ -NbN: The Most Incompressible Cubic Transition Metal Mononitride, *Physica Status Solidi (b)*. 254 (2017) 1700063. <https://doi.org/10.1002/pssb.201700063>.
- [50] J. Chang, G.P. Zhao, X.L. Zhou, K. Liu, L.Y. Lu, Structure and mechanical properties of tantalum mononitride under high pressure: A first-principles study, *Journal of Applied Physics*. 112 (2012). <https://doi.org/10.1063/1.4759279>.
- [51] S.H. Jhi, J. Ihm, S.G. Loule, M.L. Cohen, Electronic mechanism of hardness enhancement in transition-metal carbonitrides, *Nature*. 399 (1999) 132–134. <https://doi.org/10.1038/20148>.
- [52] Y. Wang, T. Csanádi, H. Zhang, J. Dusza, M.J. Reece, R.Z. Zhang, Enhanced Hardness in High-Entropy Carbides through Atomic Randomness, *Advanced Theory and Simulations*. 2000111 (2020) 1–8. <https://doi.org/10.1002/adts.202000111>.
- [53] M. Temkin, Mixtures of Fused Salts as Ionic Solutions, *Acta Physicochimica USSR*. (1945) 411–420.
- [54] M. Hillert, Modelling of disorder, in: *Phase Equilibria, Phase Diagrams and Phase Transformations: Their Thermodynamic Basis*, 2nd ed., Cambridge University Press, 2007: pp. 420–440.

- [55] M. Hillert, L.-I. Staffanson, The Regular Solution Model for Stoichiometric Phases and Ionic Melts, *Acta Chemica Scandinavica*. 24 (1970) 3618–3626.
- [56] D.B. Miracle, O.N. Senkov, A critical review of high entropy alloys and related concepts, *Acta Materialia*. 122 (2017) 448–511. <https://doi.org/10.1016/j.actamat.2016.08.081>.
- [57] D.R. Gaskell, *Introduction to the Thermodynamics of Materials*, 5th ed., Taylor & Francis, New York, NY, 2008.
- [58] B. Ye, T. Wen, K. Huang, C. Wang, Y. Chu, First-principles study, fabrication, and characterization of (Hf_{0.2} Zr_{0.2}Ta_{0.2} Nb_{0.2} Ti_{0.2})C high-entropy ceramic, *Journal of the American Ceramic Society*. 102 (2019) 4344–4352. <https://doi.org/10.1111/jace.16295>.
- [59] Y.F. Ye, C.T. Liu, Y. Yang, A geometric model for intrinsic residual strain and phase stability in high entropy alloys, *Acta Materialia*. 94 (2015) 152–161. <https://doi.org/10.1016/j.actamat.2015.04.051>.
- [60] T. Parida, A. Karati, K. Guruvidyathri, B.S. Murty, G. Markandeyulu, Novel rare-earth and transition metal-based entropy stabilized oxides with spinel structure, *Scripta Materialia*. 178 (2020) 513–517. <https://doi.org/10.1016/j.scriptamat.2019.12.027>.
- [61] B.S. Murty, J.W. Yeh, S. Ranganathan, *High Entropy Alloys*, Elsevier, 2014. <https://doi.org/10.1016/C2013-0-14235-3>.
- [62] J.L. Braun, C.M. Rost, M. Lim, A. Giri, D.H. Olson, G.N. Kotsonis, G. Stan, D.W. Brenner, J.-P. Maria, P.E. Hopkins, Charge-Induced Disorder Controls the Thermal Conductivity of Entropy-Stabilized Oxides, *Advanced Materials*. 30 (2018) 1805004. <https://doi.org/10.1002/adma.201805004>.
- [63] L. Skala, P. Capkovich, Nitrogen vacancy and chemical bonding in substoichiometric vanadium nitride, 1990.
- [64] A.B. Mei, H. Kindlund, E. Broitman, L. Hultman, I. Petrov, J.E. Greene, D.G. Sangiovanni, Adaptive hard and tough mechanical response in single-crystal B1 VN_x ceramics via control of anion vacancies, *Acta Materialia*. 192 (2020) 78–88. <https://doi.org/10.1016/j.actamat.2020.03.037>.
- [65] D.G. Sangiovanni, F. Tasnádi, L.J.S. Johnson, M. Odén, I.A. Abrikosov, Strength, transformation toughening, and fracture dynamics of rocksalt-structure T₁1-x A₁x N (0 ≤ x ≤ 0.75) alloys, *Physical Review Materials*. 4 (2020) 1–12. <https://doi.org/10.1103/PhysRevMaterials.4.033605>.
- [66] D.G. Sangiovanni, V. Chirita, L. Hultman, Electronic mechanism for toughness enhancement in T_xM_{1-x}N (M=Mo and W), *Physical Review B*. 81 (2010). <https://journals.aps.org/prb/pdf/10.1103/PhysRevB.81.104107> (accessed May 6, 2018).

Chapter 3: Color and pseudogap tunability in multicomponent carbonitrides

Olivia F. Dippo¹, Davide G. Sangiovanni², Emma Wenger³, Kenneth S. Vecchio^{1,3*}

Affiliations:

¹ Materials Science and Engineering Program, UC San Diego, La Jolla CA 92093, USA.

²Department of Physics, Chemistry, and Biology (IFM) Linköping University, SE-581 83, Linköping, Sweden

³ Department of NanoEngineering, UC San Diego, La Jolla CA 92093, USA.

*Corresponding author: kvecchio@eng.ucsd.edu, 9500 Gilman Dr, La Jolla, CA 92093, USA.

Abstract

The design and tailoring of material color for both aesthetic and functionality is an ongoing topic of materials science and engineering research. In this work, optical properties of bulk multicomponent transition metal carbonitrides were characterized using reflectivity spectra. Optical pseudogap energies were extrapolated from reflectivity data, and color appearance was quantified in the Commission Internationale de l'Eclairage (CIE) Lightness*Chroma*hue (L*C*h) color space. Variations of color parameters chroma and hue were analyzed in terms of pseudogap energies and electronic band structures. A method for the prediction of pseudogap energy, chroma, and hue of any compositional variation of B1-rocksalt structured Group 4 and 5 transition metal carbonitride is established. Compositional variations were utilized to predictably tune aspects of the electronic structure, including the specificity of electronic transitions and the energy at which they occur, to tailor the material's color appearance. Additionally, through this

method, hues such as pink and purple can be accessed in carbonitrides, which are unattainable in transition metal mononitrides or monocarbides.

3.1 Introduction

Transition metal carbides and nitrides have advantageous combinations of properties, such as good electrical conductivity, high hardness, and high melting temperatures, due to their mixed ionic, covalent and metallic bond character [1,2]. Their high hardness makes these materials particularly suited for use in applications where wear resistance and impact strength are critical. Additionally, certain transition metal nitrides, such as TiN and ZrN, have bright yellow-gold colors [3–5], making them optimal for dual-use decorative and hard-facing coatings. Due to the partially metallic character of transition metal carbides and nitrides, previous understanding of their colored appearances draws significantly from that of metals with similar optical properties. In most metals, the frequency of incident and reflected light is the same, resulting in approximately equal reflectivity over the visible range and an achromatic gray appearance [6]. However, selective absorption of light corresponding to certain electronic transitions will give a metallic material a colored appearance, which is what gives gold and copper their yellow and orange appearances, respectively. These electronic transitions are facilitated by a pseudogap in their electronic structure. The states above the pseudogap must be empty, excited states, and the states below the pseudogap must be occupied, allowing electronic transitions across the gap [6]. Transition metal carbides and nitrides fit these criteria, with a valence band filled by the hybridized anion-*p*/metal-*d* electrons, the bottom of the conduction band composed of vacant anti-bonding *p-d* states, and the valence and conduction band separated by a pseudogap [7–9].

Compositional modifications have been reported to facilitate shifts in electronic structure and pseudogap energy, leading to shifts in color appearance. In metallic systems, for example, in Au-Ag alloys, the addition of silver widens the energy gap, pushing the reflectivity edge to higher energies, and causing the gold color to turn greenish [10]. Alloying Cu with Zn or Ga increases its electron transition energy, shifting its color from orange to yellow [11]. Similarly, a red shift has been reported in TiN thin films due to an increase in non-nitrogen anion content (carbon or oxygen) [12]. Transition metal nitrides range in color appearance from bright yellow to gray. The brightest colors, in TiN and ZrN, are a consequence of narrow p-bands, higher concentrations of free carrier electrons, and dominance of high-energy p-d interband electronic transitions. Transition metal carbides generally have a gray-colored appearance with little selectivity in electronic transitions due to a lower concentration of free carrier electrons and a Fermi level that aligns with the pseudogap, allowing lower-energy intraband electronic transitions to dominate [4].

In recent years, multicomponent and high-entropy carbides and nitrides have received attention for their ability to leverage compositional modification to create tunable properties, or even enhancement of certain properties, such as phase stability and mechanical properties [13–15]. Optical and electronic properties of multicomponent ceramics are also gaining attention: a high-entropy fluoride was synthesized to be transparent and photoluminescent [16]; a high-entropy nitride was tuned for increased absorption of solar wavelengths (AlCrTaTiZr)N [17]; and high-entropy oxides have been reported with a tailored band gap width [18] and crystal distortions [19]. Bulk high-entropy nitrides and carbonitrides and their tunable mechanical properties were first reported by Dippo *et al.* [20]. In this work, the optical properties of the materials from Ref. [20], as well as of a range of novel multicomponent carbonitrides will be

discussed. Herein, the tunability potential and the limits of optical property shifts are explored in rocksalt-structured B1 transition metal carbides and nitrides, through analysis of the optical-electronic properties of multicomponent carbonitrides. By mixing bright yellow nitrides with gray carbides, electronic transition energies are modified, and new colors are tailored, designed, and created. A method to predict pseudogap energies and colored appearances of carbonitrides is established, demonstrating the ability to tune the colored appearances of multicomponent carbonitrides.

3.2 Methods

3.2.1 Synthesis

Precursor powders of graphite, CrN, CrC, HfC, NbN, NbC, TaN TaC, TiN, TiC, VC, ZrN, and ZrC were procured from Alfa Aesar (> 99% purity); HfN was procured from Reade Advanced Materials (99.5% purity); VN was procured from American Elements (99% purity). The synthesis of mononitrides is detailed in a previous work by the authors [20]. Monocarbides synthesized for this work are produced using the same processing parameters: sintering at 300°C below their melting temperature, with a maximum sintering temperature of 2200°C. The synthesis of the high entropy nitrides (HENs #1-5) and high entropy carbonitrides (HECNs #1-5) are also detailed in our previous work [20]. The synthesis of *new* multicomponent carbonitride materials were also produced following similar procedures using spark plasma sintering (SPS, Thermal Technologies, CA, USA), as 10 mm diameter pucks, 3-4 mm thick. A heating rate of 100°C per minute was utilized, up to a maximum temperature of 2200°C and a maximum pressure of 50 MPa, with a 10-minute hold time at the maximum temperature and pressure. The sintering chamber was kept under vacuum with a maximum pressure of 30 mTorr below 1200°C;

above 1200°C, argon was flowed into the chamber. The outside edges of the sample containing excess carbon from sintering in graphite dies were ground off, and a sample face was ground with diamond grinding platens and polished to a mirror finish with a 1 µm diamond suspension before further analysis. Table 3.1 shows a listing of all the nitrides and carbonitrides included in this present study.

Table 3.1: Listing of the nitrides and carbonitrides in the present study.

Precursor mononitrides & monocarbides	HENs & HECNs (Ref. [20])	Multicomponent carbonitrides
TiN	(HfNbTaTiZr)N	(Cr _{0.2} Hf _{0.4} Zr _{0.4})(C _{0.7} N _{0.3})
ZrN	(CrNbTaTiV)N	(Ti _{0.2} Zr _{0.4} Hf _{0.4})(C _{0.7} N _{0.3})
HfN	(CrHfNbTaTi)N	(Cr _{0.2} Hf _{0.2} Nb _{0.2} Ti _{0.2} Zr _{0.2})(C _{0.75} N _{0.25})
VN	(CrHfNbTiZr)N	(Cr _{0.2} Hf _{0.2} Ta _{0.2} Ti _{0.2} Zr _{0.2})(C _{0.75} N _{0.25})
NbN	(CrHfTaTiZr)N	Zr ₁ (C _{0.1} N _{0.9})
TaN	(HfNbTaTiZr)(CN)	(Ti _{0.2} Zr _{0.8})(C _{0.6} N _{0.4})
CrN (contains CrN and Cr ₂ N)	(CrNbTaTiV)(CN)	(Ti _{0.1} Zr _{0.9})(C _{0.6} N _{0.4})
	(CrHfNbTaTi)(CN)	Ti ₁ (C _{0.4} N _{0.6})
TiC	(CrHfNbTiZr)(CN)	(Ti _{0.9} Zr _{0.1})(C _{0.4} N _{0.6})
ZrC	(CrHfTaTiZr)(CN)	(Ti _{0.9} Nb _{0.1})(C _{0.4} N _{0.6})
HfC		(Ti _{0.7} Zr _{0.3})(C _{0.4} N _{0.6})
VC		Ti ₁ (C _{0.3} N _{0.7})
NbC		(Ti _{0.9} Zr _{0.1})(C _{0.3} N _{0.7})
TaC		(Ti _{0.9} Hf _{0.1})(C _{0.3} N _{0.7})
CrC (contains Cr ₃ C ₂ , Cr ₇ C ₃ , and Cr ₂₃ C ₆)		Ti ₁ (C _{0.2} N _{0.8})
		(Ti _{0.9} Hf _{0.1})(C _{0.2} N _{0.8})
		Ti ₁ (C _{0.1} N _{0.9})
		(Ti _{0.84} Hf _{0.04} Nb _{0.04} V _{0.04} Zr _{0.04})(C _{0.2} N _{0.8})
		(Ti _{0.2} Zr _{0.2} Hf _{0.2} V _{0.2} Nb _{0.2} Ta _{0.2})(C _{0.5} N _{0.5})
		(Ti _{0.6} Zr _{0.4})(C _{0.5} N _{0.5})
		(Cr _{0.4} Ti _{0.6})(C _{0.1} N _{0.9})
		(Cr _{0.3} Ti _{0.4} Zr _{0.3})(C _{0.1} N _{0.9})
		(Nb _{0.1} Ti _{0.5} V _{0.3} Zr _{0.1})(C _{0.1} N _{0.9})
		(Nb _{0.8} Ta _{0.1} Zr _{0.1})(C _{0.5} N _{0.5})

3.2.2 UV-Vis-Near IR Spectroscopy

Optical spectroscopy was performed using a Lambda 1050 UV/Vis/NIR spectrophotometer (PerkinElmer, MA, USA) equipped with a 150 mm InGaAs integrating sphere and a 10 mm diameter aperture. Spectra were collected in reflectance mode over a wavelength range of 250 to 1400 nm in 10 nm steps. 100% reflectance baseline spectra were collected using a Spectralon standard.

3.2.3 CIEL *a*b*/CIEL *C*h* Color Measurement

CIEL *a*b*/CIEL *C*h* color determinations were done in accordance with the CIE 1964 guidelines as outlined in ASTM standard E308-18, using a 10-degree observer and D65 illuminant, mimicking color appearance in daylight.

Tristimulus values are defined as:

$$X_{10} = \sum_{380}^{780} W_X(\lambda)R(\lambda), \quad (\text{Eq. 3.1})$$

$$Y_{10} = \sum_{380}^{780} W_Y(\lambda)R(\lambda), \text{ and} \quad (\text{Eq. 3.2})$$

$$Z_{10} = \sum_{380}^{780} W_Z(\lambda)R(\lambda). \quad (\text{Eq. 3.3})$$

where $R(\lambda)$ is the reflectance, and tristimulus weighting factors W_X , W_Y , and W_Z are as tabulated in the standard for a D65 illuminant, 10nm interval, and 10-degree observer (1964 standard).

Color parameters $L^*a^*b^*$ and $L^*C^*h^*$ are defined below. L^* is the lightness, where 0 is black and 100 is white. Rectangular coordinates to describe color are given by a^* , representing red/green levels, and b^* , representing blue/yellow levels. Polar coordinates to describe color, used throughout this work, are given by the chroma (C^*), representing color saturation, and hue (h^*) represents the angle on the color wheel.

$$L^* = 116 f(Q_Y) - 16, \quad (\text{Eq. 3.4})$$

$$a^* = 500 [f(Q_X) - f(Q_Y)], \quad (\text{Eq. 3.5})$$

$$b^* = 200 [f(Q_Y) - f(Q_Z)], \quad (\text{Eq. 3.6})$$

$$C^* = [(a^*)^2 + (b^*)^2]^{1/2}, \text{ and} \quad (\text{Eq. 3.7})$$

$$h^* = 180 - (180/\pi)\tan^{-1}(a^*/b^*) - 90\text{sign}(b^*). \quad (\text{Eq. 3.8})$$

where:

$$Q_X = X_{10}/X_N, \quad (\text{Eq. 3.9})$$

$$Q_Y = Y_{10}/Y_N, \quad (\text{Eq. 3.10})$$

$$Q_Z = Z_{10}/Z_N, \quad (\text{Eq. 3.11})$$

and

$$\begin{aligned} f(Q_i) &= Q_i^{1/3} \text{ if } Q_i > (6/29)^3 \quad \text{or} \\ f(Q_i) &= (841/108)Q_i \text{ if } Q_i \leq (6/29)^3. \end{aligned} \quad (\text{Eq. 3.12})$$

where i varies as X, Y, and Z. X_N , Y_N , and Z_N define the white point; for a D65 illuminant and 10-degree observer, $X_N = 94.811$, $Y_N = 100.000$, and $Z_N = 107.304$.

3.2.4 Tauc Plots

To determine the optical pseudogap energies (E_{pg}) of the materials, an extrapolation method commonly referred to as the ‘Tauc method’ is used [21]. Tauc plots rely on absorbance data, so a Kubelka-Munk transform is first employed to convert the reflectance data (R), based on the assumption of an infinitely thick, or opaque material [22,23], as:

$$R_\infty = \frac{R_{\text{sample}}}{R_{\text{standard}}}, \quad (\text{Eq. 3.13})$$

where R_{sample} is the reflectance spectrum of the sample and R_{standard} is the Spectralon standard. R_{∞} is the reflectance of the sample with infinite thickness, corresponding to $> 2\text{mm}$ in practice; samples tested in this work were all $> 2\text{mm}$ in thickness. $F(R_{\infty})$ is the remission function, which is given by:

$$F(R_{\infty}) = \frac{(1-R_{\infty})^2}{2R_{\infty}}, \quad (\text{Eq. 3.14})$$

where $F(R)$ is proportional to the absorption coefficient.

$$F(R_{\infty}) = A (h\nu - E_g)^{1/2}, \quad (\text{Eq. 3.15})$$

where A is a proportionality constant. From this relation, $[F(R_{\infty})h\nu]^2$ vs $h\nu$ is plotted; a line is fit to the linear portion of the plot and extrapolated to the x-axis, corresponding to the optical absorption edge. The value where this line crosses the x-axis is the optical gap energy, E_g , corresponding to a direct allowed electronic transition. An example Tauc plot for $\text{Zr}(\text{C}_{0.1}\text{N}_{0.9})$ is shown in Figure 3.2a.

3.2.5 Rule of Mixtures Color Calculations

Rule of mixtures (ROM) color predictions were performed using a MATLAB program, by testing all possible combinations of 6 transition metals and 2 anions in 10 atomic percent composition steps. The transition metals constituted Ti, Zr, Hf, V, Nb, and Ta. An ROM spectrum was created for each combination by taking a weighted average of the spectra of the precursors. CIE $L^*C^*h^*$ calculations were applied to the ROM spectra.

3.2.6 Density of States Calculations

Density-functional theory calculations of electronic densities of states (DOS) of stoichiometric and anion-deficient B1-structured nitrides, carbides, and carbonitrides are carried out using VASP [24] implemented with the projector augmented wave method [25]. Electronic exchange and correlation effects are evaluated via the generalized gradient approximation of Perdew, Burke, and Ernzerhof [26]. Our simulation supercells are comprised of 192 B1 lattice sites (96 cation and 96 anion positions). Metal species and anion-vacancies are randomly arranged on the corresponding sublattices. The supercells are constructed with x, y, and z Cartesian axes aligned to [110], [112], and [111] crystallographic directions. Incommensurate structural parameters along x, y, and z allow minimizing the degree of correlation between atomic positions, which mimics configurationally-disordered alloys. Prior to performing DOS calculations, the supercell structural parameters and atomic positions are optimized via conjugate gradient energy minimization. This is done with accuracies of 10–5 eV/supercell, with forces on atoms smaller than 0.01 eV/Å. Both energy-minimization and DOS calculations employ Brillouin-zone integration on $4 \times 4 \times 4$ Monkhorst-Pack k-point meshes and 500 eV cutoff energies for the planewave basis set.

For the sake of simplicity of hue and chroma descriptors proposed in this work and consistency throughout our calculations, all present DFT evaluations of DOS of stoichiometric binary nitrides and carbides employ ideal B1 lattice positions and neglect electronic-spin degrees of freedom. This approach provides accurate DOS for non-magnetic nitrides and carbides which crystallize in the B1 structure at 0 kelvin. Conversely, some differences between calculated and actual DOS (hence also between predicted vs actual hue and chroma values) may be expected for stoichiometric Group-5 nitrides (namely, VN, NbN, and TaN), CrC, CrN, as well as for alloys

that contain relatively high Cr contents or have valence electron concentrations (VEC) near $10 e^-$ /formula-unit. Indeed, Group-5 nitrides are dynamically-stabilized in the B1 structure at finite temperatures thanks to strong anharmonicity [27,28]. The effect stems, in turn, from a high VEC ($=10 e^-$ /f.u.), which produces soft vibrational modes [29]. Regarding non-magnetic B1 CrC and B1 CrN: both are predicted to be mechanically stable at 0 kelvin (see supplemental material in Ref. [30]). To our knowledge, however, B1 CrC has not been reported experimentally. Conversely, stoichiometric CrN has an antiferromagnetic orthorhombic structure in its ground state [31,32], which is thermodynamically stabilized B1 structure by lattice vibrations and paramagnetic spin disorder at room temperature [33,34].

3.3 Results and Discussion

3.3.1 Color

Transition metal mononitrides exhibit colors that range from bright yellow (TiN, ZrN), to pale yellow (HfN, VN, TaN), to gray (NbN, CrN). Transition metal monocarbides are usually gray in color, with a few of examples of pale yellow (HfC, NbC, TaC). The colors were quantified using the CIE L*a*b* color standard, derived from wavelength-dependent reflectance measurements. Full L*a*b* color results for the transition metal mononitrides and transition metal monocarbides utilized as precursors to carbonitrides in this work are listed in Supplementary Table 3.1.

Twenty-four carbonitride samples were synthesized, consisting of multicomponent mixtures of transition metal monocarbides and transition metal mononitrides, with a range of hues including yellow, orange, pink, and purple-gray; Figure 3.1a demonstrates examples of the range of colors accessible. The full list of carbonitride samples with L*a*b* color values can be

found in Supplementary Table 3.2. Selected reflectance results of three carbonitrides are shown in Figure 3.1b, displaying distinct differences in the reflectance profiles and the corresponding color appearance. Reflectance curves with a large delta between maximum and minimum values, with a steep transition or reflectance edge, represent materials whose colors are the brightest. The characteristic bright golden color of TiN and ZrN is determined by the plasma reflection edge [35], and substitutional anion additions of carbon decrease the plasma energy as the C/N ratio increases in carbonitrides [36]. In Fig 1b, this manifests as a shift in the reflectivity minimum toward higher wavelengths with an increase in carbon content. At energies below the reflectivity minimum, intraband transitions dominate, and above, interband transitions dominate [35]. Reflection minimums shift toward higher wavelengths with carbon addition, indicating that the onset of interband C $2p \rightarrow$ metal $3d$ transitions shift to lower energies, while plasma energy decreases [36]. Further analysis of this phenomenon requires analysis of the energy gaps in the carbonitride materials as compositions are tuned.

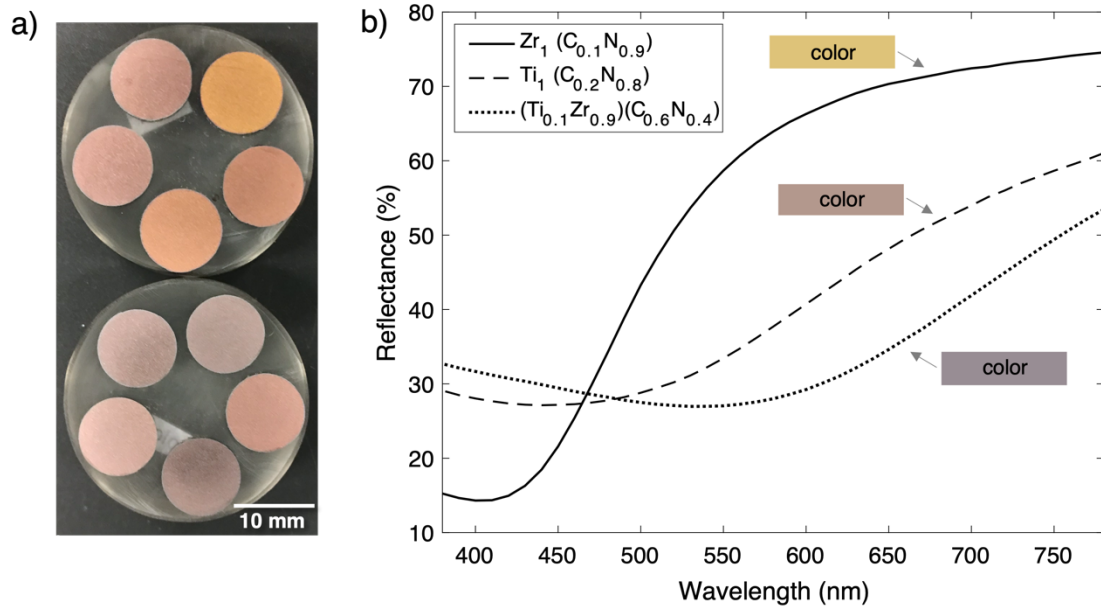


Figure 3.1: (a) Examples of colors of 10 multicomponent carbonitride materials synthesized in this work, displaying the range of colors achievable. (b) Reflectance plots for three carbonitride samples: $Zr(C_{0.1}N_{0.9})$, a high-saturation gold hue (top), and $Ti(C_{0.2}N_{0.8})$, displaying a lower-saturation pink color (middle), and $(Ti_{0.1}Zr_{0.9})(C_{0.6}N_{0.4})$ displaying a gray-purple color.

3.3.2 Optical Pseudogap Analysis

Carbide and nitride materials are known to display pseudogaps, i.e. a deep valley in the electronic density of states between the valence and conduction bands, but they typically have a non-zero density of states at the Fermi level and are therefore electrical conductors [8,37]. Tauc plot analysis (see Figure 3.2a) was used to extrapolate the energy of the electron transition across the pseudogap from the reflectance data. The pseudogap energy (E_{pg}) for a transition metal carbonitride can be predicted using Equation 3.16, where $E_{pg,ROM}$ is the pseudogap energy based on the ROM of the mononitride and monocarbide precursors, and $E_{pg,adj}$ is the adjusted pseudogap energy prediction:

$$E_{pg,adj} = 1.26 * E_{pg,ROM} - 0.92 \text{ [eV]}. \quad (Eq. 3.16)$$

This linear fit equation is shown in Fig. 3.2b, based on the ROM average of the pseudogap energies of its mononitride and monocarbide constituents.

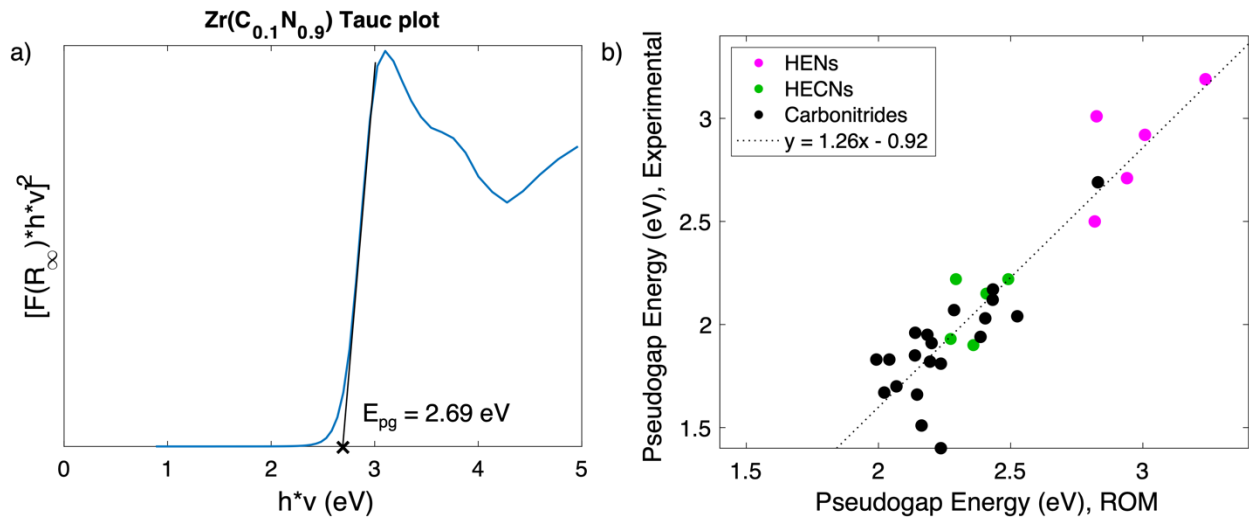


Figure 3.2: (a) Example Tauc plot, illustrating the extrapolation method for the determination of optical pseudogap energy. (b) Pseudogap energy based on a rule of mixtures (ROM) average of the precursor mononitrides and monocarbides vs the measured pseudogap energy extrapolated from Tauc plots. Linear fit line constitutes the prediction method for pseudogap energies.

3.3.3 Hue and Chroma Trends in Carbonitrides

Hues of Group 4, 5, and 6 multicomponent nitrides, carbides, and carbonitrides are shown in Fig. 3.3a, reaching a maximum approximately equal to 90, which corresponds to a yellow hue. As their pseudogap energy decreases, the hues decrease, and they decrease significantly more for the carbonitrides (black dots in Fig. 3.3) than the mononitrides or monocarbides (x's in Fig. 3.3). Thus, by producing a carbonitride material, more hues are accessible, including the range from $-120 < h^* < 0$ (or, equivalently, $240 < h^* < 360$), corresponding to blue, purple, and pink hues. The addition of carbon to nitrides, and in some cases the tuning of metal compositions, leads to a decrease of the pseudogap energy, i.e. a lower energy electronic transition, thus decreasing the hue value of the material and enabling new hue possibilities.

The power-law fit of hue vs pseudogap energy in Fig. 3.3a (Eq. 3.17) is established as a more accurate prediction than the rule of mixtures (ROM) hue predictions. Because the mononitrides and monocarbides are constrained in hue from $h^* = 10$ (TiC) to $h^* = 97$ (ZrN), with the majority falling between $60 < h^* < 90$, ROM hue predictions also tend to lie in the 60 to 90 range, corresponding to orange to yellow hues. As multicomponent solid solution carbonitride materials enable access to red-shifted hues beyond orange and yellow, an adjusted method for hue prediction is necessary. Thus, the hues of these materials are assessed according to their predicted pseudogap energy (Eq. 3.16), and the adjusted hue (h^*_{adj}) vs pseudogap energy ($E_{pg,adj}$) fit (Eq. 3.17)

$$h^*_{adj} = -947.8(E_{pg,adj}) + 98.77. \quad (Eq. 3.17)$$

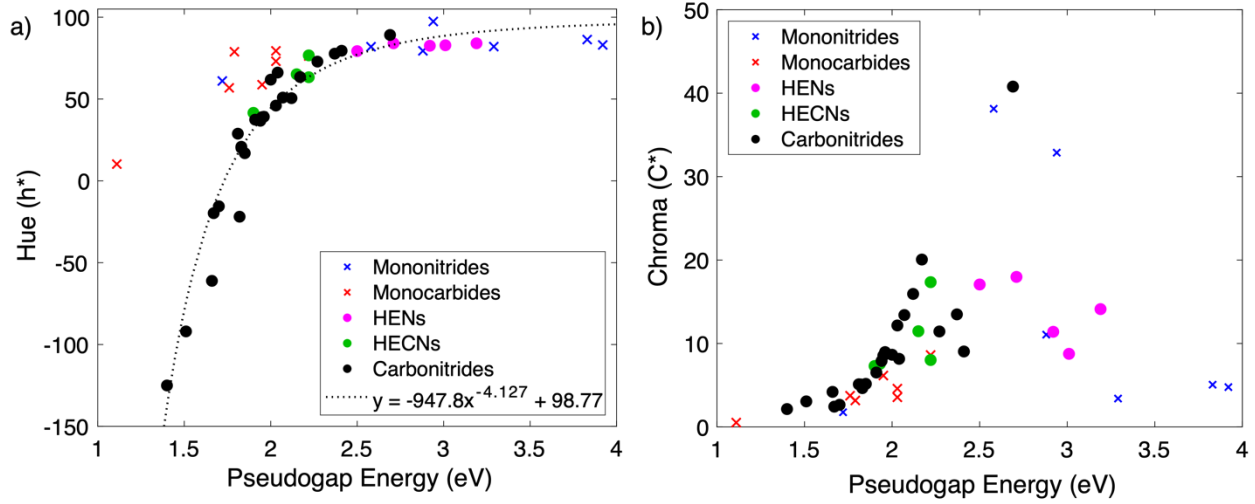


Figure 3.3: Hue and chroma trends with pseudogap energy. (a) Hue vs pseudogap energy, with fit line included for carbonitrides, which can access a larger range of hues than monocarbides and mononitrides. (b) Chroma value vs pseudogap energy. The high-entropy nitrides (HENs) and high-entropy carbonitrides (HECNs) shown were synthesized in Ref. [20].

As colors are red-shifted from the characteristic golden-yellow of mononitrides, such as TiN and ZrN, their chroma (i.e. saturation) decreases. The chroma of the multicomponent carbonitrides reaches a maximum with pseudogap energies between 2.5 and 3 (Fig. 3.3b). However, unlike the hue, chroma is not predictable based on pseudogap energy, as there are examples in the data wherein two carbonitride materials have the same pseudogap energy, but different chromas (see, e.g., two green circles at pseudogap energy ≈ 2.2 eV in Fig. 3.3b). Engineering chroma values is equally important as hue, as a material with very low chroma ($0 < C^* < 3$) will appear to the human eye somewhere on the black/gray/white spectrum, no matter its hue. High chroma values require highly selective absorption energies. Nitride materials TiN and ZrN with highly selective absorption behavior are characterized by a tall, narrow valence band peak, facilitating p-d interband transitions at specific energies [4]. As shown below, chroma values can be predicted based on DOS-peak broadening of the precursor mononitrides and monocarbides.

As carbides and nitrides are mixed in solid solution, the energies of their densities of states also mix, resulting in broadening when peaks are at similar, but slightly different energies. This valence band broadening effect has been reported in TiCN thin films, based on DOS calculations [38] and experimental X-ray photoelectron spectroscopy measurements [36]. Slight broadening of the valence peak due to atomic mixing changes the electron transition energy, enabling the red shift of color from yellow nitrides to orange, pink, and purple carbonitrides. However, broadening also contributes to the dampening of the carbonitride's color saturation, or chroma value (C^*). Additionally, a large distance from the valence peak to the Fermi level supports selective, high-energy interband transitions. Nitrides have a much larger separation between the anion-p/metal-d valence band and Fermi level than carbides. Because the threshold energy for interband transitions in carbides is much lower than nitrides, at < 1 eV, carbides have much lower selectivity in the visible range [39]; for this reason, carbides have a grayer and duller appearance than nitrides.

The electronic density of states (DOS) for all Group 4 and 5 B1-structured mononitrides and monocarbides were calculated. Example DOS are shown in Fig. 3.4a for TiN, TiC, ZrN, ZrC, with their valence peak energies marked (dashed lines); see Supplementary Fig. 3.1-14 for all DOS plots. To quantify the effect of both the separation of the p-d valence peak from the Fermi level and the valence peak broadening, the parameter 'p' was created, where p equals the standard deviation of the valence peak energies of the constituent transition metal monocarbides and transition metal mononitrides divided by the weighted average of the valence peak energies. It was found that when $p > 0.16$, i.e. the standard deviation is high, p has a linear relation to chroma (Fig. 3.4b), and the following chroma adjustment (C_{adj}^*) can be applied:

$$C_{adj}^* = -80.35p + 30.07. \quad (Eq. 3.18)$$

The upper limit for each material’s predicted chroma value is its ROM chroma, and when $p < 0.16$, the predicted chroma is equal to its ROM chroma. Otherwise, when $p > 0.16$, the chroma adjustment (C_{adj}^*) captures the decrease in chroma value relative to the ROM chroma when constituent materials have significant differences in valence peak energies. An independent test case for these fitting parameters, confirming the E_{pg} , hue, and chroma predictability can be found in Supplementary Fig. 3.15.

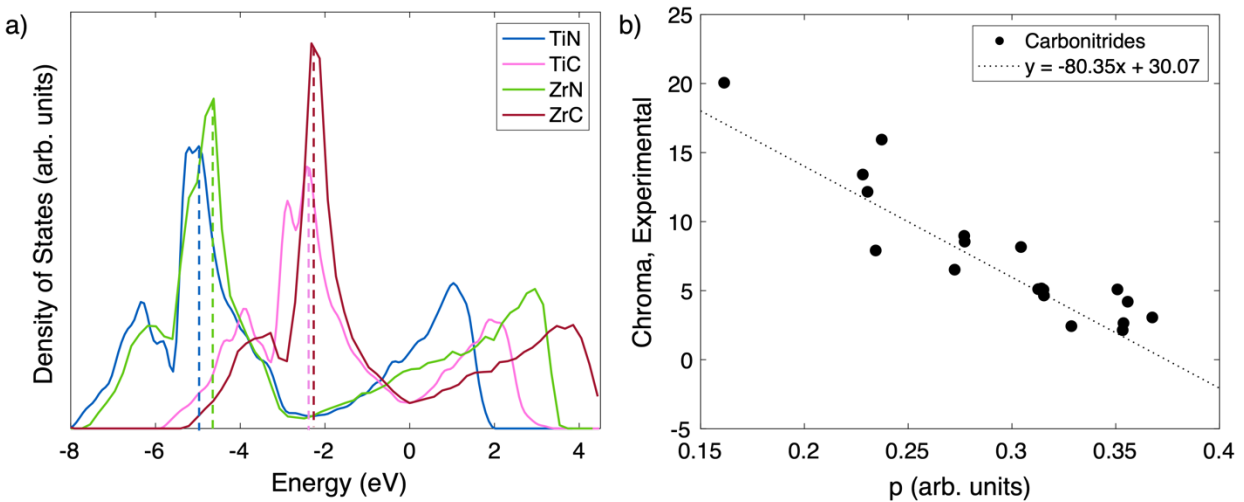


Figure 3.4: (a) Example total density of states (in arbitrary units) calculated via DFT for B1-structured TiN, TiC, ZrN, and ZrC at 0 kelvin. Dashed lines mark the anion-p/metal-d valence band peak energies. Energy = 0 is defined as the Fermi level. (b) The chroma of carbonitrides can be predicted from the density of states and the precursor monocarbides and mononitrides using p , the standard deviation of the constituent valence band peak energies divided by their weighted average.

It should be noted that lattice vibrations at finite temperatures – not accounted for in our “static” DFT calculations – may also contribute to enhance DOS-peak broadening. While thermal effects at 300 K are expected to be negligible in fairly-harmonic systems as TiC or TiN

(phonon frequencies vary slowly with temperature [40]), a more substantial DOS-peak broadening may be observed for carbonitrides with valence electron concentrations close to $10 e^-$ /formula-unit. Indeed, group 5 nitrides (with VEC = $10 e^-$ /f.u.) are dynamically stabilized in the B1 structure thanks to anharmonic lattice vibrations [27,28] and have acoustic phonon frequencies which change rapidly with temperature [40]. For cases of alloys that contain Cr, one should also expect effective values of band broadening and Fermi energies to be influenced by electronic-spin degrees of freedom (more details given in DFT methods section).

By applying corrections for pseudogap energy ($E_{pg,adj}$, Eq. 3.16), hue (h^*_{adj} , Eq. 3.17), and chroma (C^*_{adj} , Eq. 3.18) to the rule of mixtures (ROM) optical properties, it is possible to predict color combinations for any solid-solution B1-structured multicomponent carbonitride. Shown in Figure 3.5 are all possible combinations of $M(C_xN_{1-x})$, where x is incremented in 10 atomic percent steps from 0 to 1, and M is any combination of up to five metals from (Ti, Zr, Hf, V, Nb, Ta), also incremented in 10 atomic percent steps. Chroma values are brightest in the yellow region for nitride mixtures ($h^* = 70-90$), but tunability using carbon additions and variations in metal composition grants access to almost all hues on the color wheel, with chroma values greater than 5.

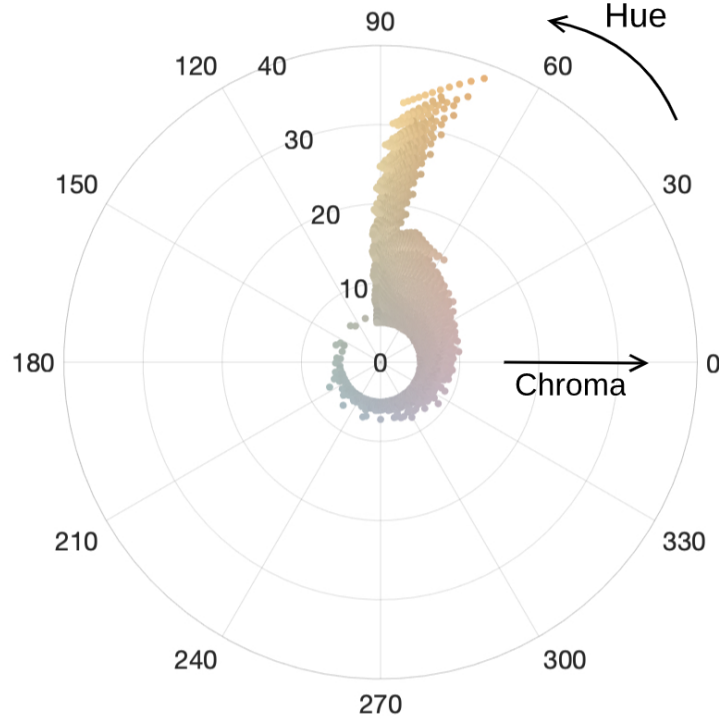


Figure 3.5: The predicted hues and chromas of all possible combinations of carbonitrides with up to 5 metals (Ti, Zr, Hf, V, Nb, Ta), having $C_{adj}^* > 5$ and $L_{ROM}^* > 70$. Hue (h_{adj}^* , theta axis) represents the angle around the color wheel and chroma (C_{adj}^* , r-axis) represents the saturation of the color. Each point on the plot represents one composition, and the color of the point is the material's predicted color. L_{ROM}^* , C_{adj}^* , and h_{adj}^* predictions are based on ROM, with chroma and hue adjustments applied.

Lightness (L_{ROM}^*) predictions in Fig. 3.5 are based on rule of mixtures averages of precursors. All carbonitride materials analyzed had $60 < L^* < 80$, and within this range, L^* does not contribute as significantly to the material's color appearance as chroma and hue. Niyomsoan *et al.* showed that L^* decreases as nitrogen stoichiometry increases from 0.81 to 0.94 in thin films of ZrN but showed little change in L^* with stoichiometry variation in TiN [3]. Significant anion sub-stoichiometry is common in transition metal carbides and nitrides, but anion concentrations are not easily controlled in the solid-state powder-processing synthesis techniques used in this work, especially nitrogen concentration. Anion vacancies additionally contribute to an increase in metallic bond character, contributing to transition metal 3d defect states that

increase the density of states at the pseudogap [41,42], which would decrease the specificity of electronic transitions and give rise to less saturated colors.

3.4 Conclusions

In the case of mono-cation ceramics, such as monocarbides (e.g. TiC and ZrC) and mononitrides (e.g. TiN and ZrN), the color appearance is largely fixed by the cation-anion bonding structures and the resulting electronic density of states. Conversely, in multi-cation and multi-anion compounds, the density of states can be systematically varied by changes in cation and anion ratios. That is, multicomponent materials are inherently capable of and provide ample opportunity for having their color appearance tailored. As demonstrated in this work, mixing monocarbides and mononitrides, which on their own are limited in color from gray to yellow, unlocks color appearances with hues including orange, pink, purple, and blue.

We found that this color modification is enabled by complete tunability of pseudogap energies based on composition of carbonitrides. The brightest colors occur with pseudogap energy of 2.5-3.0 eV for nitrides and carbonitrides, have a golden-yellow color. However, there currently is a trade-off to consider for creating certain colors: as carbonitride colors are red shifted, by increasing carbon concentration or manipulating metal atom concentrations, color saturations (chroma) decrease. This occurs due to (1) broadening in the p-d valence band peaks of the electronic density of states and (2) valence band shift toward the Fermi level, which decrease the energy selectivity of photon absorption processes.

To expand the range of highly saturated colors, future work includes introducing additional anions, i.e. oxygen, into the same crystal structure or expanding to other crystal systems; controlling for anion stoichiometry; doping with other elements to modify plasma

frequency; manipulating surface finishes; and creating engineered multiphase materials whose microstructure can act as color pixels.

The prediction parameters for pseudogap energy, chroma, and hue developed in this work provide the ability to predict the color appearance of any compositional variation of Group 4/5 B1-structured carbonitride materials. The guiding principles used to understand color appearance through the lens of electronic structure extend to many material systems, laying the groundwork for tunable optical properties in other multicomponent systems.

Acknowledgements

The authors would like to acknowledge Dr. Javier Garay and Meir Shachar, for helpful discussions on absorption phenomena in nitrides. O.F.D. would also like to thank Dr. Andrew Zhao for many helpful discussions and for editing the manuscript. This work was partially supported through access and utilization of the UC San Diego, Dept. of NanoEngineering's Materials Research Center (NEMRC). Support from the Oerlikon Group to Professor Vecchio's research group is acknowledged. DFT calculations were carried out using the resources provided by the Swedish National Infrastructure for Computing (SNIC), partially funded by the Swedish Research Council through Grant Agreement N° VR-2015-04630. D.G.S. gratefully acknowledges financial support from the Competence Center Functional Nanoscale Materials (FunMat-II) (Vinnova Grant No. 2016-05156) and the Swedish Research Council (VR) through Grant N° VR-2021-04426.

Chapter 3, in full, has been submitted for publication of the material "Color and pseudogap tunability in multicomponent carbonitrides" as it may appear in *Materials & Design*

2022. Dippo, Olivia F.; Sangiovanni, Davide G.; Wenger, Emma H.; Vecchio, Kenneth S. The dissertation author was the primary investigator and author of this material.

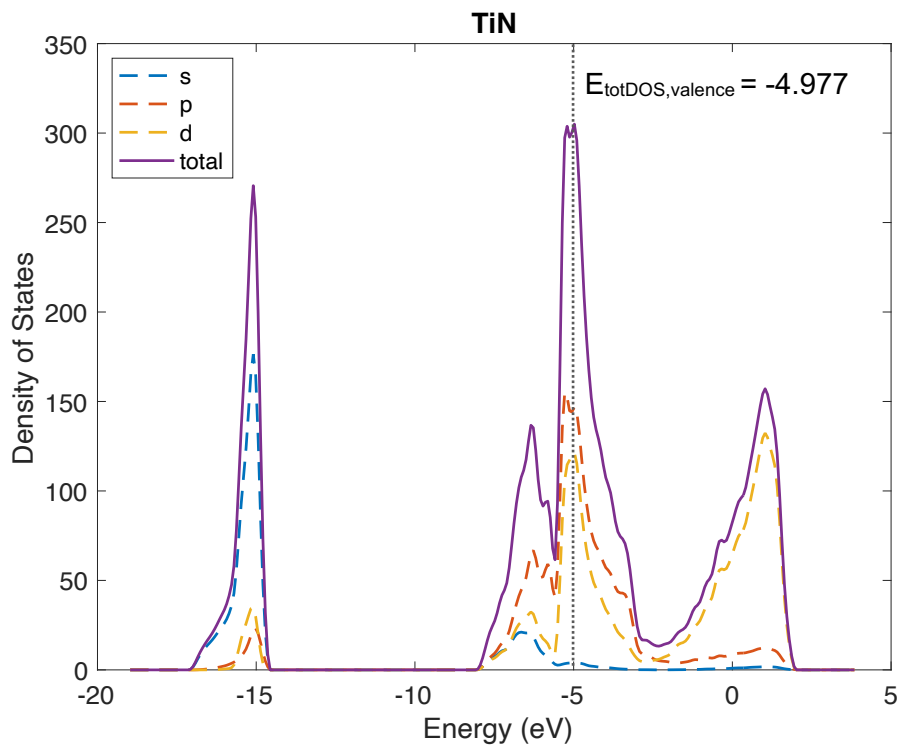
Supplementary Information

Supplementary Table 3.1: Precursor monocarbide and mononitride samples, with their measured CIELCh color values from wavelength-dependent reflection, pseudogap energies (E_{pg}) from Tauc plot analysis, and the energy of the total valence band peak in the calculated electronic density of states ($E_{valence, totDOS}$).

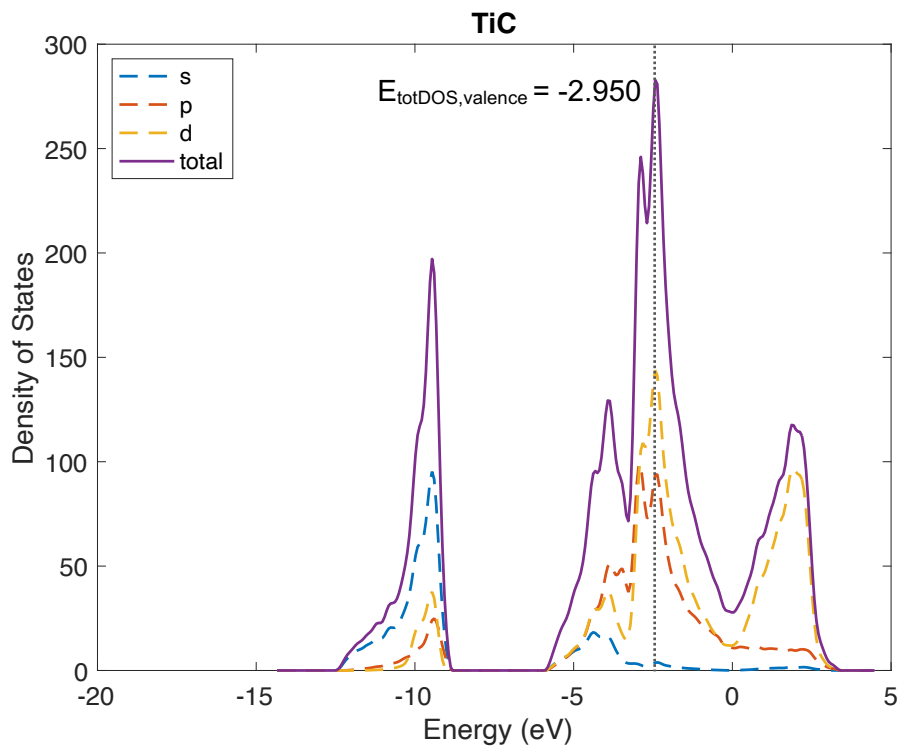
Composition	L	C	H	E_{pg} (eV)	$E_{valence, totDOS}$ (eV)
TiN	76.13	38.13	81.97	2.58	-4.977
ZrN	86.62	32.87	97.39	2.94	-4.627
HfN	76.75	5.06	86.35	3.83	-5.497
VN	70.12	11.06	79.45	2.88	-5.646
NbN	77.05	3.4	82.04	3.29	-5.878
TaN	71.6	4.77	83.06	3.92	-6.770
CrN (contains CrN and Cr ₂ N)	76.62	1.76	61.04	1.72	-5.676
TiC	74.04	0.52	10.25	1.11	-2.950
ZrC	72.03	3.17	78.9	1.79	-2.319
HfC	66.32	4.59	79.44	2.03	-2.429
VC	76.41	3.74	56.84	1.76	-3.875
NbC	73.11	6.16	58.78	1.95	-4.336
TaC	71.91	8.62	76.29	2.22	-4.869
CrC (contains Cr ₃ C ₂ , Cr ₇ C ₃ , and Cr ₂₃ C ₆)	79.03	3.55	73.09	2.03	-4.246

Supplementary Table 3.2: Carbonitride samples analyzed in this work, with their measured CIELCh color values from wavelength-dependent reflection and pseudogap energies (E_{pg}) from Tauc plot analysis.

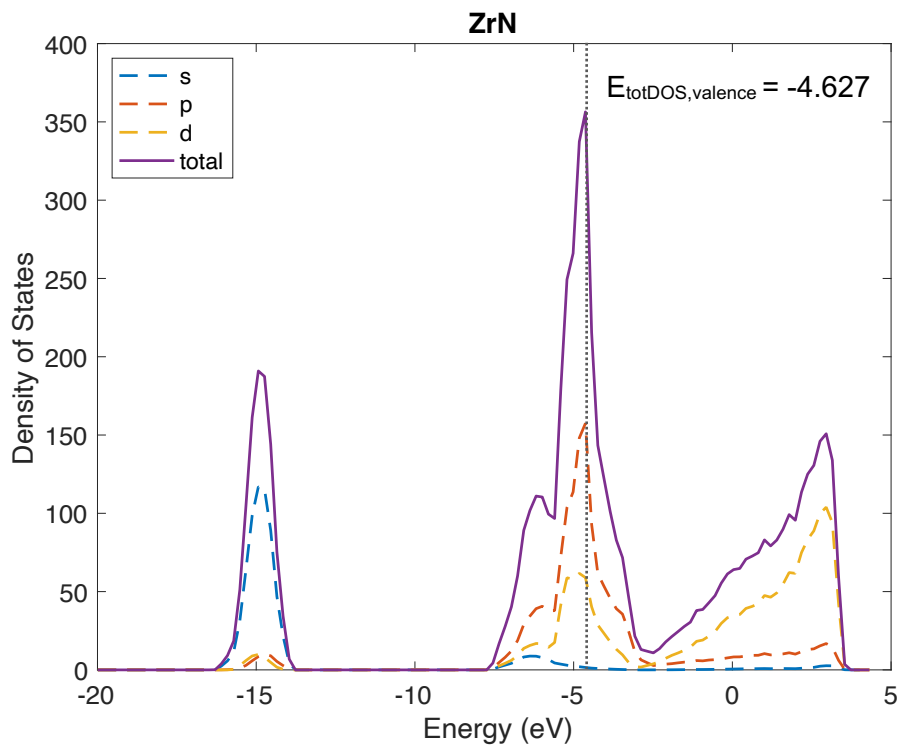
Composition	L	C	H	E_{pg} (eV)
(HfNbTaTiZr)N [Ref. 20]	77.86	14.12	84.06	3.19
(CrNbTaTiV)N [Ref. 20]	77.16	8.76	82.85	3.01
(CrHfNbTaTi)N [Ref. 20]	68.13	11.40	82.56	2.92
(CrHfNbTiZr)N [Ref. 20]	73.27	17.07	79.29	2.50
(CrHfTaTiZr)N [Ref. 20]	75.09	17.98	84.06	2.71
(HfNbTaTiZr)(CN) [Ref. 20]	69.25	17.35	63.33	2.22
(CrNbTaTiV)(CN) [Ref. 20]	76.06	8.02	76.68	2.22
(CrHfNbTaTi)(CN) [Ref. 20]	71.40	11.47	65.14	2.15
(CrHfNbTiZr)(CN) [Ref. 20]	65.53	7.55	38.70	1.93
(CrHfTaTiZr)(CN) [Ref. 20]	57.44	7.30	41.57	1.90
(Cr _{0.2} Hf _{0.4} Zr _{0.4})(C _{0.7} N _{0.3})	64.25	2.14	234.98	1.40
(Ti _{0.2} Zr _{0.4} Hf _{0.4})(C _{0.7} N _{0.3})	64.70	3.06	268.01	1.51
(Cr _{0.2} Hf _{0.2} Nb _{0.2} Ti _{0.2} Zr _{0.2})(C _{0.75} N _{0.25})	67.06	2.43	340.26	1.67
(Cr _{0.2} Hf _{0.2} Ta _{0.2} Ti _{0.2} Zr _{0.2})(C _{0.75} N _{0.25})	66.65	2.65	344.47	1.70
Zr ₁ (C _{0.1} N _{0.9})	79.61	40.79	89.16	2.69
(Ti _{0.2} Zr _{0.8})(C _{0.6} N _{0.4})	61.28	4.20	298.90	1.66
(Ti _{0.1} Zr _{0.9})(C _{0.6} N _{0.4})	60.01	5.09	338.10	1.82
Ti ₁ (C _{0.4} N _{0.6})	63.30	4.65	20.16	1.83
(Ti _{0.9} Zr _{0.1})(C _{0.4} N _{0.6})	63.22	5.07	20.84	1.83
(Ti _{0.9} Nb _{0.1})(C _{0.4} N _{0.6})	65.64	6.52	37.40	1.91
(Ti _{0.7} Zr _{0.3})(C _{0.4} N _{0.6})	62.56	5.16	16.91	1.85
Ti ₁ (C _{0.3} N _{0.7})	63.58	8.97	39.18	1.96
(Ti _{0.9} Zr _{0.1})(C _{0.3} N _{0.7})	63.29	8.55	38.96	1.95
(Ti _{0.9} Hf _{0.1})(C _{0.3} N _{0.7})	63.08	7.91	36.73	1.94
Ti ₁ (C _{0.2} N _{0.8})	65.40	13.41	50.89	2.07
(Ti _{0.9} Hf _{0.1})(C _{0.2} N _{0.8})	64.17	12.16	46.00	2.03
Ti ₁ (C _{0.1} N _{0.9})	68.46	20.06	63.45	2.17
(Ti _{0.84} Hf _{0.04} Nb _{0.04} V _{0.04} Zr _{0.04})(C _{0.2} N _{0.8})	65.67	15.94	50.53	2.12
(Ti _{0.2} Zr _{0.2} Hf _{0.2} V _{0.2} Nb _{0.2} Ta _{0.2})(C _{0.5} N _{0.5})	70.84	8.16	66.17	2.04
(Ti _{0.6} Zr _{0.4})(C _{0.5} N _{0.5})	61.47	5.11	28.83	1.81
(Cr _{0.4} Ti _{0.6})(C _{0.1} N _{0.9})	69.92	11.44	72.87	2.27
(Cr _{0.3} Ti _{0.4} Zr _{0.3})(C _{0.1} N _{0.9})	68.03	8.65	61.84	2.00
(Nb _{0.1} Ti _{0.5} V _{0.3} Zr _{0.1})(C _{0.1} N _{0.9})	73.45	13.49	77.73	2.37
(Nb _{0.8} Ta _{0.1} Zr _{0.1})(C _{0.5} N _{0.5})	78.42	9.04	79.51	2.41



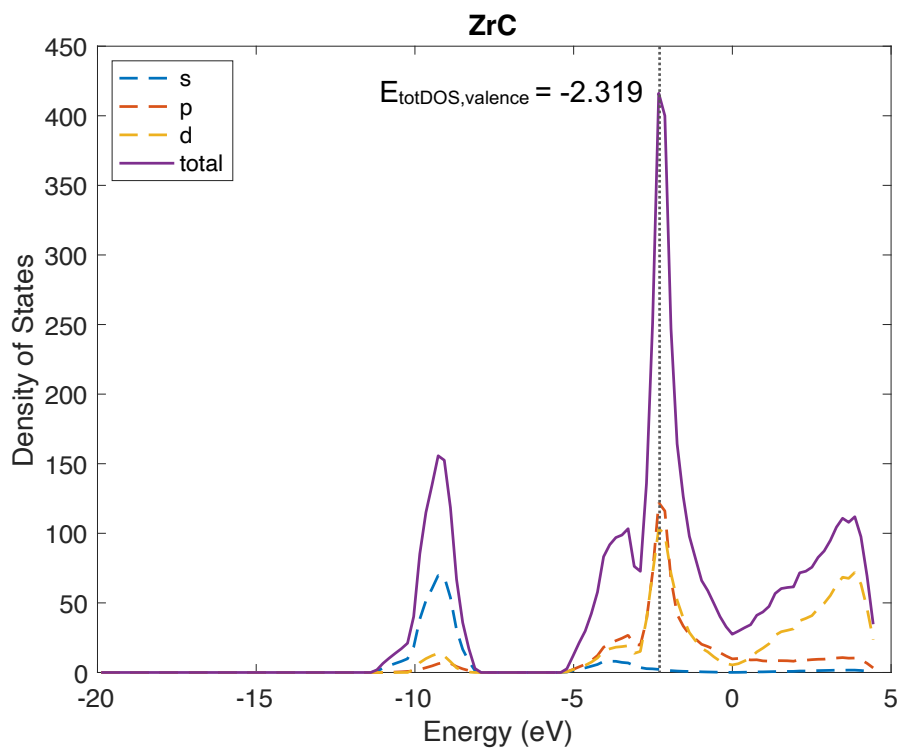
Supplementary Figure 3.1: Density of states for B1-structured TiN.



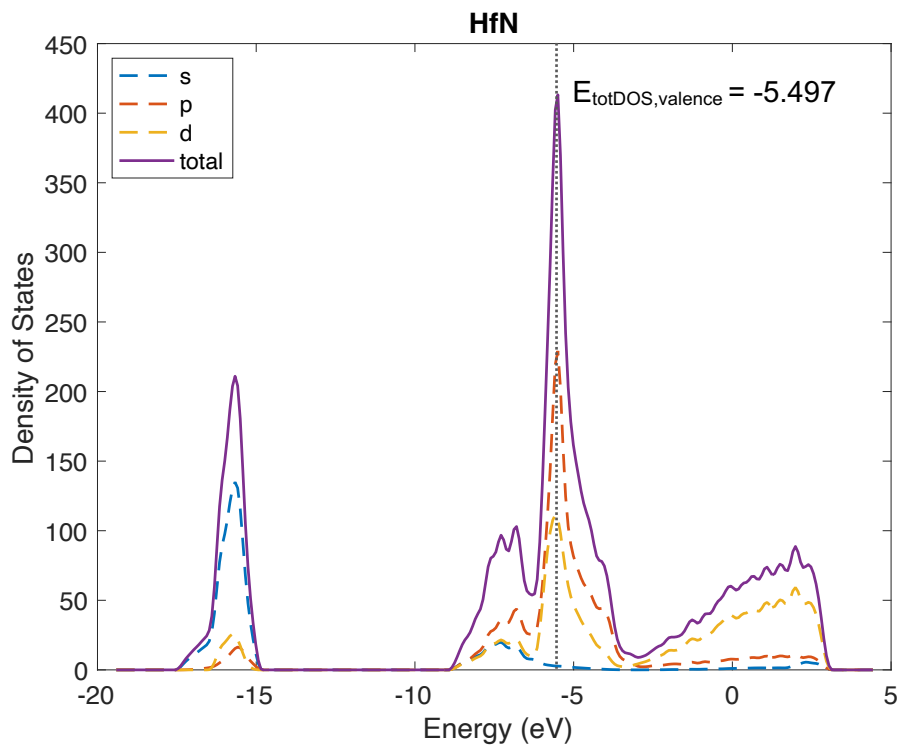
Supplementary Figure 3.2: Density of states for B1-structured TiC.



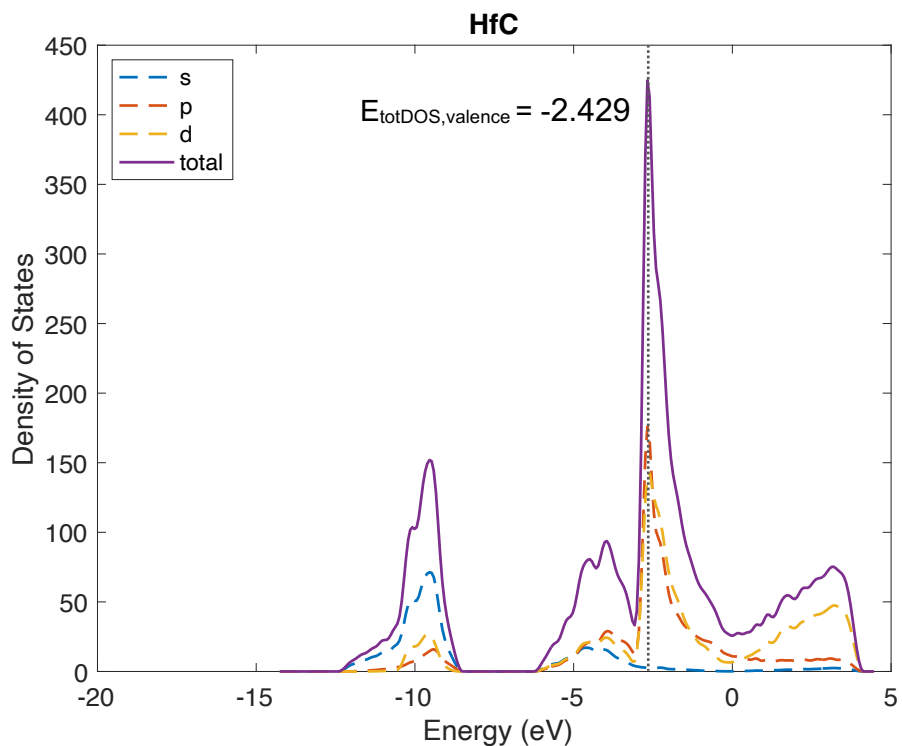
Supplementary Figure 3.3: Density of states for B1-structured ZrN.



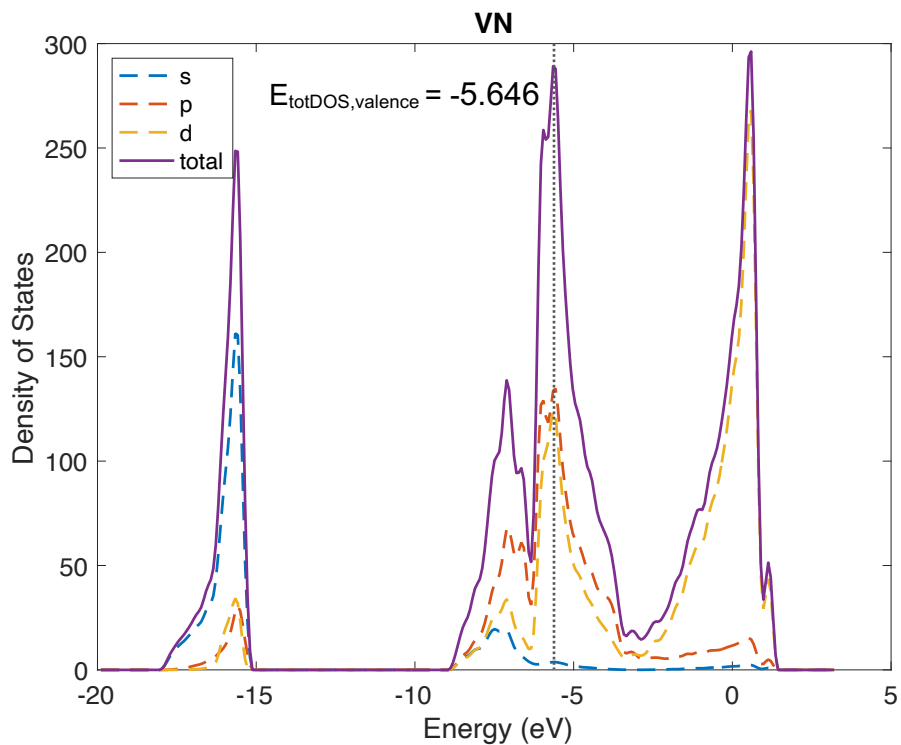
Supplementary Figure 3.4: Density of states for B1-structured ZrC.



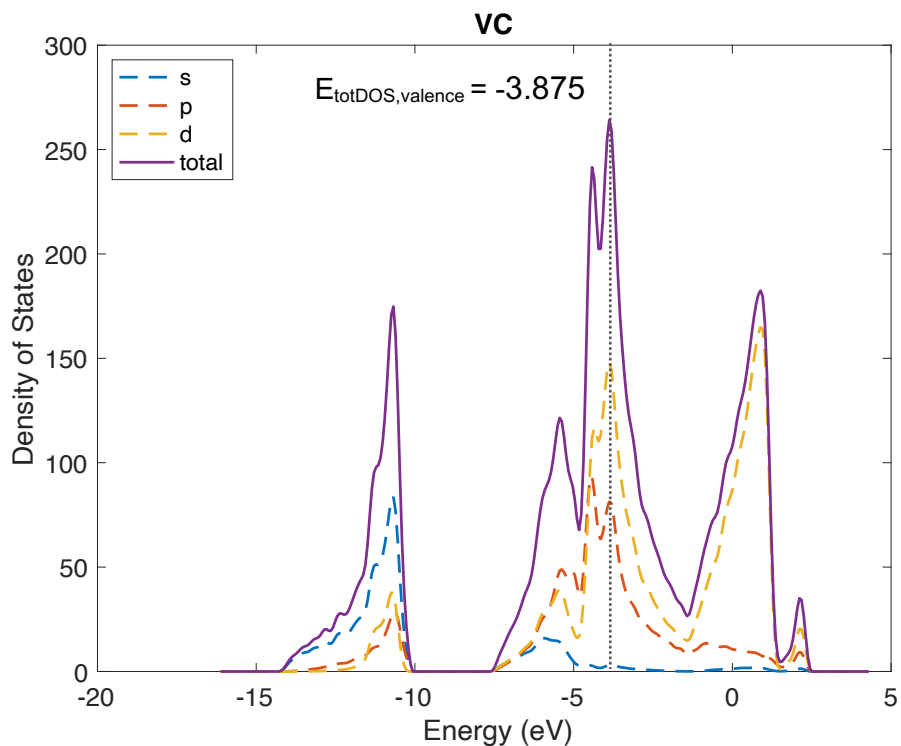
Supplementary Figure 3.5: Electronic density of states for B1-structured HfN.



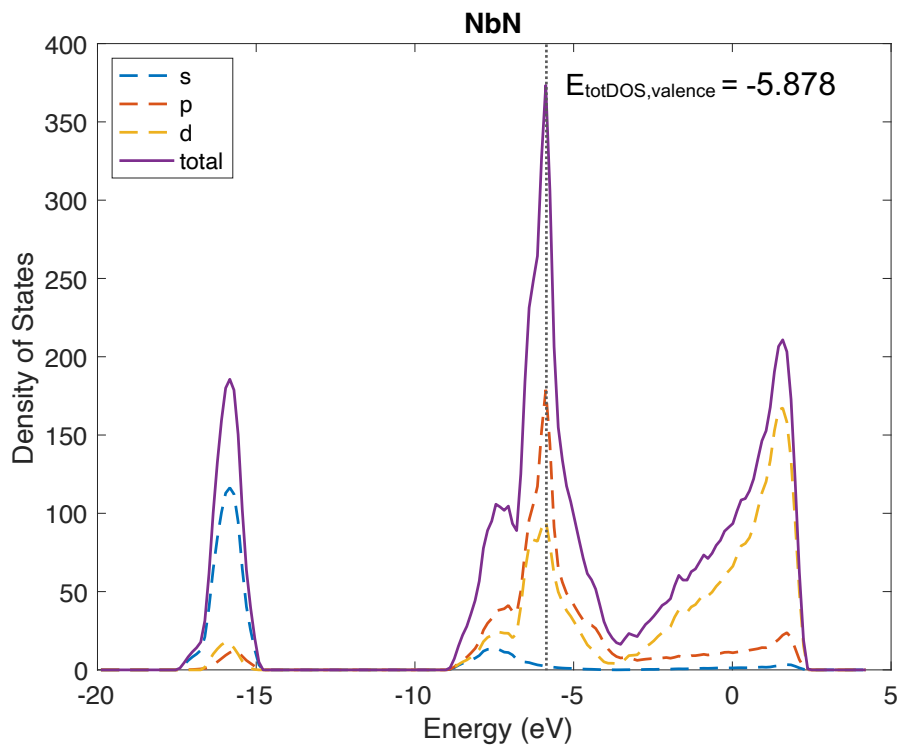
Supplementary Figure 3.6: Electronic density of states for B1-structured HfC.



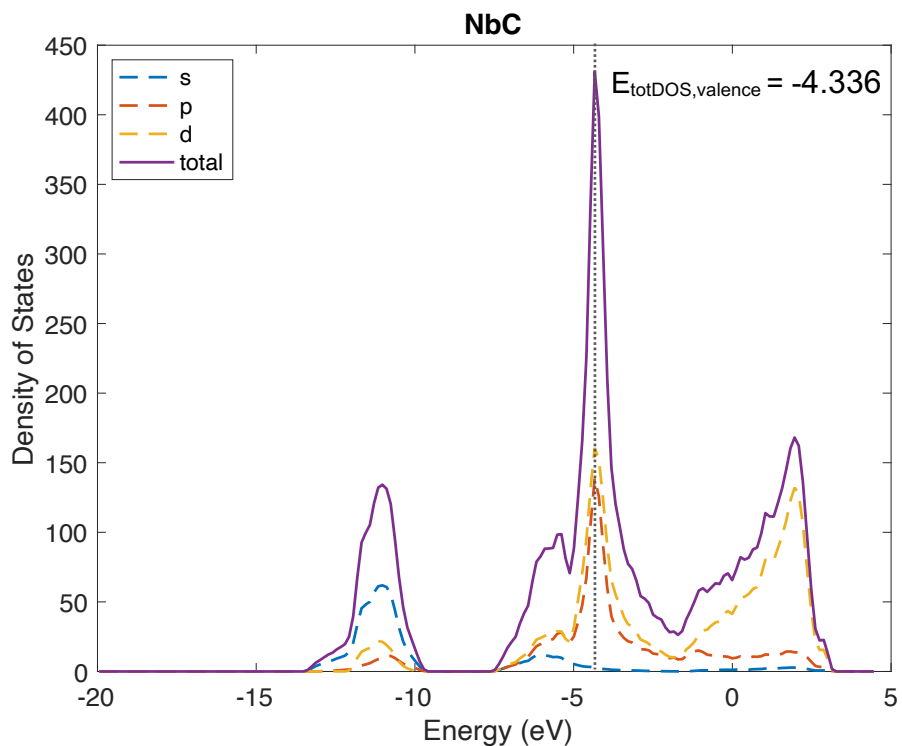
Supplementary Figure 3.7: Electronic density of states for B1-structured VN.



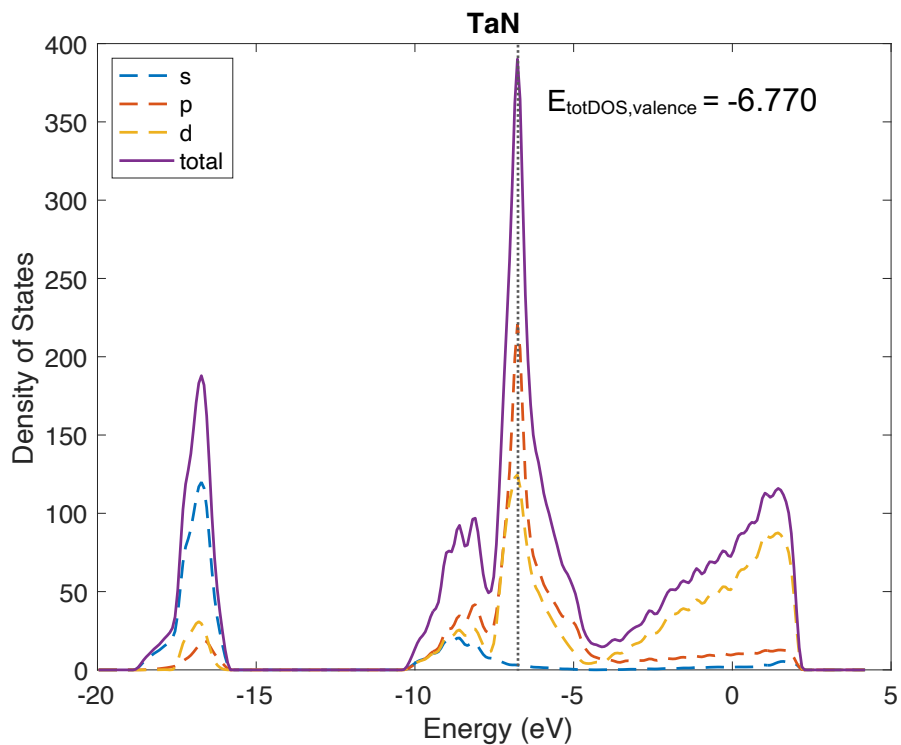
Supplementary Figure 3.8: Electronic density of states for B1-structured VC.



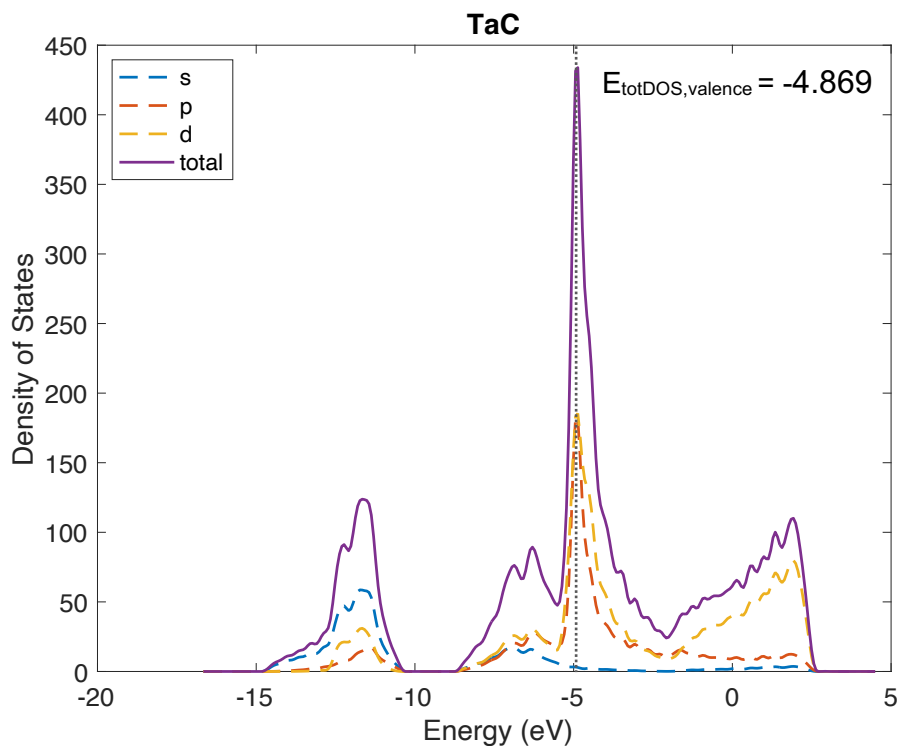
Supplementary Figure 3.9: Electronic density of states for B1-structured NbN.



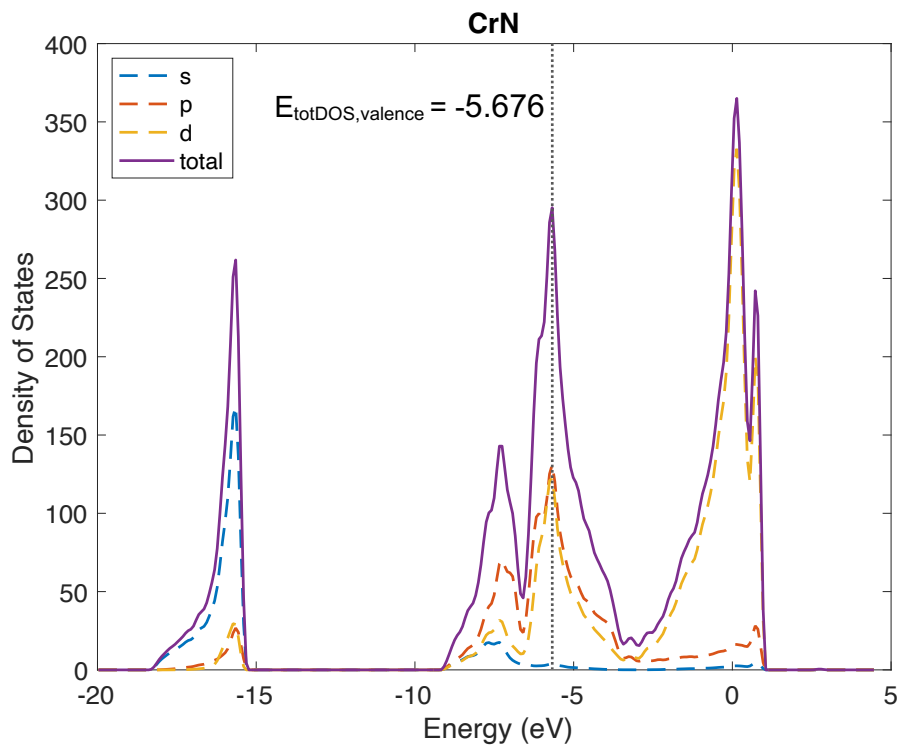
Supplementary Figure 3.10: Electronic density of states for B1-structured NbC.



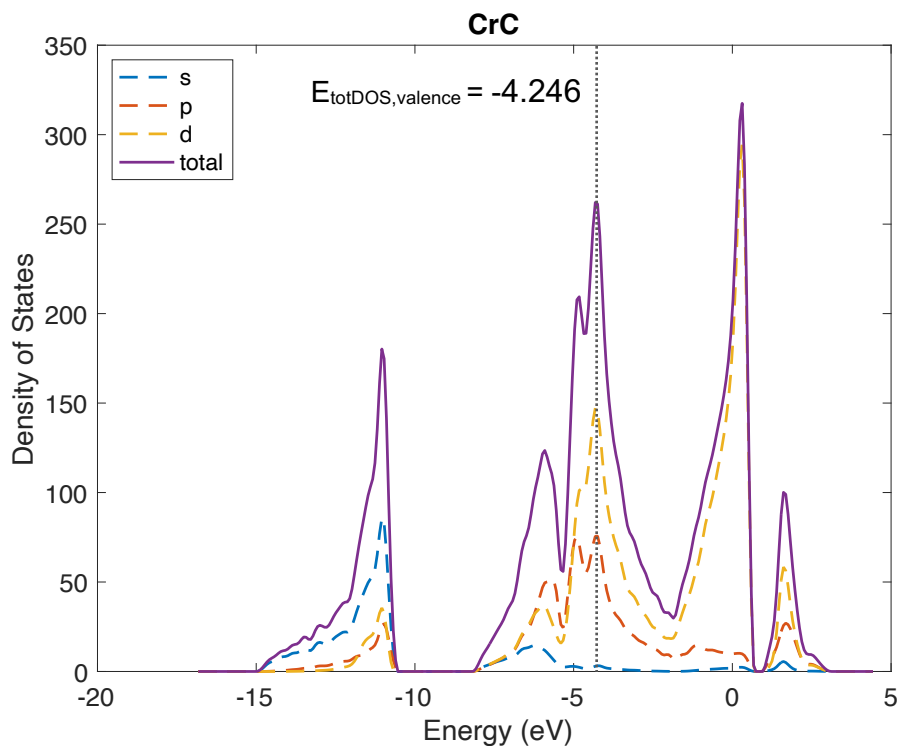
Supplementary Figure 3.11: Electronic density of states for B1-structured TaN.



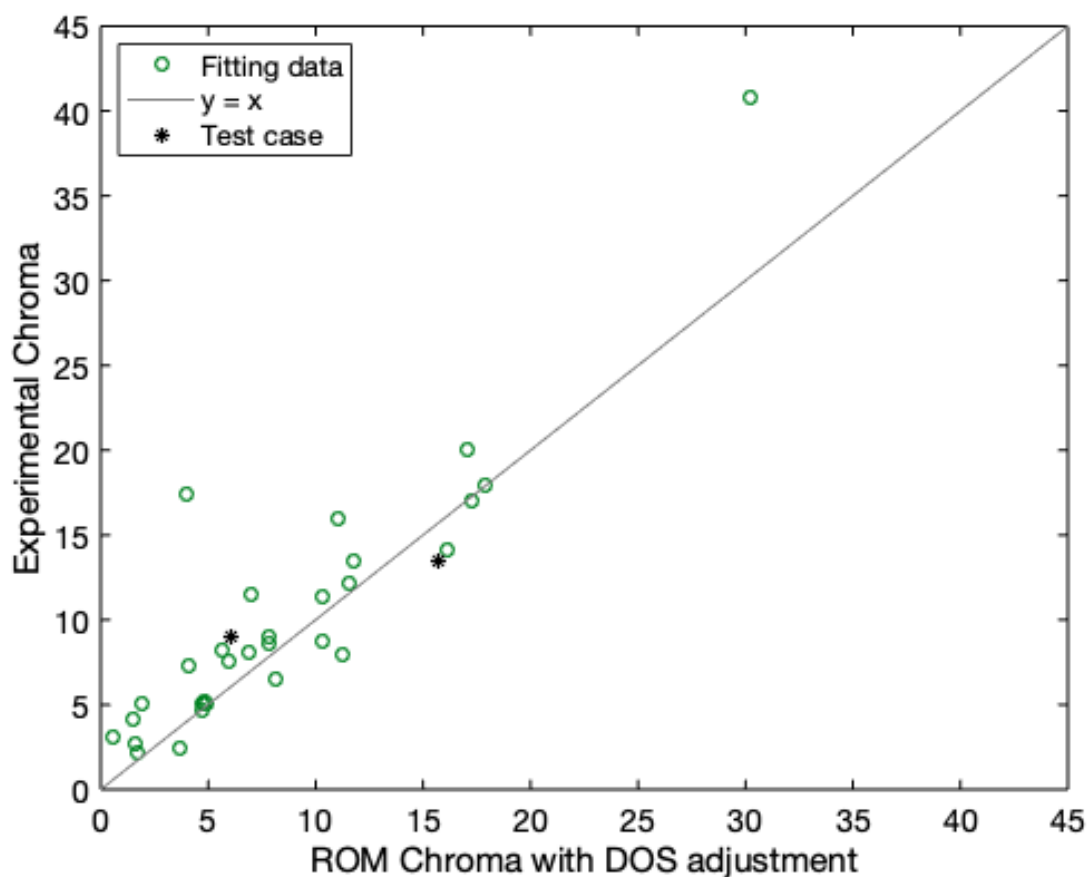
Supplementary Figure 3.12: Electronic density of states for B1-structured TaC.



Supplementary Figure 3.13: Electronic density of states for B1-structured CrN.



Supplementary Figure 3.14: Electronic density of states for B1-structured CrC.



Supplementary Figure 3.15: Experimental chroma vs ROM Chroma with DOS adjustment (Eq. 3.18 in main text). The fitting data was used to fit the chroma model. In the test case, two materials with approximately the same hue but different chroma values according to the DOS adjustment were successfully predicted and synthesized. All color parameters for test case compositions $(\text{Nb}_{0.1}\text{Ti}_{0.5}\text{V}_{0.3}\text{Zr}_{0.1})(\text{C}_{0.1}\text{N}_{0.9})$ and $(\text{Nb}_{0.8}\text{Ta}_{0.1}\text{Zr}_{0.1})(\text{C}_{0.5}\text{N}_{0.5})$ can be found in Supplementary Table 3.2.

References

- [1] S.P. Denker, Cohesion in cubic refractory monocarbides, mononitrides and monoxides, *Journal of The Less-Common Metals*. 14 (1968) 1–22. [https://doi.org/10.1016/0022-5088\(68\)90198-7](https://doi.org/10.1016/0022-5088(68)90198-7).
- [2] H.O. Pierson, *Handbook of refractory carbides and nitrides : properties, characteristics, processing, and applications*, Noyes Publications, 1996.
- [3] S. Niyomsoan, W. Grant, D.L. Olson, B. Mishra, Variation of color in titanium and zirconium nitride decorative thin films, *Thin Solid Films*. 415 (2002) 187–194. [https://doi.org/10.1016/S0040-6090\(02\)00530-8](https://doi.org/10.1016/S0040-6090(02)00530-8).
- [4] A.M. Bonnot, H. Belkhir, D. Pailharey, Optical Properties Of Titanium And Zirconium Carbonitride Thin Films, *Optical Materials Technology for Energy Efficiency and Solar Energy Conversion V*. 0653 (1986) 215. <https://doi.org/10.1117/12.938331>.
- [5] A. Mumtaz, W.H. Class, Color of Titanium Nitride Prepared By Reactive DC Magnetron Sputtering., *Journal of Vacuum Science and Technology*. 20 (1981) 345–348. <https://doi.org/10.1116/1.571461>.
- [6] S.G. Steinemann, W. Wolf, R. Podloucky, Color and Optical Properties, *Intermetallic Compounds - Principles and Practice*. 3 (2002) 231–244. <https://doi.org/10.1002/0470845856.ch12>.
- [7] H. Allmaier, L. Chioncel, E. Arrigoni, Titanium nitride : A correlated metal at the threshold of a Mott transition, (2009) 1–7. <https://doi.org/10.1103/PhysRevB.79.235126>.
- [8] T.J. Harrington, *High Entropy Carbides: Modeling, Synthesis, and Properties*, 2019. <https://escholarship.org/uc/item/4x88244f>.
- [9] S. Yu, Q. Zeng, A.R. Oganov, G. Frapper, L. Zhang, Phase stability, chemical bonding and mechanical properties of titanium nitrides: A first-principles study, *Physical Chemistry Chemical Physics*. 17 (2015) 11763–11769. <https://doi.org/10.1039/c5cp00156k>.
- [10] K.E. Saeger, J. Rodies, The colour of gold and its alloys - The mechanism of variation in optical properties, *Gold Bulletin*. 10 (1977) 10–14. <https://doi.org/10.1007/BF03216519>.
- [11] Y.B. Jeong, S.H. Hong, J.T. Kim, H.J. Park, Y.S. Kim, H.D. Lee, J.K. Lee, S.C. Mun, Y.J. Hwang, K. Heo, K.B. Kim, Investigation on the Relationship Between Transition Energy and the Color Change of Cu–M Alloys, *Metals and Materials International*. 25 (2019) 539–545. <https://doi.org/10.1007/s12540-018-0205-5>.
- [12] H.A.A. El-Fattah, I.S. El-Mahallawi, M.H. Shazly, W.A. Khalifa, Optical properties and microstructure of TiN_xO_y and TiN thin films before and after annealing at different conditions, *Coatings*. 9 (2019) 1–15. <https://doi.org/10.3390/coatings9010022>.

- [13] D.G. Sangiovanni, F. Tasnádi, T. Harrington, M. Odén, K.S. Vecchio, I.A. Abrikosov, Temperature-dependent elastic properties of binary and multicomponent high-entropy refractory carbides, *Materials & Design*. 204 (2021) 109634. <https://doi.org/10.1016/J.MATDES.2021.109634>.
- [14] W.M. Mellor, K. Kaufmann, O.F. Dippo, S.D. Figueroa, G.D. Schrader, K.S. Vecchio, Development of ultrahigh-entropy ceramics with tailored oxidation behavior, *Journal of the European Ceramic Society*. 41 (2021) 5791–5800. <https://doi.org/10.1016/J.JEURCERAMSOC.2021.05.010>.
- [15] T.J. Harrington, J. Gild, P. Sarker, C. Toher, C.M. Rost, O.F. Dippo, C. McElfresh, K. Kaufmann, E. Marin, L. Borowski, P.E. Hopkins, J. Luo, S. Curtarolo, D.W. Brenner, K.S. Vecchio, Phase stability and mechanical properties of novel high entropy transition metal carbides, *Acta Materialia*. 166 (2019) 271–280. <https://doi.org/10.1016/j.actamat.2018.12.054>.
- [16] X. Chen, Y. Wu, High-entropy transparent fluoride laser ceramics, *Journal of the American Ceramic Society*. 103 (2020) 750–756. <https://doi.org/10.1111/JACE.16842>.
- [17] C.Y. He, X.L. Qiu, D.M. Yu, S.S. Zhao, H.X. Guo, G. Liu, X.H. Gao, Greatly enhanced solar absorption via high entropy ceramic AlCrTaTiZrN based solar selective absorber coatings, *Journal of Materiomics*. 7 (2021) 460–469. <https://doi.org/10.1016/J.JMAT.2020.11.010>.
- [18] Abhishek Sarkar, Christoph Loho, Leonardo Velasco, Tiju Thomas, S. S. Bhattacharya, Horst Hahn, Ruzica Djenadic, Multicomponent equiatomic rare earth oxides with a narrow band gap and associated praseodymium multivalency, *Dalton Transactions*. 46 (2017) 12167–12176. <https://doi.org/10.1039/C7DT02077E>.
- [19] D. Berardan, A.K. Meena, S. Franger, C. Herrero, N. Dragoe, Controlled Jahn-Teller distortion in (MgCoNiCuZn)O-based high entropy oxides, *Journal of Alloys and Compounds*. 704 (2017) 693–700. <https://doi.org/10.1016/J.JALLCOM.2017.02.070>.
- [20] O.F. Dippo, N. Mesgarzadeh, T.J. Harrington, G.D. Schrader, K.S. Vecchio, Bulk high-entropy nitrides and carbonitrides, *Scientific Reports*. 10 (2020) 1–11. <https://doi.org/10.1038/s41598-020-78175-8>.
- [21] J. Tauc, R. Grigorovici, A. Vancu, Optical Properties and Electronic Structure of Amorphous Germanium, *Physica Status Solidi (b)*. 15 (1966) 627–637. <https://doi.org/10.1002/PSSB.19660150224>.
- [22] P. Kubelka, F. Munk, *An Article on Optics of Paint Layers*, (1931).
- [23] D.B. Judd, *Color in business, science, and industry*, John Wiley & Sons, Ltd, New York, 1952. <https://doi.org/10.1002/JPS.3030421221>.

- [24] G. Kresse, J. Furthmüller, Efficiency of ab-initio total energy calculations for metals and semiconductors using a plane-wave basis set, *Computational Materials Science*. 6 (1996) 15–50. [https://doi.org/10.1016/0927-0256\(96\)00008-0](https://doi.org/10.1016/0927-0256(96)00008-0).
- [25] G. Kresse, D. Joubert, From ultrasoft pseudopotentials to the projector augmented-wave method, *Physical Review B*. 59 (1999) 1758. <https://doi.org/10.1103/PhysRevB.59.1758>.
- [26] J.P. Perdew, K. Burke, M. Ernzerhof, Generalized Gradient Approximation Made Simple, *Physical Review Letters*. 77 (1996) 3865. <https://doi.org/10.1103/PhysRevLett.77.3865>.
- [27] A.B. Mei, O. Hellman, N. Wireklint, C.M. Schlepütz, D.G. Sangiovanni, B. Alling, A. Rockett, L. Hultman, I. Petrov, J.E. Greene, Dynamic and structural stability of cubic vanadium nitride, *Physical Review B - Condensed Matter and Materials Physics*. 91 (2015) 054101. <https://doi.org/10.1103/PHYSREVB.91.054101>.
- [28] G. Rydén, Ab initio lattice dynamics and Anharmonic effects in refractory Rock-salt structure TaN ceramic, 2020. <http://urn.kb.se/resolve?urn=urn:nbn:se:liu:diva-174208> (accessed November 28, 2021).
- [29] E.I. Isaev, S.I. Simak, I.A. Abrikosov, R. Ahuja, Y.K. Vekilov, M.I. Katsnelson, A.I. Lichtenstein, B. Johansson, Phonon related properties of transition metals, their carbides, and nitrides: A first-principles study, *Journal of Applied Physics*. 101 (2007) 123519. <https://doi.org/10.1063/1.2747230>.
- [30] K. Balasubramanian, S. v. Khare, D. Gall, Valence electron concentration as an indicator for mechanical properties in rocksalt structure nitrides, carbides and carbonitrides, *Acta Materialia*. 152 (2018) 175–185. <https://doi.org/10.1016/j.actamat.2018.04.033>.
- [31] L.M. Corliss, N. Elliott, J.M. Hastings, Antiferromagnetic Structure of CrN, *Physical Review*. 117 (1960) 929. <https://doi.org/10.1103/PhysRev.117.929>.
- [32] R.M. Ibberson, R. Cywinski, The magnetic and structural transitions in CrN and (CrMo)N, *Physica B: Condensed Matter*. 180–181 (1992) 329–332. [https://doi.org/10.1016/0921-4526\(92\)90749-I](https://doi.org/10.1016/0921-4526(92)90749-I).
- [33] I. Stockem, A. Bergman, A. Glensk, T. Hickel, F. Körmann, B. Grabowski, J. Neugebauer, B. Alling, Anomalous Phonon Lifetime Shortening in Paramagnetic CrN Caused by Spin-Lattice Coupling: A Combined Spin and Ab Initio Molecular Dynamics Study, *Physical Review Letters*. 121 (2018) 125902. <https://doi.org/10.1103/PHYSREVLETT.121.125902>.
- [34] N. Shulumba, B. Alling, O. Hellman, E. Mozafari, P. Steneteg, M. Odén, I.A. Abrikosov, Vibrational free energy and phase stability of paramagnetic and antiferromagnetic CrN from ab initio molecular dynamics, *Physical Review B - Condensed Matter and Materials Physics*. 89 (2014) 174108. <https://doi.org/10.1103/PHYSREVB.89.174108>.

- [35] A. Schlegel, P. Wachter, J.J. Nickl, H. Lingg, Optical properties of TiN and ZrN, *Journal of Physics C: Solid State Physics*. 10 (1977) 4889–4896. <https://doi.org/10.1088/0022-3719/10/23/022>.
- [36] G.G. Fuentes, E. Elizalde, J.M. Sanz, Optical and electronic properties of TiCxNy films, *Journal of Applied Physics*. 90 (2001) 2737–2743. <https://doi.org/10.1063/1.1394157>.
- [37] F. Lévy, P. Hones, P.E. Schmid, R. Sanjinés, M. Diserens, C. Wiemer, Electronic states and mechanical properties in transition metal nitrides, *Surface and Coatings Technology*. 120–121 (1999) 284–290. [https://doi.org/10.1016/S0257-8972\(99\)00498-3](https://doi.org/10.1016/S0257-8972(99)00498-3).
- [38] J. Petrů, J. Klíma, The KKR CPA study of electron states in TiCxN1-x, *Zeitschrift Für Physik B Condensed Matter*. 73 (1988) 213–217. <https://doi.org/10.1007/BF01305738>.
- [39] M. Kumar, N. Umezawa, S. Ishii, T. Nagao, Examining the performance of refractory conductive ceramics as plasmonic materials: a theoretical approach, (n.d.) 1–9.
- [40] D.G. Sangiovanni, Mass transport properties of quasiharmonic vs. anharmonic transition-metal nitrides, *Thin Solid Films*. 688 (2019) 137297. <https://doi.org/10.1016/J.TSF.2019.05.016>.
- [41] A. Catellani, P. D’Amico, A. Calzolari, Tailoring the plasmonic properties of metals: The case of substoichiometric titanium nitride, *Physical Review Materials*. 4 (2020) 15201. <https://doi.org/10.1103/PhysRevMaterials.4.015201>.
- [42] H. Höchst, R.D. Bringans, P. Steiner, T. Wolf, Photoemission study of the electronic structure of stoichiometric and substoichiometric TiN and ZrN, *Physical Review B*. 25 (1982) 7183–7191. <https://doi.org/10.1103/PhysRevB.25.7183>.

Conclusions & Future Directions

Conclusions

In Chapter 1, configurational entropy was discussed, including the methods for calculating configurational entropy, the establishment of a new entropy metric for the determination of high- to low- entropy status, and the implications of configurational entropy for ceramics with crystal structures ranging from simple to highly complex. Configurational entropy is arguably the most important feature of high-entropy materials, as configurational entropy predominates any other form of entropy, and significant entropy increases have been linked to increases in phase stability [1–5], decreases in thermal conductivity [6,7] enhancement of mechanical properties [8–10], and more. In other words, engineering configurational entropy enables the enhancement of important material properties, and thus it is critical that entropy determination and thresholding is well-defined and universal.

High-entropy ceramics grew out of the metallic high-entropy alloys community, where many simplifications and assumptions were justifiably made about the entropy in high-symmetry metal alloy systems. However, as these high-entropy ceramic materials continue to increase in complexity as the field expands and matures, it is critical to the accuracy of analyses that the underlying assumptions and implications of configurational entropy in high-entropy materials are examined. Chapter 1 did the vital work of reconciling differences between entropy determinations in various high-entropy materials fields. Simultaneously, the entropy metric (EM) established in Chapter 1 applies consistently to any crystalline solid, marking the first truly universal configurational entropy metric for high-entropy materials.

Chapter 2, “Bulk high-entropy nitrides and carbonitrides,” constitutes an important demonstration of the potential of high-entropy materials with increasing complexity to create

additional increases in configurational entropy and promote entropic enhancement of material properties. The high-entropy carbonitrides in the study were comprised of a multi-anion, multi-cation system, thus these materials had configurational entropy contributions from both the anion and cation lattice. This increase in configurational disorder, i.e., entropy, was tied to an increase in the entropic strengthening effect. That is, the carbonitrides displayed an enhancement in hardness and elastic modulus, almost double that of the nitrides. In addition to entropy, it was found that valence electron concentration (VEC) was an important indicator of mechanical properties, due to an increase in VEC being associated with an increase in metallic bond character, and therefore a decrease in hardness and elastic modulus. These two properties, configurational entropy and VEC, provide important insights into the tunability of mechanical properties in engineered high-entropy ceramics.

The mechanical property enhancement found in the carbonitrides in Chapter 2 paved the way for more discovery of multi-anion effects. In Chapter 3, the optical properties of carbonitrides were analyzed, and similarly, by utilizing mixtures of carbides and nitrides, novel properties were uncovered. Transition metal nitrides and carbides are limited in color from bright yellow to dull gray, but carbonitrides can achieve almost any color on the color wheel. The color appearances are enabled by the pseudogaps present in the electronic density of states of nitrides, carbides, and carbonitrides, which are predictably tunable based on composition. Additionally, it was found that this pseudogap energy controls the hue of the material, as the electron transition energy across the pseudogap determines the energies which are absorbed and reflected by the materials, i.e. their reflection edge. Lastly, it was found that the chroma of carbonitride materials is controlled by the energy spread of the valence band - which becomes broader upon creating solid solutions - and the proximity of the valence band to the Fermi level. Chroma is tied to the

selectivity of photon absorption and reflection phenomena that occur at energies corresponding to the visible range. Prediction parameters for pseudogap energy, hue, and chroma were established, leading to the predictability of color appearance for any compositional variation of the group 4/5 transition metal carbonitrides, and laying the groundwork for predicting color appearances in other multi-anion and/or multi-cation materials.

Future Directions

In Chapter 1, the advancement of high-entropy ceramics into higher complexity and lower symmetry crystal systems was discussed. Crystal structures with higher degrees of complexity can be engineered to have higher entropy, even if composed of the same elements as a lower complexity crystal system. This tunability in entropy and bond type based on crystal structure and elemental arrangement in the crystal structure can lead to further tunability in the entropic strengthening effect observed in high-entropy nitrides and carbonitrides in Chapter 2. Additionally, these novel crystal systems would represent a new class of tunable optical properties.

Combinations of materials with multiple crystal symmetries can also be engineered for material property advantages. High-entropy composite materials can provide favorable combinations of properties, such as mechanical and thermal property tunability in borocarbides [11]. Engineered multiphase materials can also provide advantages for optical properties, with multiple preferred absorption edges. This could lead to an appearance where microstructural phase separation of two phases with different optical properties could act as pixels, creating a blended color on the macroscale as seen by the human eye [12].

Novel colors can also be created by selective additions of anions and/or cations. For example, in the synthesis of TiN thin films it was observed that non-nitrogen anions (carbon or oxygen) contributed to a red-shift in the color appearance [13]. Thus oxynitrides and oxycarbonitrides are the clear potential next steps in expanding tailorable multi-anion systems. In the continual expansion toward compositionally complex multi-anion multi-cation ceramics, increasing the throughput of experiments can be a great asset. This can be accomplished computationally using high-throughput density-functional theory [14] or machine learning techniques [15–17] for material property calculation and screening with minimal human intervention. Alternatively, or in parallel, this can be accomplished using high-throughput experimental methods. Bulk ceramic materials can be synthesized using high-throughput sintering [18], and thin films can be synthesized with various high-throughput methods, such as masking [19].

Thin films are advantageous for high-throughput screening due to their ability to create continuous gradients of material, i.e. infinitesimally small step sizes in compositions, thickness, and/or heat treatment. Thin film synthesis can also be advantageous for controlling anion stoichiometry, especially when anions consist of oxygen, nitrogen, and similar diatomic gaseous molecules that are challenging to control in solid-state synthesis. Other compositional variations can include introduction of small amounts of dopants to create shifts in plasma frequency, electron transition energy, valence band specificity, or other features of the electronic structure.

In the first 12 years of research into multi-principle element alloys, approximately 1 in 1.4 million of the total possibilities were explored [20]. Multi-principle element alloys, unlike multicomponent ceramics, are limited to a solid solution of elements on just one lattice site, and are usually simple face-centered cubic or body-centered cubic structures. The possibilities for

novel ceramics expand greatly when one considers the multitude of crystal structures, anion combinations, cation combinations, and more that have yet to be considered. The complexity of the problem of tunability in ceramic materials - which can be engineered to be single-phase solid solutions, as in Chapter 2, or multiphase materials, with any compositional variation - explodes as the compositional complexity increases. As property tunability in high-entropy and multicomponent ceramics continues to be explored in mechanical, optical, environmental properties and more, so emerges a path toward boundless property tunability in multicomponent ceramic materials.

References

- [1] C.M. Rost, E. Sachet, T. Borman, A. Moballegh, E.C. Dickey, D. Hou, J.L. Jones, S. Curtarolo, J.P. Maria, Entropy-stabilized oxides, *Nature Communications*. 6 (2015) 1–8. <https://doi.org/10.1038/ncomms9485>.
- [2] A. Sarkar, R. Djenadic, D. Wang, C. Hein, R. Kautenburger, O. Clemens, H. Hahn, Rare earth and transition metal based entropy stabilised perovskite type oxides, *Journal of the European Ceramic Society*. 38 (2018) 2318–2327. <https://doi.org/10.1016/j.jeurceramsoc.2017.12.058>.
- [3] S.J. McCormack, A. Navrotsky, Thermodynamics of high entropy oxides, *Acta Materialia*. 202 (2021) 1–21. <https://doi.org/10.1016/j.actamat.2020.10.043>.
- [4] Q.-J. Hong, A. van de Walle, Prediction of the material with highest known melting point from ab initio molecular dynamics calculations, *RAPID COMMUNICATIONS PHYSICAL REVIEW B*. 92 (2015) 20104. <https://doi.org/10.1103/PhysRevB.92.020104>.
- [5] O. Cedillos-Barraza, D. Manara, K. Boboridis, T. Watkins, S. Grasso, D.D. Jayaseelan, R.J.M. Konings, M.J. Reece, W.E. Lee, Investigating the highest melting temperature materials: A laser melting study of the TaC-HfC system, *Scientific Reports*. 6 (2016) 1–11. <https://doi.org/10.1038/srep37962>.
- [6] A.J. Wright, Q. Wang, S.T. Ko, K.M. Chung, R. Chen, J. Luo, Size disorder as a descriptor for predicting reduced thermal conductivity in medium- and high-entropy pyrochlore oxides, *Scripta Materialia*. 181 (2020) 76–81. <https://doi.org/10.1016/j.scriptamat.2020.02.011>.

- [7] R. Banerjee, S. Chatterjee, M. Ranjan, T. Bhattacharya, S. Mukherjee, S.S. Jana, A. Dwivedi, T. Maiti, High-entropy perovskites: An emergent class of oxide thermoelectrics with ultralow thermal conductivity, *ACS Sustainable Chemistry and Engineering*. 8 (2020) 17022–17032. <https://doi.org/10.1021/acssuschemeng.0c03849>.
- [8] E. Castle, T. Csanádi, S. Grasso, J. Dusza, M. Reece, Processing and Properties of High-Entropy Ultra-High Temperature Carbides, *Scientific Reports*. 8 (2018). <https://doi.org/10.1038/s41598-018-26827-1>.
- [9] T.J. Harrington, J. Gild, P. Sarker, C. Toher, C.M. Rost, O.F. Dippo, C. McElfresh, K. Kaufmann, E. Marin, L. Borowski, P.E. Hopkins, J. Luo, S. Curtarolo, D.W. Brenner, K.S. Vecchio, Phase stability and mechanical properties of novel high entropy transition metal carbides, *Acta Materialia*. 166 (2019). <https://doi.org/10.1016/j.actamat.2018.12.054>.
- [10] Y. Wang, T. Csanádi, H. Zhang, J. Dusza, M.J. Reece, R.Z. Zhang, Enhanced Hardness in High-Entropy Carbides through Atomic Randomness, *Advanced Theory and Simulations*. 2000111 (2020) 1–8. <https://doi.org/10.1002/adts.202000111>.
- [11] M. Qin, J. Gild, C. Hu, H. Wang, M.S. bin Hoque, J.L. Braun, T.J. Harrington, P.E. Hopkins, K.S. Vecchio, J. Luo, Dual-phase high-entropy ultra-high temperature ceramics, *Journal of the European Ceramic Society*. 40 (2020) 5037–5050. <https://doi.org/10.1016/j.jeurceramsoc.2020.05.040>.
- [12] S.H. Hong, S.C. Mun, G.C. Kang, H.J. Park, Y.B. Jeong, G. Song, K.B. Kim, Recent development of coloring alloys, *Progress in Materials Science*. (2021) 100811. <https://doi.org/10.1016/J.PMATSCI.2021.100811>.
- [13] H.A.A. El-Fattah, I.S. El-Mahallawi, M.H. Shazly, W.A. Khalifa, Optical properties and microstructure of TiN_xO_y and TiN thin films before and after annealing at different conditions, *Coatings*. 9 (2019) 1–15. <https://doi.org/10.3390/coatings9010022>.
- [14] S. Curtarolo, W. Setyawan, G.L.W.W. Hart, M. Jahnatek, R. v. Chepulskii, R.H. Taylor, S. Wang, J. Xue, K. Yang, O. Levy, M.J. Mehl, H.T. Stokes, D.O. Demchenko, D. Morgan, AFLOW: An automatic framework for high-throughput materials discovery, *Computational Materials Science*. 58 (2012) 218–226. <https://www.sciencedirect.com/science/article/pii/S0927025612000717?via%3Dihub> (accessed August 31, 2018).
- [15] K. Kaufmann, D. Maryanovsky, W.M. Mellor, C. Zhu, A.S. Rosengarten, T.J. Harrington, C. Oses, C. Toher, S. Curtarolo, K.S. Vecchio, Discovery of high-entropy ceramics via machine learning, *Npj Computational Materials*. 6 (2020) 1–9. <https://doi.org/10.1038/s41524-020-0317-6>.
- [16] K. Kaufmann, K.S. Vecchio, Searching for high entropy alloys: A machine learning approach, *Acta Materialia*. 198 (2020) 178–222. <https://doi.org/10.1016/j.actamat.2020.07.065>.

- [17] L. Ward, A. Agrawal, A. Choudhary, C. Wolverton, A general-purpose machine learning framework for predicting properties of inorganic materials, *Npj Computational Materials*. 2 (2016) 1–7. <https://doi.org/10.1038/npjcompumats.2016.28>.
- [18] C. Wang, W. Ping, Q. Bai, H. Cui, R. Hensleigh, R. Wang, A.H. Brozena, Z. Xu, J. Dai, Y. Pei, C. Zheng, G. Pastel, J. Gao, X. Wang, H. Wang, J.C. Zhao, B. Yang, X. Zheng, J. Luo, Y. Mo, B. Dunn, L. Hu, A general method to synthesize and sinter bulk ceramics in seconds, *Science*. 368 (2020) 521–526. <https://doi.org/10.1126/science.aaz7681>.
- [19] X.D. Xiang, X. Sun, G. Briceño, Y. Lou, K.A. Wang, H. Chang, W.G. Wallace-Freedman, S.W. Chen, P.G. Schultz, A combinatorial approach to materials discovery, *Science*. 268 (1995) 1738–1740. <https://doi.org/10.1126/science.268.5218.1738>.
- [20] D. Miracle, B. Majumdar, K. Wertz, S. Gorsse, New strategies and tests to accelerate discovery and development of multi-principal element structural alloys, *Scripta Materialia*. 127 (2017) 195–200. <https://doi.org/10.1016/j.scriptamat.2016.08.001>.